Davies, P. J., McKenzie, J. A., Palmer-Julson, A., et al., 1991
Proceedings of the Ocean Drilling Program, Initial Reports, Vol. 133

9. SITE 816[1]

Shipboard Scientific Party[2]

HOLE 816A

Date occupied: 31 August 1990

Date departed: 31 August 1990

Time on hole: 12 hr, 27 min

Position: 19°11.924'S, 150°0.608'E

Bottom felt (rig floor; m, drill-pipe measurement): 449.0

Distance between rig floor and sea level (m): 11.17

Water depth (drill-pipe measurement from sea level, m): 437.8

Total depth (rig floor; m): 560.5

Penetration (m): 111.5

Number of cores (including cores with no recovery): 15

Total length of cored section (m): 111.5

Total core recovered (m): 97.53

Core recovery (%): 87.5

Oldest sediment recovered:
Depth (mbsf): 111.5
Nature: rhodolith-bearing bioclastic floatstone
Age: middle Miocene

HOLE 816B

Date occupied: 31 August 1990

Date departed: 1 September 1990

Time on hole: 13 hr, 50 min

Position: 19°11.911'S, 150°0.601'E

Bottom felt (rig floor; m, drill-pipe measurement): 449.0

Distance between rig floor and sea level (m): 11.17

Water depth (drill-pipe measurement from sea level, m): 437.8

Total depth (rig floor; m): 620.0

Penetration (m): 171.0

Number of cores (including cores with no recovery): 9

Total length of cored section (m): 77.2

Total core recovered (m): 10.5

Core recovery (%): 13.6

Oldest sediment recovered:
Depth (mbsf): 163.2
Nature: rhodolith-bearing bioclastic floatstone
Age: middle Miocene

HOLE 816C

Date occupied: 1 September 1990

Date departed: 2 September 1990

Time on hole: 1 day, 9 hr, 30 min

Position: 19°11.911'S, 150°0.608'E

Bottom felt (rig floor; m, drill-pipe measurement): 449.0

Distance between rig floor and sea level (m): 11.17

Water depth (drill-pipe measurement from sea level, m): 437.8

Total depth (rig floor; m): 699.0

Penetration (m): 250.0

Number of cores (including cores with no recovery): 13

Total length of cored section (m): 109.6

Total core recovered (m): 11.3

Core recovery (%): 10.3

Oldest sediment recovered:
Depth (mbsf): 250.0
Nature: dolomitized coralgal boundstone with rhodoliths
Age: middle Miocene

Principal results: Site 816 is located on the northwestern corner of the Marion Plateau. Drilling penetrated a 250-m-thick sequence of sediments composed of a 91-m-thick unit of lower Pliocene–Pleistocene hemipelagic sediments overlying very shallow water (<5 m) lithified middle Miocene carbonates. The bio-assemblages of the shallow-water sediments are clearly chlorozoan, indicative of warm surface waters. Within the hemipelagic sediments, benthic foraminifer assemblages indicate upper bathyal depths (200–600 m) during the period of sedimentation. The sedimentation rate was low (0.5 cm/k.y.) during the late Pleistocene, whereas late Pliocene rates (2 cm/k.y.) were rather normal for a pelagic setting. Shipboard paleomagnetic studies show a reversed paleomagnetic signal for the sediments in the upper 31 m of Hole 816A, indicating that most of the Brunhes and perhaps part of the Matuyama magnetic zones are missing. This could account for the low sedimentation rate in the Pleistocene. As at Site 815, the sedimentation rate apparently increased dramatically during the early Pliocene, but, until there is better biostratigraphic control, it is impossible to estimate how high the rate actually was. Shore-based studies of material obtained from this sedimentary sequence, together with that from Site 815, will provide important environmental information on the factors controlling carbonate platform growth and demise.

Three major sedimentary units were recovered between the seafloor and 250 mbsf (meters below seafloor). The lithologic units are as follows:

1. *Unit I:* depth, 0–93.0 mbsf; age, Pleistocene to early Pliocene. At the top, Unit I comprises light gray foraminifer nannofossil ooze that grades into olive green nannofossil clayey ooze with dolomite and foraminifers at the base. It has been divided into four subunits based on the varying ratios of foraminifers, nannofossils, and clay.

(1) *Subunit IA:* depth, 0–15.0 mbsf; age, Pleistocene. Subunit IA contains locally bioturbated light-gray nannofossil foraminifer ooze with clay and bioclasts. Carbonate content is usually >80% but decreases to 77% at 9.5 mbsf.

(2) *Subunit IB:* depth, 15.0–24.5 mbsf; age, late Pliocene. Subunit IB contains olive-gray bioturbated mottled clayey foraminifer ooze with nannofossils. Carbonate content generally ranges between 71% and 75%.

(3) *Subunit IC:* depth, 24.5–62.5 mbsf; age, Pliocene. Subunit IC contains olive-gray bioturbated mottled clayey foraminifer

[1] Davies, P. J., McKenzie, J. A., Palmer-Julson, A., et al., 1991. *Proc. ODP, Init. Repts.*, 133: College Station, TX (Ocean Drilling Program).

[2] Shipboard Scientific Party is as given in list of participants preceding the contents.

nannofossil ooze. Bioturbated areas are locally pyrite rich. Carbonate content ranges from 54% to 82%.

(4) *Subunit ID:* depth: 62.5–93.0 mbsf; age, early Pliocene. Subunit ID contains olive gray to olive bioturbated nannofossil ooze to chalk with foraminifers and dolomite. Carbonate content varies from 58% to 84%.

2. *Unit II:* depth, 93.0–163.7 mbsf; age, middle Miocene. Unit II contains partially dolomitized rhodolith-bearing bioclastic floatstone and rudstone. Spheroidal to discoidal rhodoliths are cemented within a matrix consisting of coarse angular fragments of mollusks, coralline algae, coral, *Halimeda,* bryozoans, echinoid spines, and lithoclasts. Moldic and intraparticle porosity is well developed and geopetal fabrics partially fill some cavities. Deposition probably occurred in a shallow (<5 m water depth) back-reef environment.

3. *Unit III:* depth, 163.7–250.0 mbsf; age, middle Miocene. Unit III consists of dolomitized coralline algal and coral (including *Porites* and *Acropora*) boundstone and framestone with white rhodoliths up to 5 cm in diameter. The minor bioclasts include fragments of coralline algae, mollusks, rare *Halimeda,* and coral. Moldic and intraparticle porosity are well developed. Deposition probably occurred in very shallow water on a reef flat, possibly in an intertidal regime.

The interstitial water chemistry of the hemipelagic sequence cored at Site 816 shows a downward trend of increasing Ca^{2+} and decreasing Mg^{2+} concentrations to 80 mbsf. This inverse correlation can be attributed to dolomite formation below 93 mbsf within the shallow-water carbonate units. The Sr^{2+} concentration increases downward, reflecting the dissolution of metastable carbonates. When normalized to the chloride concentration, the sulfate content decreases downward, an indication for bacterial sulfate reduction. The presence of sulfur in the bulk sediment, with concentrations as high as 14%, is consistent with sulfate reduction in the hemipelagic sequence.

From the top to 93 mbsf, the predominant carbonate mineral is calcite, but aragonite is also present ($\leq$12.6%) within the upper Pliocene hemipelagic sediments between 22.4 and 79.4 mbsf. In Unit II and III, the dominant carbonate mineral is dolomite. The carbonate content of the hemipelagic sediments is variable, ranging from 50% to 90%, but with depth there is an overall trend toward decreasing values to 80 mbsf.

Extremely high variability in both resistivity and velocity logs was measured in the depth intervals corresponding to Units II and III, indicating correspondingly high variability in porosity, which is presumably controlled by diagenesis. The character of the record differs between the two units, suggesting different sedimentary/diagenetic histories. Unit II shows four cycles of very large bimodal alternations between near-zero porosity and high porosity. The bimodality is probably related to the initial lithostratigraphy rather than diagenetic recrystallization, but the near-zero values would require substantial recrystallization. Unit III shows a different velocity/resistivity relationship than that recorded for Unit II. With substantial porosity increases, the observed pattern in the logs suggests that the rocks in Unit III have experienced considerable cementation followed by a later stage of dissolution, which produced porosity with a high degree of pore connectivity but had little effect on the rigidity of the formation.

The total organic carbon content of the sediments was low but variable, ranging between 0% and 0.55% with slightly higher values for the hemipelagic sediments. Volatile hydrocarbons, with methane concentrations about 2 ppm and no ethane or propane, presented no safety problems.

BACKGROUND AND SCIENTIFIC OBJECTIVES

Site 816 occurs in approximately 440 m of water on the northern edge of the Marion Plateau, and is a true platform site in comparison with Site 815, which is a slope site. The scientific objectives at Site 816 could be met with a relatively shallow hole (250 mbsf). The site survey data (see Fig. 5, "Site 815" chapter, this volume) and the seismic section (Fig. 4, "Site 815" chapter, this volume) shows the site situated on the southern flank of a buildup considered to be the last phase of substantial reef growth on the Marion Plateau, represented by horizon 14 (Fig. 1). The section below the mound structure (i.e., below horizon 15), is also considered to represent reef growth, but of much earlier age, probably representing early to middle Miocene platform establishment. The section above the buildup is thought to represent the vestiges of the current deposition so prevalent at Site 815 (up to horizon 1), and which was finally terminated by the pelagic sequence representing the subsidence of the Marion Plateau as seen between horizon 1 and the seafloor. The objectives of drilling at Site 816 were:

1. To determine the minimum position of the middle Miocene eustatic highstand.
2. To determine the nature and age of two phases of carbonate platform growth, thereby defining the paleoclimatic and oceanographic regimes twice during the Neogene.
3. To determine the cause and timing of the demise of both phases of carbonate platform accretion as a key to understanding the controls on carbonate platform development.
4. To determine the nature and age of the sequence that overlies these carbonate platforms so as to understand the climatic and oceanographic regimes at a time when carbonate platform facies were not being deposited.

OPERATIONS

Transit to Site 816

The transit in dynamic positioning (DP) mode from Site 815 to Site 816 (proposed site NEA-13) covered 3 nmi in 1.75 hr at an average speed of 1.8 kt. A Datasonics beacon was dropped at 0310L (all times given in local time, or L), 31 August 1990, within an optimal global positioning system (GPS) window at the previously surveyed GPS coordinates.

Hole 816A

Hole 816A was spudded at 19°11.924′S, 150°0.608′E at 0428L, 31 August. The precision depth recorder (PDR) indicated a water depth of 437.7 m from sea level. The bit was positioned at a water depth of 433.8 m from sea level and the first core was shot. Core 133-816A-1H recovered 5.53 m of sediment, placing the mud line at 437.8 m. Continuous APC cores (Cores 133-816A-1H through -11H) were taken from 0.0 to 93.0 mbsf, with 93.0 m cored and 96.0 m recovered (103.2% recovery). APC coring ended in hard shallow-water limestone when Core 133-816A-11H reached refusal. Cores 133-816A-12X through -15X were taken from 93.0 to 111.5 mbsf, with 18.5 m cored and 1.60 m recovered (8.6%). XCB coring ended due to a slow penetration rate (31 min/ft) and low recovery. The BHA was pulled out of the hole to the seafloor at 1527L, and was back on deck at 1710L, 31 August.

Hole 816B

The ship moved 15 m north in DP mode, arriving on location for Hole 816B, 19°11.911′S, 150°0.601′E, at 1555L 31 August. A Hycalog four-cone insert bit was run with a mechanical bit release (MBR), outer core barrel, 11 drill collars, and Hydrolex jars. This RCB bottom-hole assembly was run to the seafloor and Hole 816B was spudded at 2030L. The 9-7/8-in. hole was washed down to 86 mbsf, the depth at which good recovery had ended in Hole 816A. Continuous RCB cores (Cores 133-816B-1R through -8R) were taken from 86.0 to 163.2 mbsf, with 77.2 m cored and 10.49 m recovered (13.6% recovery). At that point the pipe stuck, so a 20-bbl-mud sweep was circulated and the drillstring was worked up to 270,000 lb overpull. One blow with the jars at 60,000 lb freed the pipe, and Core 133-816A-9R was drilled from 163.2

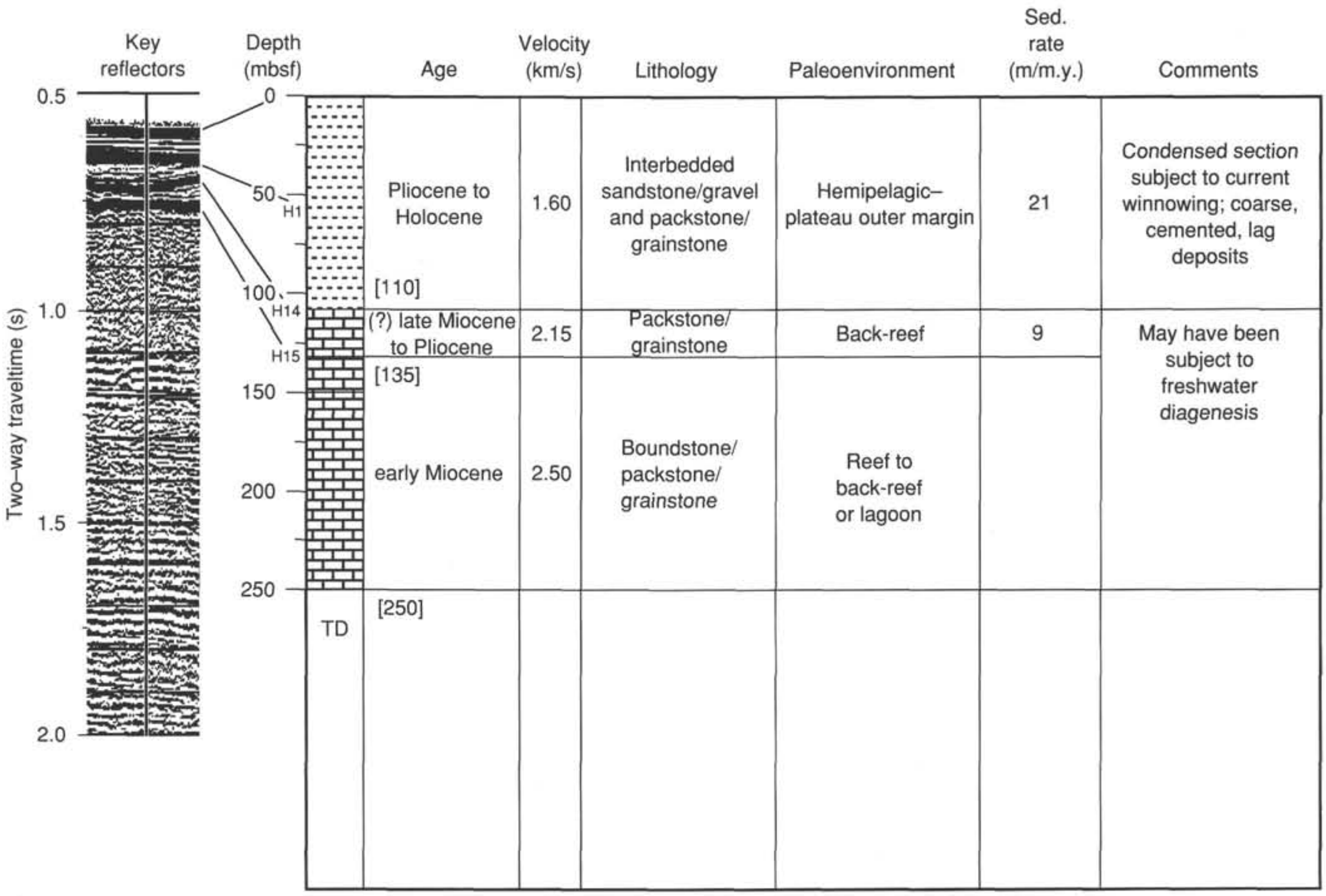

Figure 1. Pre-drilling prognosis for Site 816 (line is BMR 75/027 Pt. A).

to 171.0 mbsf. However, during our attempt to retrieve this core, we discovered that the core barrel had been lost in the hole. The drill string was pulled and back on deck at 0700L, 1 September. The bit and the MBR disconnect were left in the hole, apparently as a result of a split in the MBR disconnect.

Hole 816C

The ship was moved 15 m north in DP mode to 19°11.911′S, 150°0.608′E for Hole 816C. A used 9-7/8-in. RBI bit and MBR were run, and Hole 816C was spudded at 0853L 1 September. The hole was washed from 0.0 to 140.4 mbsf, recovering Core 133-816C-1W with the wash barrel. Cores 133-816C-2R through -13R were recovered from 140.4 to 250.0 mbsf, with 109.6 m cored and 11.2 m recovered (10.2% recovery). A 15-bbl mud sweep was pumped during the middle part of the coring process to avoid overpull and pipe sticking as cuttings accumulated. The hard, brittle limestone and dolomite tended to jam in the core catcher and liner after about 1 m of recovery. A short trip was made to 93 mbsf to condition the hole for logs, the bit and MBR were released, and the pipe pulled up to 102 mbsf.

Logs were run as follows:

1. The induction/density/sonic/caliper/gamma-ray (DITE/HLDT/SDT/MCDG/NGT) logging tool entered the hole at 0205L, 2 September, and was back out at 0310L; the tool was run to within 2.6 m of the bottom of the hole.
2. The formation microscanner (FMS)/gamma-ray/temperature (FMS/NGT/TCC) tool string entered the hole at 0445L, 2 September, and was back out at 0640L; this tool likewise encountered 2.6 m of fill.
3. The wireline packer was run in at 0820L, and an unsuccessful attempt was made to set the packer at 229.8 mbsf; the tool was pulled out at 1255L. The lower packer assembly stuck in the adjustable latch sleeve in the head sub. The weak point was sheared at 8000 lb to retrieve the upper electronics package. We found that A suction screen had plugged with silt and had collapsed. Insufficient water was collected to provide a sample.
4. The water sampler temperature pressure (WSTP) tool was run on the coring wireline to obtain a water sample (which we later found was seawater) from 87 mbsf (above the point at which the packer had stuck in the drill pipe).

The drill string was pulled, and the MBR cleared the seafloor at 1453L, and was back on deck at 1630L, 2 September. The beacon was recalled and retrieved within 15 min.

Table 1 contains the coring summary for Site 816.

SITE GEOPHYSICS

A general description of the design and operation of the joint site location survey for Sites 815 and 816 is included in the "Site Geophysics" section, "Site 815" chapter, this volume.

Following completion of drilling at Site 815 and separation from the beacon at JD 242/1525 UTC, 30 August 1990, the *JOIDES Resolution* returned to her confirmed GPS position for Site 816 in dynamic positioning mode. A beacon was dropped at the site at JD 242/1710 UTC; final coordinates of Hole

Table 1. Coring summary, Site 816.

Core no.	Date (1990)	Time (UTC)	Depth (mbsf)	Length Cored (m)	Length Recovered (m)	Recovery (%)	Age (Ma)
133-816A							
1H	August 30	1830	0–5.5	5.5	5.53	100.0	.93–1.27
2H		1845	5.5–15.0	9.5	9.71	102.0	1.88–2.29
3H		1900	15.0–24.5	9.5	9.35	98.4	2.6–3.45
4H		1935	24.5–34.0	9.5	9.84	103.0	3.51–4.24
5H		2000	34.0–43.5	9.5	9.88	104.0	4.24–5.26
6H		2025	43.5–53.0	9.5	9.90	104.0	4.24–5.26
7H		2040	53.0–62.5	9.5	9.88	104.0	
8H		2100	62.5–72.0	9.5	10.07	106.0	4.24–5.26
9H		2121	72.0–81.5	9.5	9.96	105.0	4.24–5.26
10H		2145	81.5–91.0	9.5	10.01	105.3	4.24–5.26
11H		2205	91.0–93.0	2.0	1.89	94.5	middle Miocene
12X		2335	93.0–98.2	5.2	0.21	4.0	middle Miocene
13X	August 31	0040	98.2–102.2	4.0	0.17	4.3	middle Miocene
14X		0140	102.2–107.8	5.6	0.42	7.5	middle Miocene
15X		0425	107.8–111.5	3.7	0.71	19.2	middle Miocene
Coring totals				111.5	97.53	87.5	
133-816B							
1R	August 31	1225	86.0–95.6	9.6	4.15	43.2	
2R		1310	95.6–105.3	9.7	0.90	9.3	
3R		1415	105.3–114.9	9.6	0.76	7.9	
4R		1500	114.9–124.6	9.7	0.63	6.5	
5R		1540	124.6–134.3	9.7	0.10	1.0	
6R		1620	134.3–144.0	9.7	0.06	0.6	
7R		1705	144.0–153.6	9.6	1.36	14.1	
8R		1745	153.6–163.2	9.6	2.53	26.3	
Coring totals				77.2	10.49	13.6	
133-816C							
1W	September 01	0130	0.0–140.4	140.4	5.32	(wash core)	
2R		0215	140.4–144.4	4.0	0.08	2.0	
3R		0320	144.4–154.0	9.6	0.61	6.4	
4R		0440	154.0–163.7	9.7	0.84	8.7	
5R		0530	163.7–173.4	9.7	0.93	9.6	
6R		0605	173.4–183.1	9.7	1.11	11.4	
7R		0640	183.1–192.4	9.3	0.51	5.5	
8R		0715	192.4–202.0	9.6	1.65	17.2	
9R		0755	202.0–211.3	9.3	0.47	5.1	
10R		0840	211.3–221.0	9.7	0.38	3.9	
11R		0930	221.0–230.7	9.7	3.22	33.2	
12R		1010	230.7–240.3	9.6	0.74	7.7	
13R		1055	240.3–250.0	9.7	0.72	7.4	
Coring totals				109.6	11.26	10.3	
Washing totals				140.4	5.32		
Combined totals				250.0	16.58		

Note that times are given in Universal Time Coordinated or UTC, which is 10 hr later than local time, or L.

816A are 19°11.924′S and 150°0.608′E, with a water depth of 437.8 m (drill-pipe measurement, or DPM, from sea level).

Site 816 lies in ~440 m of water on the northern margin of the Marion Plateau adjacent to the western Townsville Trough (see Figs. 7 and 8, "Site 815" chapter, this volume), ~56 km northeast of the Great Barrier Reef and ~220 km west of Marion Reef (Fig. 2). It is the most southerly of the two sites (Sites 815 and 816) on the northern Marion Plateau, and was positioned to drill through the edge of one of the youngest phases of carbonate platform growth and into the top of the oldest recognized platform complex (see Fig. 9, "Site 815" chapter, this volume).

There was good correlation at the site between the intersecting *JOIDES Resolution* single channel seismic profiles and the *Rig Seismic* multichannel seismic profiles (Figs. 3 and 4). Basement is not visible on any of the water-gun data across the site; however, normal resolution air-gun seismic data in the area (Symonds and Davies, 1988) indicates that it lies about 1.6 s TWT (two-way traveltime) below seafloor. The top of the strong band of reflectors about 0.5 s TWT below seafloor at Site 816 may mark the base of the platform facies. The site is underlain by an upper 0.11 s TWT thick (~90 m) flat lying and onlapping ?ooze sequence, which overlies a mounded sequence containing low amplitude reflectors. This sequence is about 0.05 s TWT thick (~60 m) at the site, and sits on a series of irregular, discontinuous reflectors, which extend to TD and appear to form the top of the older phase of platform growth. Beneath TD the platform is about 0.3 s TWT thick (possibly >450 m thick), and consists of mounded non-reflecting "build-up" facies, interspersed with onlapping and offlapping, irregular, low amplitude reflectors, which may represent slope and "lagoonal" facies.

To provide some predictive capability during the drilling at Site 816, an estimate of the two-way traveltime (TWT)/depth relationship below the seafloor was made using stacking derived interval velocities from the BMR seismic line across the site (Fig. 5). Greater than 200 mbsf, Sites 816 and 812 have similar TWT/depth relationships and considerably higher velocities than for equivalent depth sediment at Site 811, reflecting their position within a carbonate platform. Shallower than 200 mbsf, Site 812 has a similar TWT/depth profile to Site 811

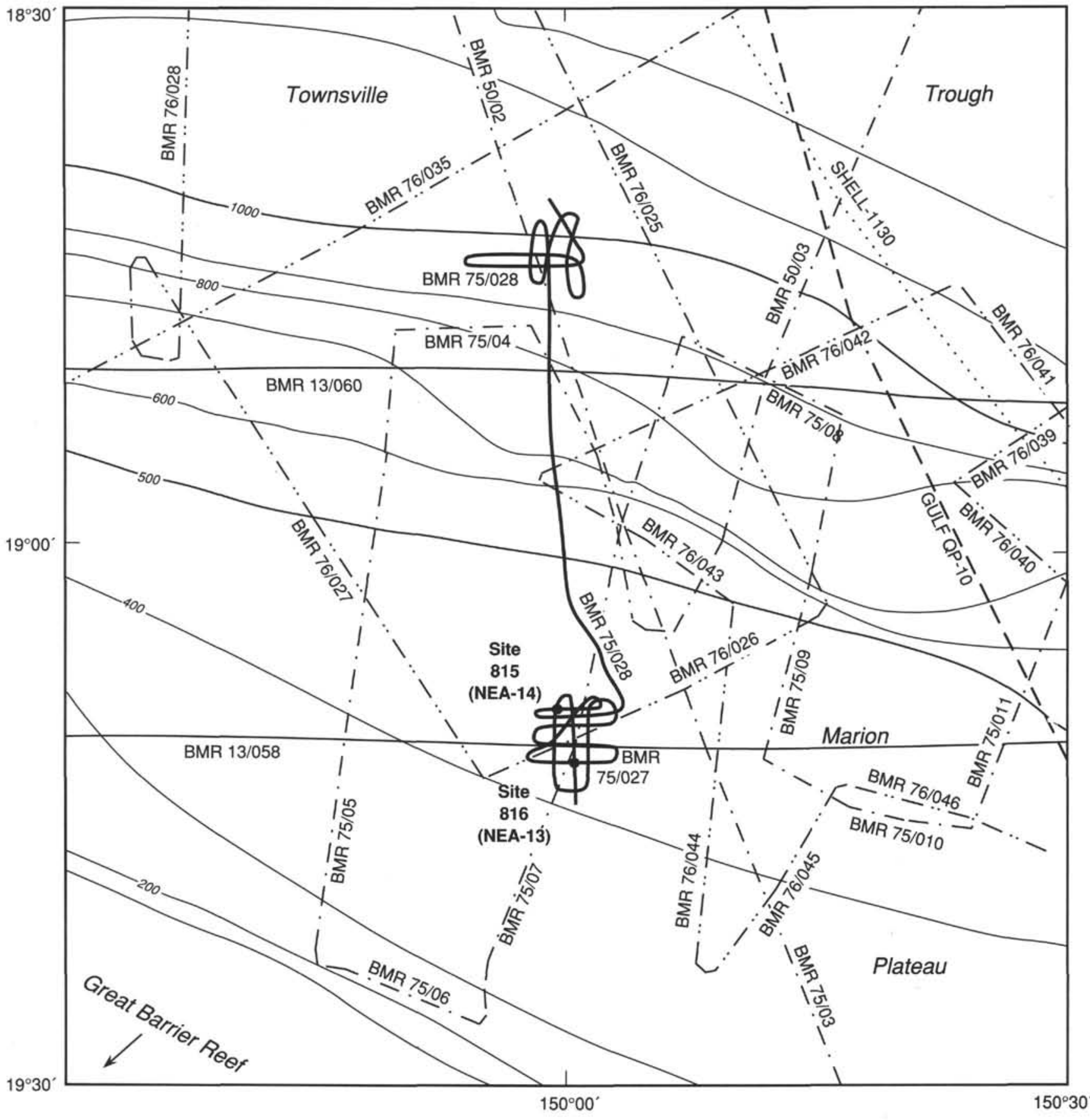

Figure 2. Track chart showing the distribution of regional seismic data in the area around Sites 815 and 816 and simplified bathymetry in meters.

and thus lower sediment velocities than Site 816. This difference corresponds to the occurrence of low velocity "lagoonal" sediments within the upper part of the section at Site 812, whereas at Site 816 solid platform facies with relatively high velocities are present at shallow depths.

LITHOSTRATIGRAPHY

Introduction

The lithostratigraphy of Site 816 is characterized by three units (Fig. 6), one of which was deposited entirely in a bathyal environment while the other two are of very shallow-water facies deposited in <20 m of water. Unit I is an ooze with varying foraminifer, nannofossil, and clay content; Unit II is a partially dolomitized rhodolith-bearing floatstone and rudstone; whereas Unit III is a dolomitized coralgal framestone with rhodoliths.

Lithologic Units

Unit I (Cores 133-816A-1H through -11H; depth, 0–93.0 mbsf; Core 133-816B-1R, depth, 86.0–89.76 mbsf; age, early Pliocene to Pleistocene)

Unit I is an upper bathyal ooze that varies from an olive green, nannofossil clayey ooze with dolomite and foraminifers

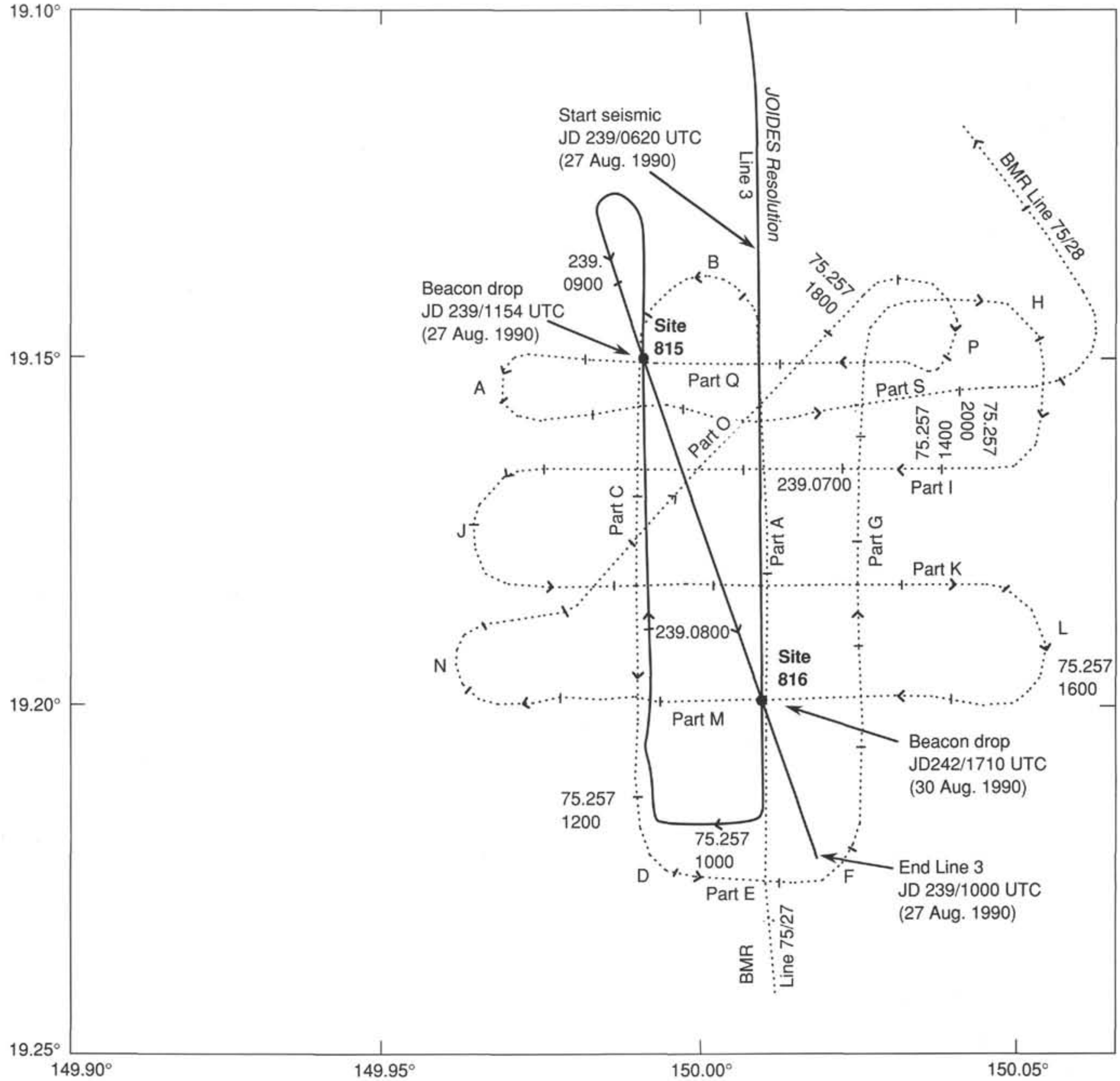

Figure 3. *JOIDES Resolution* Leg 133 site-location tracks (solid line) and *Rig Seismic* 1987 site-survey tracks (dotted line) around Sites 815 and 816.

at the base to a light gray foraminifer nannofossil ooze at the top. The entire unit is slightly bioturbated and mottled. The depth to the contact between Units I and II varies at each hole. This is probably due to synoptic relief on the upper surface of Unit II (see below).

The unit has been divided into four subunits based on the varying ratios of foraminifers, nannofossils, and clay. Carbonate content varies from 89% at the top of the section (Core 133-816A-1H) to ~53% at 33.01 mbsf (Core 133-816A-4H). The unit becomes both chalky and dolomitic toward the base. The ooze becomes firm by 53 mbsf (Core 133-816A-7H) and chalk nodules are present by 81.5 mbsf (Core 133-816A-10H). Dolomite first appears at ~20 mbsf (Core 133-816A-3H), peaks at ~65 mbsf (Core 133-816A-8H), and is then absent from the basal part of the unit (see "Inorganic Geochemistry" section, this chapter).

Although Unit I was deposited in an upper bathyal (200–600 m) environment (see "Biostratigraphy" section, this chapter), the benthic foraminifer assemblages indicate that the lowest part of the section, from 72 to 93 mbsf (Cores 133-816A-9H to -11H), was deposited in water depths no greater than 500 m. The contact between Unit I and II is shown in Figure 7.

Subunit IA (Cores 133-816A-1H to -2H; depth, 0–15.0 mbsf; age, Pleistocene)

Subunit IA consists of light gray, locally bioturbated, nannofossil, foraminifer ooze with clay and bioclasts. Carbonate content is usually more than 80% but drops to 77% at 9.5 mbsf.

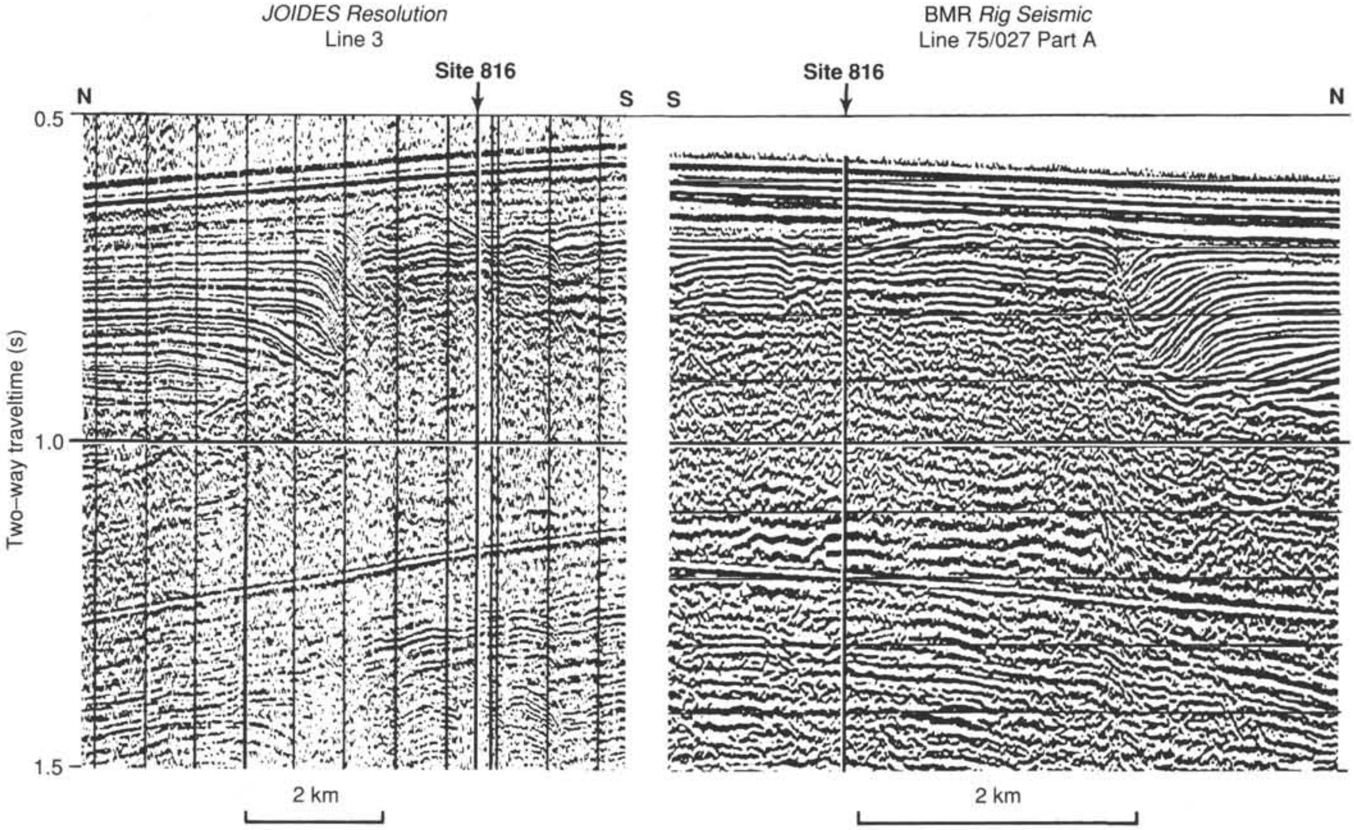

Figure 4. Comparison of *JOIDES Resolution* and *Rig Seismic* 80-in.[3] water-gun seismic profiles across Site 816.

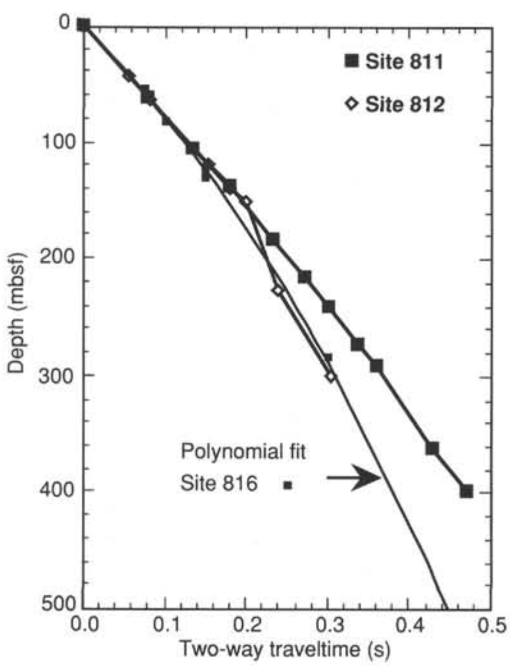

Figure 5. Comparison of TWT/depth curve estimated for Site 816 with those for Sites 811 and 812 on the Queensland Plateau.

Subunit IB (Core 133-816A-3H; depth, 15.0–24.5 mbsf; age, late Pliocene)

Subunit IB consists of olive gray, bioturbated, mottled clayey foraminifer ooze with nannofossils. Carbonate content usually falls within the range of 71%–75% except for two samples, one with 61.9% and the other 81.3%.

Subunit IC (Cores 133-816A-4H through -7H; depth, 24.5–62.5 mbsf; age, Pliocene)

Subunit IC consists of olive gray, bioturbated, mottled, clayey, foraminifer, nannofossil ooze. Bioturbated areas are locally pyrite rich. Carbonate content ranges from 53.1% to 85%.

Subunit ID (Cores 133-816A-8H through -11H; depth, 62.5–93.0 mbsf; Core 133-816B-1R, depth 86.0–89.76 mbsf; age, early Pliocene)

Subunit ID consists of olive gray to olive, bioturbated, nannofossil ooze and chalk with foraminifers and dolomite. Carbonate content varies from 54.6% to 83%.

Unit II (Cores 133-816A-12X through -15X, depth 93–111.5 mbsf; 133-816B-1R through -8R, depth, 89.76–163.2 mbsf; and 133-816C-2R through -4R, depth, 140.4–163.7 mbsf; age, middle Miocene)

Unit II consists of partially dolomitized rhodolith-bearing bioclastic floatstone and rudstone (Figs. 8 and 9). The rock consists of rhodoliths in a matrix of coarse angular fragments comprising mollusks, coralline algae, coral, *Halimeda,* and bryozoan debris, echinoid spines, and lithoclasts (Fig. 10). The rhodoliths are spheroidal to discoidal in shape, from 1 to 6 cm in diameter, with dominantly laminar thalli. They usually

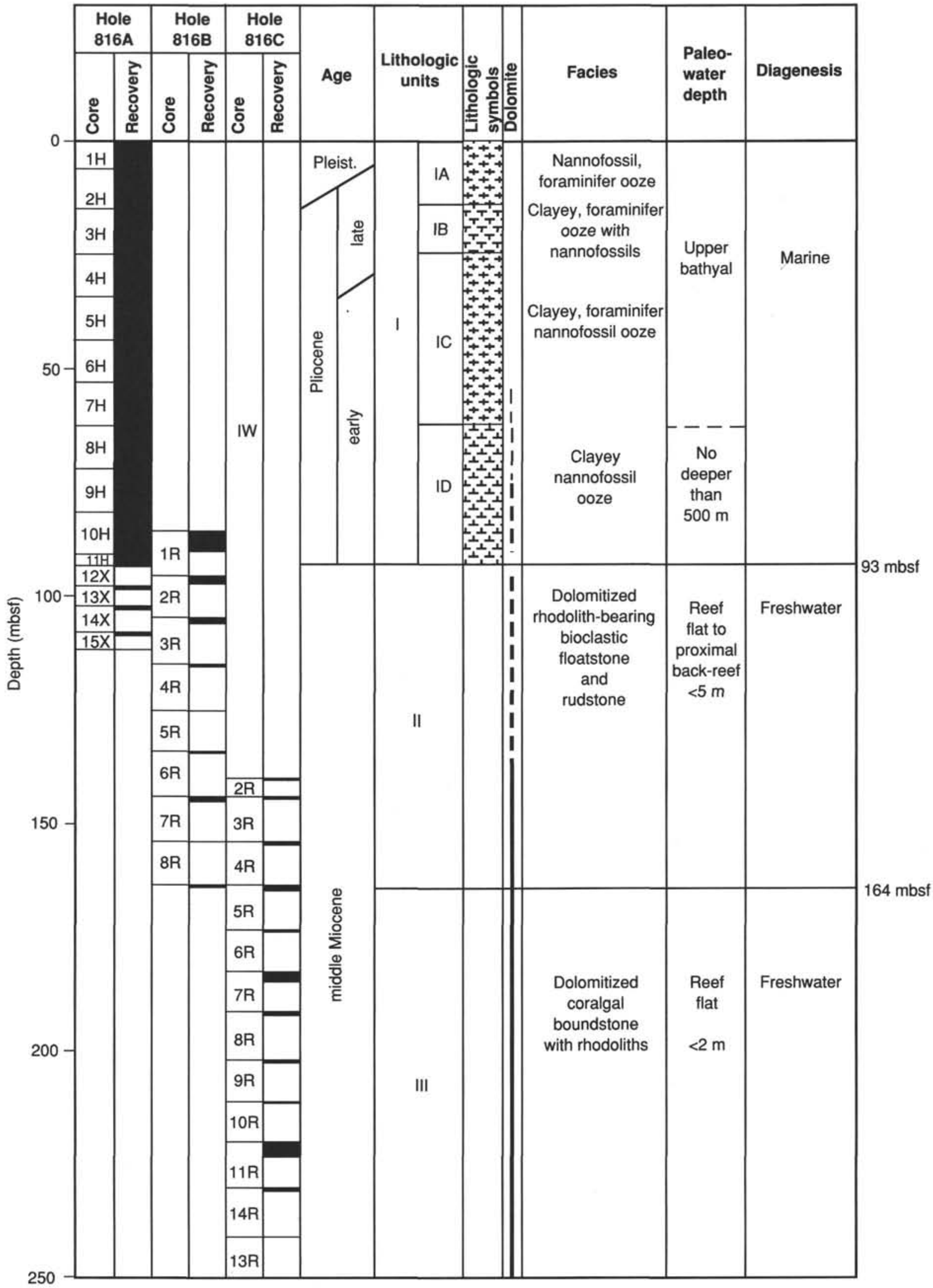

Figure 6. Lithostratigraphic column for Site 816. See "Explanatory Notes" chapter (this volume) for key to lithologic symboles.

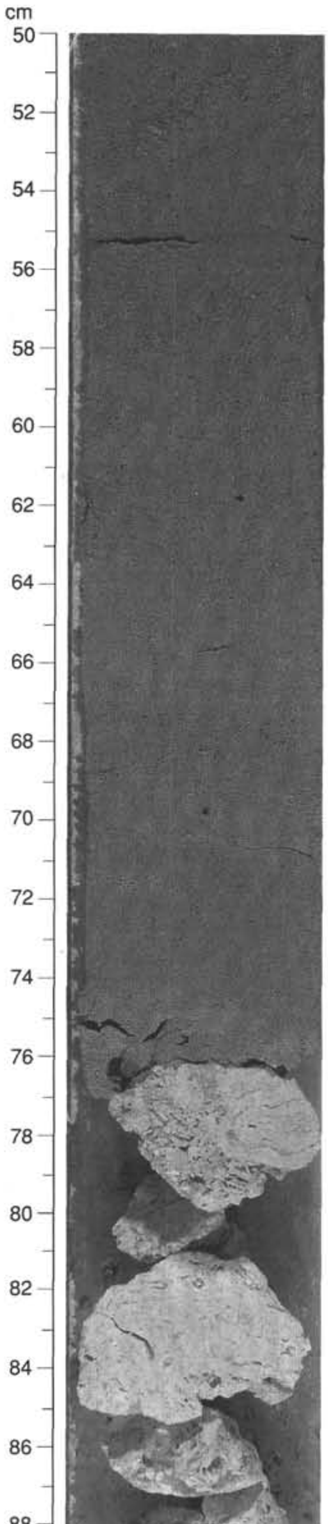

Figure 7. Photograph of interval from 50 to 90 cm in Section 133-816B-1R-3 (89.76 mbsf) showing the contact between the upper bathyal hemipelagic sediments of Unit I and shallow-water rhodolith bearing floatstone and rudstone of Unit II.

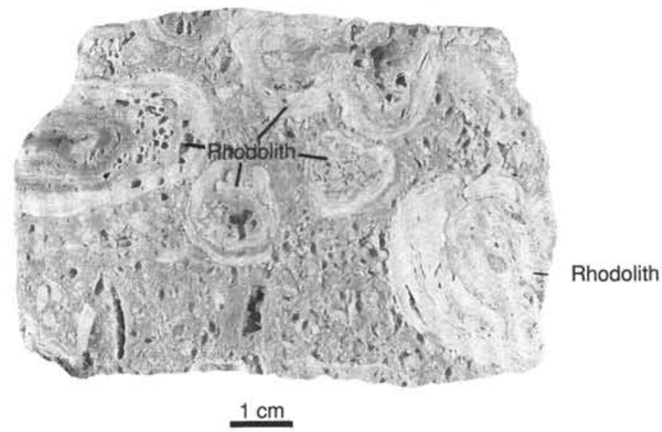

Figure 8. Photograph of a typical dolomitized, rhodolith-bearing rudstone from Unit II (50–59 cm in Section 133-816B-4R-1, 114.5 mbsf). Note the coral nuclei of the rhodoliths (including hydrozoan ?*Millepora,* in the rhodolith in the lower right corner) and the porosity development.

have coral or coralline algae cores (Figs. 8 and 9) and frequently show *Cliona* borings. Moldic and intraparticle porosity is well developed. Geopetal mud partially fills some cavities (Fig. 11).

The assemblage is chlorozoan and indicative of warm tropical surface waters. The angular, fragmented nature of the matrix components suggests that they are predominantly para-autochthonous and the composition of the assemblage suggests that the sediment was deposited in a shallow back-reef environment. The occurrence of more delicate, gracile coral forms below 144 m suggests a more protected proximal back-reef environment, implying some southward progradation of the back-reef facies. The entire unit was probably deposited in <5 m of warm (tropical) water.

The top of Unit II is at a different level in each of the three holes drilled at Site 816. In Hole 816A the top of Unit II was intersected at 91 mbsf (top of Core 133-816A-11H), whereas in Hole 816B it was intersected at 89.76 mbsf in Core 133-816B-1R). The contact between Units I and II was not sampled in Hole 816C but the logging results suggest that this contact is at 92 mbsf. This variation in the depth of the contact between Units I and II may be real in that the top of Unit II may have some relief due to the development of karstic topography while it was exposed during the late Miocene.

Unit III (Cores 133-816C-5R through -13R, depth, 163.7–250.0 mbsf; age, middle Miocene)

Unit III consists of dolomitized coralline algae and coral framestone with rhodoliths (Figs. 12–14). White rhodoliths and minor bioclasts are bound by light gray corals (Fig. 12) including *Porites* and *Acropora*. Bioclasts, which form a minor component of the sediment, include fragments of coralline algae, mollusks, rare *Halimeda,* and coral. The rhodoliths are up to 5 cm in diameter, generally spheroidal in shape, with both laminar and columnar thalli. The rhodoliths are often bored and have either coral or coralline algae nuclei (Fig. 14). Moldic and intraparticle porosity are well developed. Geopetal fabrics are present in some cavities (Fig. 15). The coral and *Halimeda* in this unit are typical of a chlorozoan assemblage indicative of warm tropical surface waters. This sediment was probably deposited in shallow water (0–20 m), possibly on a reef flat.

1 cm

Figure 9. Photograph of a dolomitized rhodolith-bearing rudstone from 7–11 cm in Section 133-816B-1R-CC (95.5 mbsf) showing coral nuclei of the rhodoliths and moldic and intraparticle porosity. Coral fragments are also present in the bioclastic matrix.

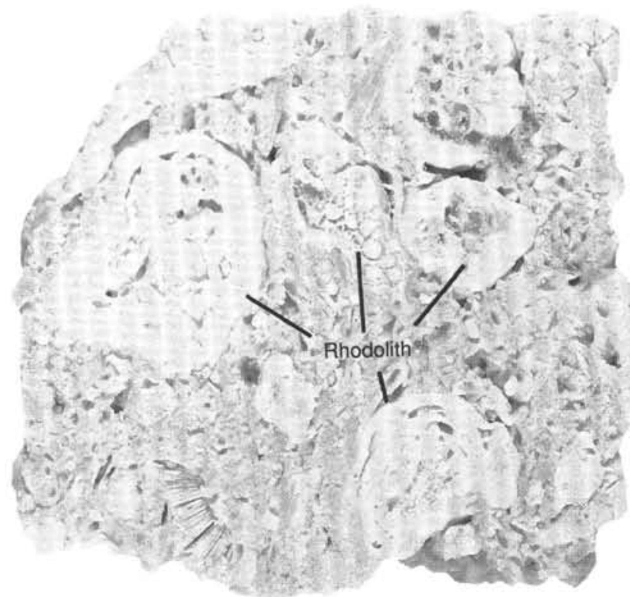

1 cm

Figure 10. Photograph of a dolomitized rhodolith-bearing rudstone from 70–75 cm in Section 133-816B-8R-2 (155.8 mbsf) showing the bioclastic nature of the matrix. Matrix fragments include coral, articulated coralline algae, mollusk, and echinoid detritus.

Discussion and Interpretation

One of the objectives in drilling Site 816 was to determine the nature and age of the phases of platform growth along the northern edge of the Marion Plateau. Our interpretation of the stratigraphic relations are shown in Figure 16, based on the preliminary dating of Unit II at Site 816 which shows that it is no younger than middle Miocene in age. The unconformity between Units V and VI at Site 815 must be carried up over the mound at Site 816, implying that the unconformity between Units II and I at Site 816 extends from the middle Miocene to the early Pliocene. This interpretation requires that all late Miocene sedimentation was confined to the slope and that the top of the carbonate platform at Site 816 was exposed throughout the late Miocene.

Another of the major objectives of drilling Site 816 was to establish the reason for the demise of the carbonate platform that covers the Marion Plateau and to establish the reasons for the drowning of the plateau. Site 816 recovered a sequence that was deposited in two markedly different environments and thereby records the drowning of the Marion Plateau. This stratigraphic record also provides an indication as to why the reef growth failed to re-establish itself in this part of the plateau in contrast to the eastern part of the plateau, where reef complexes were successful in recolonizing the plateau after major falls in sea level. Furthermore, the eastern reef complexes have kept up with the pronounced late Cenozoic relative sea-level rise so that a rapid relative rise in sea level does not in itself provide an explanation for the drowning of the plateau.

Units II and III were deposited in very shallow water as benthic assemblages clearly indicate. The presence of over 160 m of very shallow-water sediments demonstrates that the platform was able to keep pace with relative rises in sea level.

Unit I records the effects of rapid drowning of the platform and shows that at about 3.5 Ma (CN10–CN11) a pulse of subsidence produced a rapid relative rise in sea level, drowning most of the Marion Plateau. However, this rapid relative rise in sea level does not, in itself, explain why the carbonate platform in the northwestern part of the plateau failed to recover. The failure of the platforms to keep up in this part of the plateau is complex, but the information recovered from Site 816 may provide an explanation.

The initial demise of the platform was probably caused by exposure. The limited diagenetic information available suggests that the platform (Units II and III) has been subjected to freshwater diagenesis (based on post-cruise thin section analysis). When the platform was reflooded in the earliest Pliocene due largely to a pulse of subsidence, the platform failed to re-establish itself because water quality had deteriorated. The clay content of the sediments in Unit I (up to 46.4% at 80 m in Core 133-816A-9H) indicates that turbid water conditions were the principal reason for the reefs being unable to recolonize the older platform in the western part of the Marion Plateau. To the east, it is proposed that the late Miocene and Pliocene platforms were far enough removed from the influx of terrigenous clay to be unaffected and therefore able to re-establish themselves and keep up despite the subsidence

Figure 11. Photograph of well-cemented rhodolith-bearing floatstone from Unit II (74–84 cm) in Section 133-816A-15X-1 (108.5 mbsf). The rhodoliths vary considerably in size and are scattered through a bioclastic matrix. Geopetal fabrics within the large rhodolith at the center of the core indicate that up is to the right.

pulse. With increasing water depth the top of the plateau was quickly removed from the photic zone and the opportunity for recolonization lost.

In summary, results from the drilling at Site 816 suggest that the cause of the drowning of the Marion Plateau was complex and not simply due to a rapid relative rise in sea level. Initially shallow-water carbonate production was terminated because of exposure. Following reflooding of the plateau in the early Pliocene, turbid water conditions created an environment inimicable to shallow-water carbonate production, thus preventing the re-establishment of a shallow-water platform. Finally, a coincident rapid relative rise in sea level caused by increased subsidence removed the top of the plateau from the photic zone and drowned it.

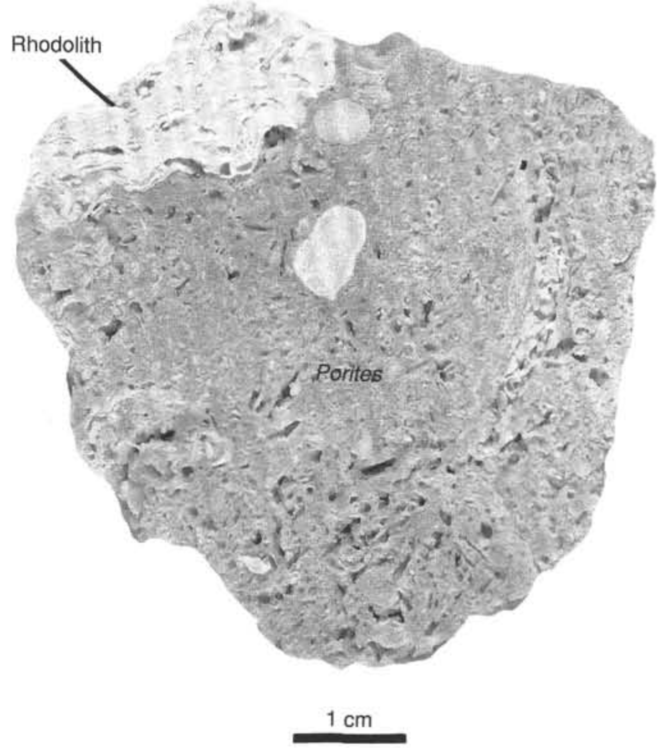

Figure 12. Photograph of dolomitized framestone with rhodoliths from Unit III (34–40 cm) in Section 133-816C-6R-1 (173.7 mbsf). The gray area of the core is mostly *Porites* that binds the rhodolith and articulate coralline algae fragments to form a framestone.

BIOSTRATIGRAPHY

Nannofossils, planktonic foraminifers, and benthic foraminifers were examined from the core-catcher samples at Hole 816A. Additional samples from within selected cores were also studied. The biostratigraphic results and zonal assignments indicate a Pliocene to Pleistocene section above Core 133-816A-12X. These results are summarized in Figure 17.

Hole 816A yielded abundant, moderately preserved calcareous nannofossils above Core 133-816A-12X. Planktonic foraminifers show moderate to good preservation, whereas benthic foraminifer preservation is excellent throughout this interval. Benthic foraminifer assemblages indicate an upper bathyal paleodepth for Hole 816A above Section 133-816A-11H-CC.

Calcareous Nannofossils

Site 816 yielded abundant, moderately preserved upper Pleistocene through lower Pliocene calcareous nannofossils from the seafloor to 93 mbsf. Underlying this interval is a consolidated neritic deposit. Sample 133-816A-12X-CC from the consolidated interval contains no nannofossils. Other core-catcher samples from this interval were either not available for examination or did not recover nannofossils in the recrystallized rocks. However, all the core-catcher samples from Cores 133-816A-1H through -11X, plus two samples directly above the consolidated sediment were examined for nannofossils.

Sample 133-816A-1H-CC yielded *Pseudoemiliania lacunosa* but no medium or large-sized *Gephyrocapsa,* and can be assigned to Subzone 13b (0.93–1.27 Ma). Sample 133-816A-2H-CC contains *Discoaster brouweri* but no *D. pentara-*

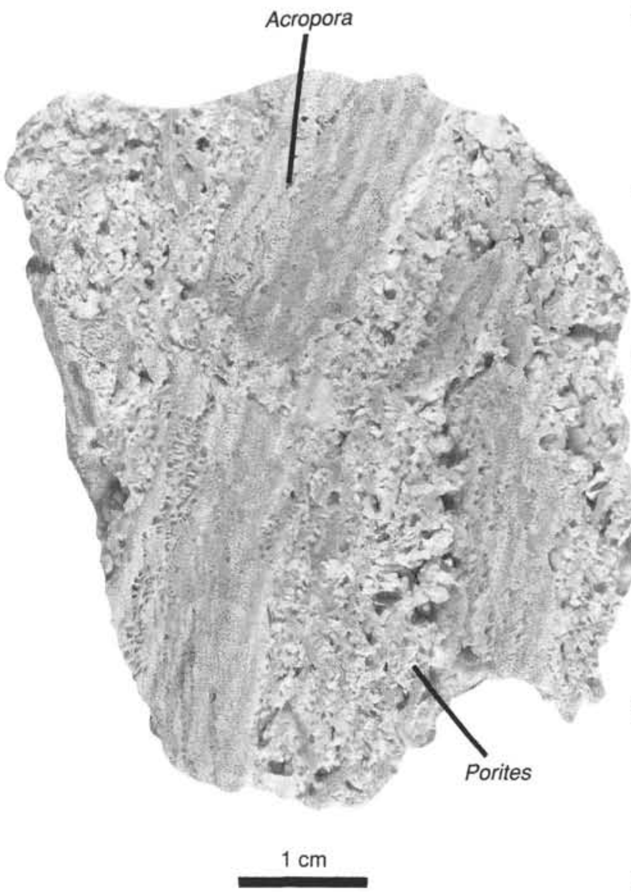

Figure 13. Photograph of dolomitized framestone from Unit III (6–10 cm in Section 133-816C-9R-1, 202.1 mbsf). The framestone consists almost entirely of coral including *Acropora, Porites,* and hydrozoan *?Millepora* (central left of core). This assemblage is indicative of water <20 m deep.

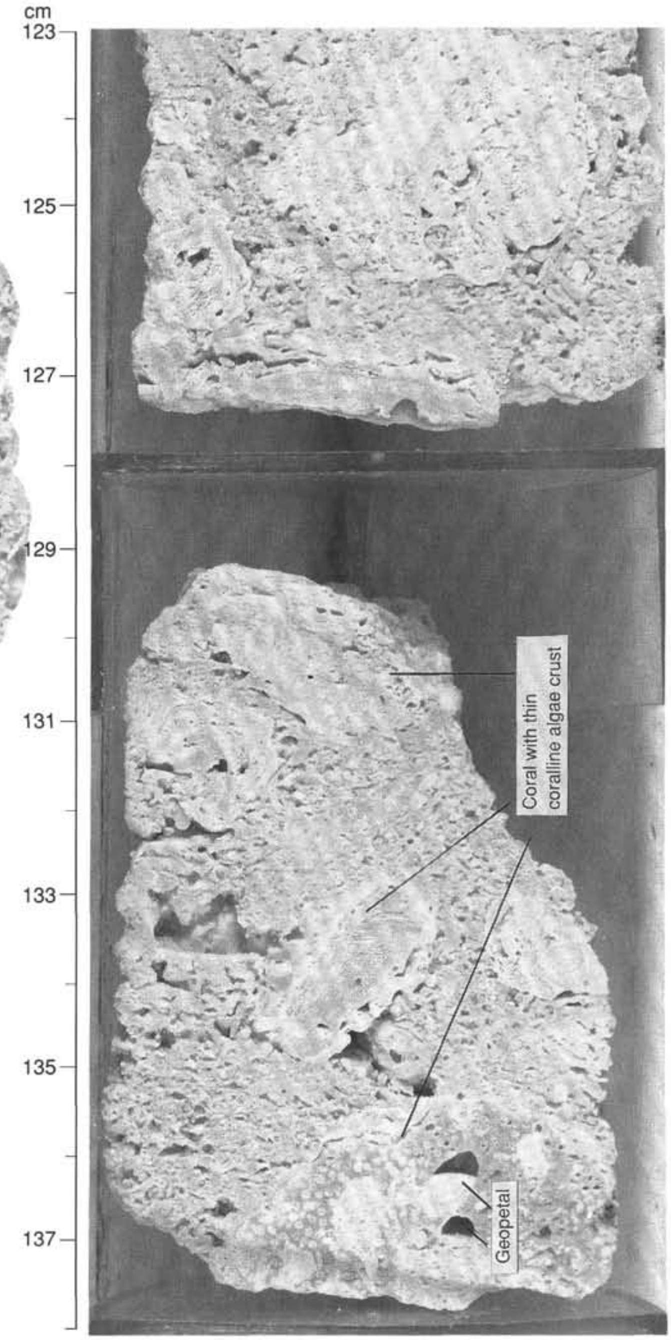

Figure 14. Photograph of a dolomitized rhodolith bearing framestone (right-hand piece) from 123–138 cm in Section 133-816C-11R-1, 222.3 mbsf) showing thin coralline algae crusts on coral fragments and bound together by *Porites*. Note the geopetal fabrics indicating up to the left.

diatus or other species of *Discoaster,* and is placed in the uppermost Pliocene nannofossil Subzone CN12d (1.88–2.29 Ma). *Discoaster tamalis, D. pentaradiatus, D. surculus,* and *D. asymmetricus* were found in Sample 133-815A-3H-CC, but *Reticulofenestra pseudoumbilica* and *Sphenolithus abies* are absent; this sample, therefore, belongs to Subzone CN12a (2.6–3.45 Ma). Sample 133-816A-4H-CC contains the highest occurrence of *Reticulofenestra pseudoumbilica* but lacks *Discoaster quinqueramus*. Based on this, the sample is placed in a combined Zone CN10–CN11 (3.5–5.26 Ma, early Pliocene).

Sample 133-816A-11H-1, 76 cm, from calcareous sands immediately above the neritic limestone, yielded a well-preserved and diverse nannofossil assemblage including *Reticulofenestra pseudoumbilica, Discoaster tamalis,* and *D. asymmetricus,* but no *D. quinqueramus* or species of *Amaurolithus*. A similarly abundant, well-preserved and diverse (>16 species) nannofossil assemblage is also present in Sample 133-816B-1R-1, 0 cm, a calcareous clay in contact with the limestone. Both assemblages can be assigned to Zones CN10–CN11 (3.5–5.26 Ma). Most likely, these assemblages belong to Zone CN11 (3.5–4.24 Ma) because no species of *Amaurolithus* is present, even though species of *Amaurolithus* occur in Zone CN10 sediments at a nearby site (Site 815).

Sample 133-816A-12X-CC (98.2 mbsf) is barren of calcareous nannofossils. The limestone and dolomite yielded no fine fraction to analyze for nannofossils. Random pulverized samples proved barren.

Planktonic Foraminifers

The upper part of Hole 816A, Samples 133-816A-1H-CC through -10H-CC, yielded abundant planktonic foraminifers and the specimens have moderate to good preservation. The sediments of this depth interval have a Pliocene to Pleistocene age; Zones N22–N23, N21, and N18–N19 were identified. No planktonic foraminifers were recovered below this section.

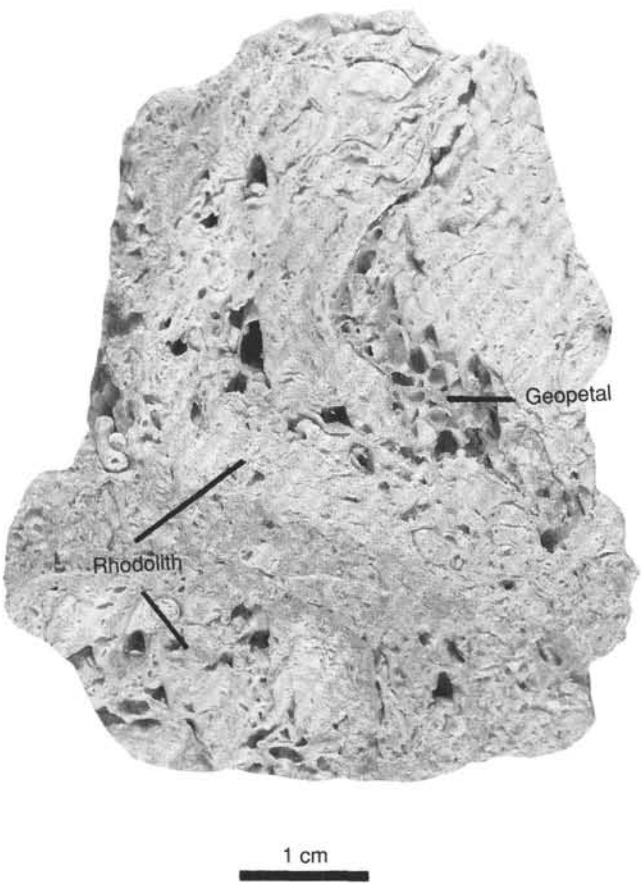

Figure 15. Photograph of large rhodolith from Unit III (85–90 cm in Section 133-816C-8R-1) showing geopetal fabrics indicating up to the left. Some mud from these cavities was examined for nannofossils in an unsuccessful attempt to obtain a nannofossil date for Unit III.

The latest occurrences of *Globigerinoides fistulosus* (1.6 Ma) and *Globigerinoides obliquus* (1.8 Ma) are in Sample 133-816A-2H-CC, just above the Pleistocene/Pliocene boundary. The lowest occurrence of *Globorotalia truncatulinoides*, marking the lower limit of Zone N22–N23, is in Core 133-816A-3H. In the core catcher of this core, the first occurrence of *Globorotalia tosaensis* was found, which implies that the zonal boundary between combined N22–N23 and N21 is in Core 133-816A-4H.

Sediments in Cores 133-816A-5H through -10H-CC can be assigned to Zone N18–N19. Its lower limit, however, defined by the first occurrence of *Globorotalia tumida tumida*, cannot be placed with certainty in Sample 133-816A-10H-CC because no planktonic foraminifers were found below.

Benthic Foraminifers

Core-catcher samples from Hole 816A above Sample 133-816A-11H-CC contain upper bathyal (200–600 m) benthic foraminifer assemblages. Preservation is excellent throughout the interval studied.

The upper bathyal benthic foraminifer assemblages contain the characteristic species associations *Bulimina marginata, B. mexicana, Cibicidoides cicatricosus, C. dutemplei, C. matanzasensis, C. mundulus, C. pachyderma, C. subhaidingerii, Hoeglundina elegans, Hyalinea balthica, Sigmoilopsis schlumbergeri*, and *Sphaeroidina bulloides* (van Morkhoven et al., 1986). Samples 133-816A-8H-CC and -10H-CC also contain *Planulina foveolata*, placing the lower depth limit of these samples at ~500 m.

Samples 133-816A-5H-CC, -8H-CC, and-10H-CC contain abundant *Ammonia* spp. in otherwise typical upper bathyal faunas. This taxon is consistently associated with shallow-water facies such as coastal bays, lagoons, and estuaries (Poag, 1981). The absence of reefal contaminants in these same samples suggests that there may have been a nearby shallow area source of *Ammonia* spp. that had no associated reef development.

Larger benthic foraminifers

Recrystallized larger foraminifers (Lepidocyclinas, *Nephrolepidina howchini*) occur in and below Sample 133-816A-11H-CC, 5–7 cm, indicating a middle Miocene age for this part of the section.

PALEOMAGNETISM

Paleomagnetic results from Hole 816A generally did not correlate with the geomagnetic polarity time scale. The uncertainty in polarity stems from the relatively weak magnetic intensities and perhaps incomplete demagnetization. Only the upper 25 m can be tentatively dated paleomagnetically with the assistance of the biostratigraphic markers. Stratigraphically, the most interesting result from the continuous archive-half measurements is that the top of the core, to about 31 mbsf has a reversed polarity after AF 15 mT demagnetization (Fig. 18). If this polarity is confirmed by shore-based study, it would indicate that part of the middle Pleistocene, and all of the upper Pleistocene is missing at this location.

The only reversal boundaries that can be identified are: (1) a clear reversal at about 31 mbsf, which is either the Matuyama/Gauss boundary, dated at 2.47 Ma or the uppermost normal subchron in the Gilbert chron; and (2) a short normal zone from ~9 to 10 mbsf, which may perhaps correlate with the Olduvai normal subchron or one of the short Reunion events below the Olduvai. However, both these boundaries must be confirmed and refined with additional study. The interval from 30 to 76 mbsf had a predominantly normal polarity after AF 15 mT demagnetization. From 76 mbsf to the underlying cemented limestone, a scattered inclination zone occurs which is of uncertain polarity. The widely scattered nature of the inclination and declination data are likely due to their weak intensities, approaching the lower measurement limit of the cryogenic magnetometer. The cemented limestones (dolomites[?]) recovered in the lower sections of Holes 816A, 816B, and 816C, were analyzed for intensity purposes only as the correct orientation of many of the pieces was unknown.

Magnetically, several distinct zones are delineated based on the change in orientation and intensity between the NRM and AF 15 mT steps. From the sediment/water interface to ~23 mbsf, a relatively strong intensity was measured, which responds very little to AF demagnetization (<10% decrease in original intensity). From ~24 to 31 mbsf, the archive-half NRM orientation data shows a steep normal inclination that switches abruptly to a moderately high reversed inclination upon AF demagnetization. A concomitant decrease in intensity also occurs in this zone after AF 15 mT. Below 31 mbsf the orientation data are considerably more stable between the NRM and AF 15 mT steps, although they remain highly scattered. These clay-rich mixed sediments between 31 mbsf and the top of the limestone are responsive to AF demagnetization, with an intensity decrease to about half the NRM value.

Zones of fine-grained pyrite (perhaps also containing some greigite) similar to those seen in Hole 815A, are common in

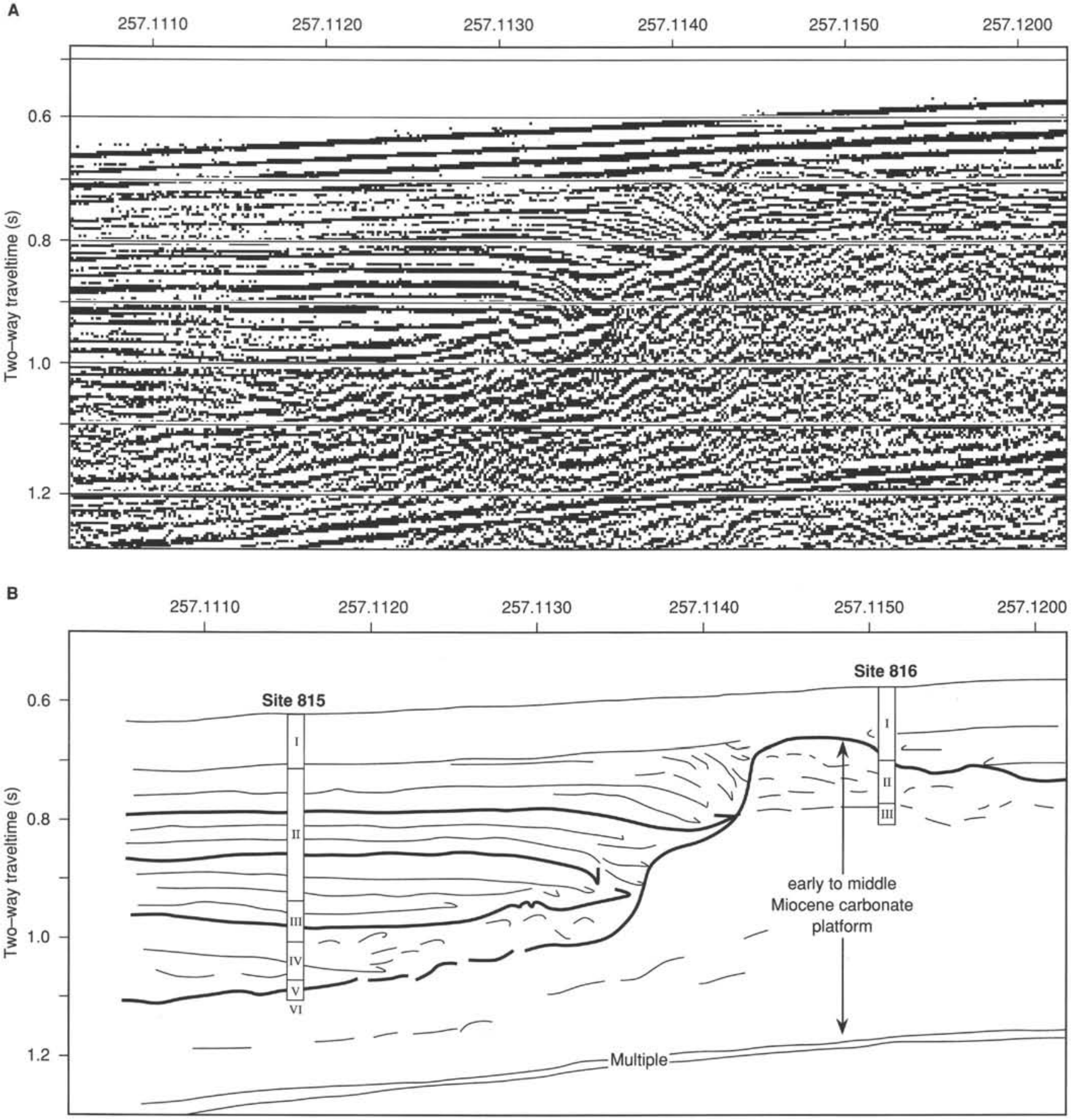

Figure 16. The unconformity at Site 816 spans from middle Miocene to lower Pliocene. **A.** Seismic stratigraphy. **B.** Comparison of Site 815 lithology with that of Site 816.

the lower 40 m of Hole 816A. Magnetic susceptibility (Fig. 19) in the uncemented sediments shows several downhole trends. From the seafloor to ~20 mbsf, the susceptibility increases rather uniformly. This upward decrease in susceptibility may be related to increased carbonate content upward from ~20 mbsf. A sharp drop to weaker susceptibility values occurs between 20 and 22 mbsf, and continues downward until about 55 mbsf. At this point the susceptibility rises gradually to the contact between the clay-rich sediments and limestone, and may reflect a secondary, diagenetic magnetic mineralogy.

SEDIMENTATION RATES

Age vs. depth is plotted for Site 816 on Figure 20. The plot includes only core-catcher samples from Hole 816A, since no plankton fossils were recovered from Holes 816B and 816C (except for Core 133-816B-1R). Sedimentation rate is relatively low at the top of the section - about 0.3 cm/k.y. for upper Pleistocene (from the Holocene to the top of the small *Gephyrocapsa* interval), increasing slightly to 0.8 cm/k.y. for the lower Pleistocene (to the highest occurrence of *Discoaster*

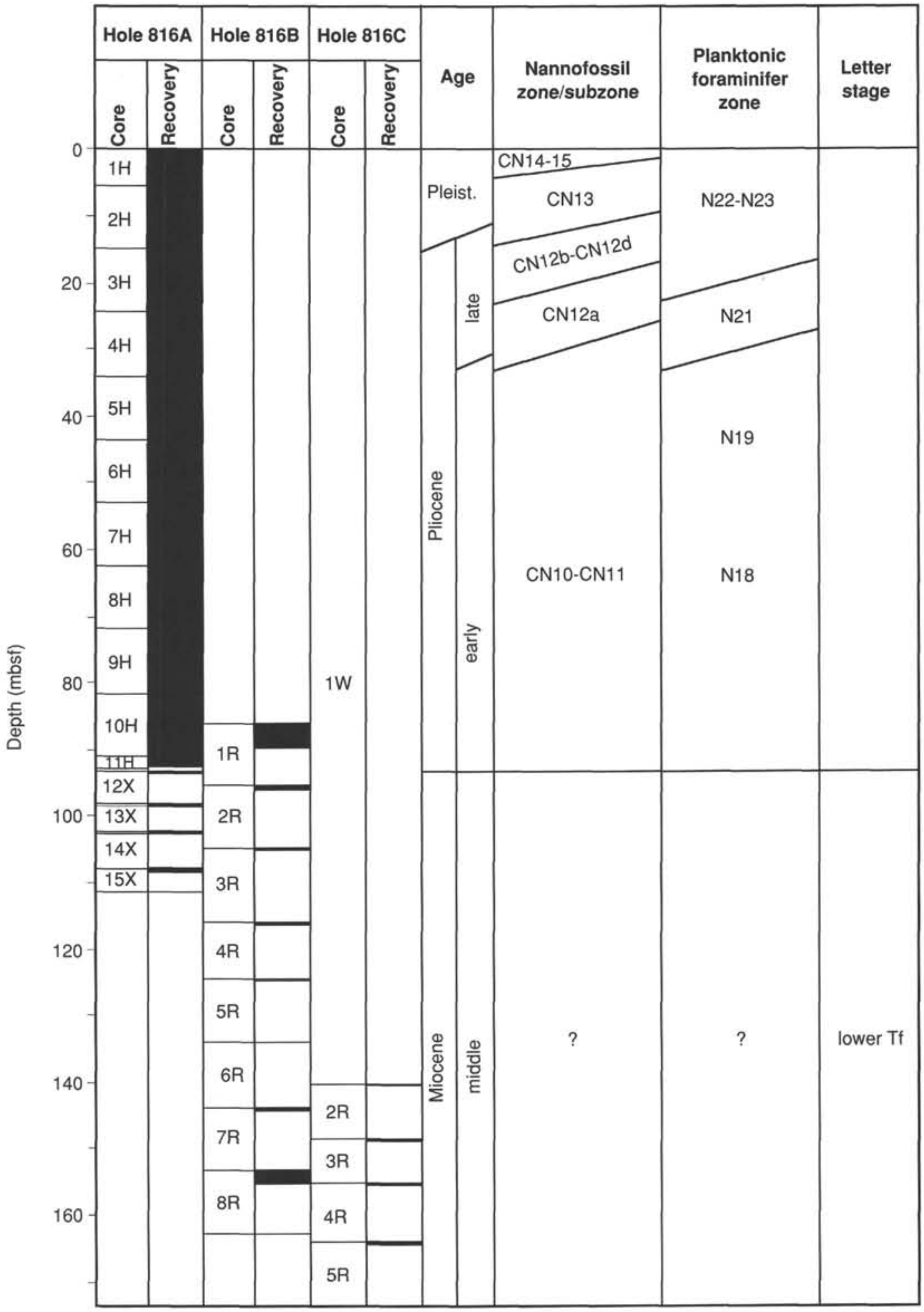

Figure 17. Summary of planktonic microfossil data from Site 816.

brouweri), to about 1.3 cm/k.y. in the upper Pliocene (to the highest occurrence of *Discoaster pentaradiatus*), and 3.4 cm/k.y. to the highest occurrence of *Sphenolithus abies*). Below this, the sedimentation rate increases by more than an order of magnitude to 47.5 cm/k.y. in the middle Pliocene (to the highest occurrence of *Reticulofenestra pseudoumbilica*). It should be noted, however, that biostratigraphic control is somewhat uncertain at this site. Even though nannofossils are relatively abundant through Core 133-816A-10H, marker species are poorly represented and poorly preserved. In addition, the relatively low sedimentation rate in the upper part of the section combined with the relatively large sample spacing may introduce a very large error. The cause for the apparent great change in sedimentation rate in the middle Pliocene is not

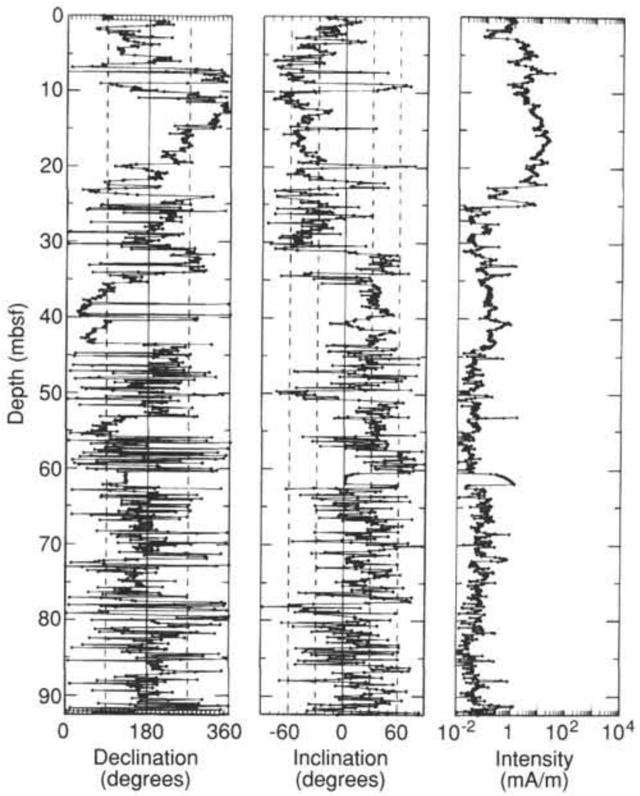

Figure 18. Whole-core magnetic data after AF 15 mT demagnetization, Site 816. The reversal boundaries are poorly defined based on shipboard data.

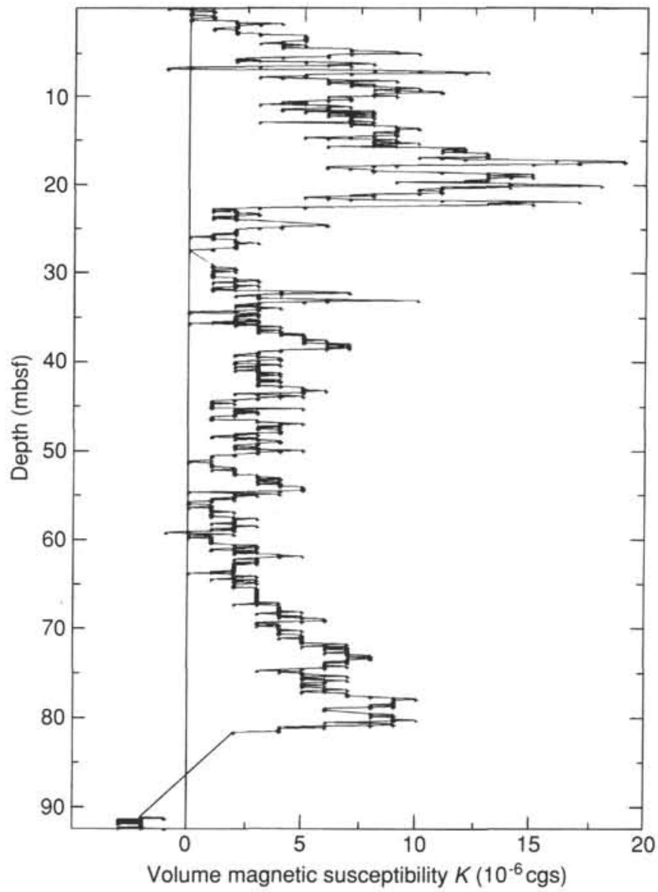

Figure 19. Continuous whole-core volume magnetic susceptibility for the unconsolidated sediments at Hole 816A.

obvious but may be clarified when further samples have been examined from this site.

INORGANIC GEOCHEMISTRY

Interstitial Waters

Interstitial water samples were taken from Cores 133-816A-1H to -10H. Samples were squeezed and analyzed according to the methods outlined in the "Explanatory Notes" (this volume).

Calcium, Magnesium, and Strontium

Calcium concentrations increase in Hole 816A from seawater values of 10.58 mM at the seafloor to 17.26 mM at 79.49 mbsf. Below this depth, Ca^{2+} concentrations appear to decrease although there is only one sample defining this trend (133-816A-10H-5, 145–150 cm; Fig. 21 and Table 2). Magnesium values decrease over the sampled interval from a seawater concentration of 53.7 mM to 47.7 mM at 79.49 mbsf. In the lower portion the values appear to increase (Fig. 21 and Table 2). The trend of Sr^{2+} concentration data is similar to that of Ca^{2+} increasing from a seawater concentration of 93–349 μM and then decreasing to 223 μM (Fig. 21 and Table 2).

The decrease in Mg^{2+} and increase in Ca^{2+} in this hole can be attributed to the formation of dolomite below 90 mbsf. The increase in Sr^{2+} results from the dissolution of aragonite and low magnesium calcite (LMC) and the precipitation of inorganic LMC within the top 90 mbsf of Hole 816A.

Chloride

Chloride concentrations increase only slightly downhole from seawater values of 542.97 to 572.24 mM.

Alkalinity, Sulfate, and pH

Alkalinity at Site 816 increases from surface-water values of 2.55 mM to ~3.2 mM for the remainder of the sampled interval (Fig. 21 and Table 2). Sulfate concentrations remain nearly constant downhole at a value of 27.5 mM (Fig. 21 and Table 2). When SO_4^{2-} is normalized to salinity by dividing SO_4^{2-} by Cl^-, an effective sulfate decrease in concentration is evident (Fig. 21). Hence, SO_4^{2-} is being utilized to oxidize organic matter in the sediments. Further reductions in SO_4^{2-} do not take place as a result of the low concentrations of organic matter in the sediments (see "Organic Geochemistry" section, this chapter).

Silica

Silica concentrations were relatively low (123–155 μM) and nearly constant with depth except for an increase at the top of the hole from seawater values of 9 μM to values of ~123 μM for the rest of the sampled interval (Fig. 21 and Table 2). The lack of pore-water silica gradients in Hole 816A result from low concentrations of siliceous microfossils in the sediments.

Carbonate Contents and X-ray Diffraction

Samples for X-ray diffraction (XRD) analyses were taken from interstitial water (IW) squeezed sediment and physical properties (PP) samples.

Aragonite concentrations rise from 0% near the top of the hole to 12.6% at 79.45 mbsf (133-816A-9H-5, 145–150 cm; Fig. 22 and Table 3). The highest aragonite concentrations are accompanied by a maxima in the interstitial strontium con-

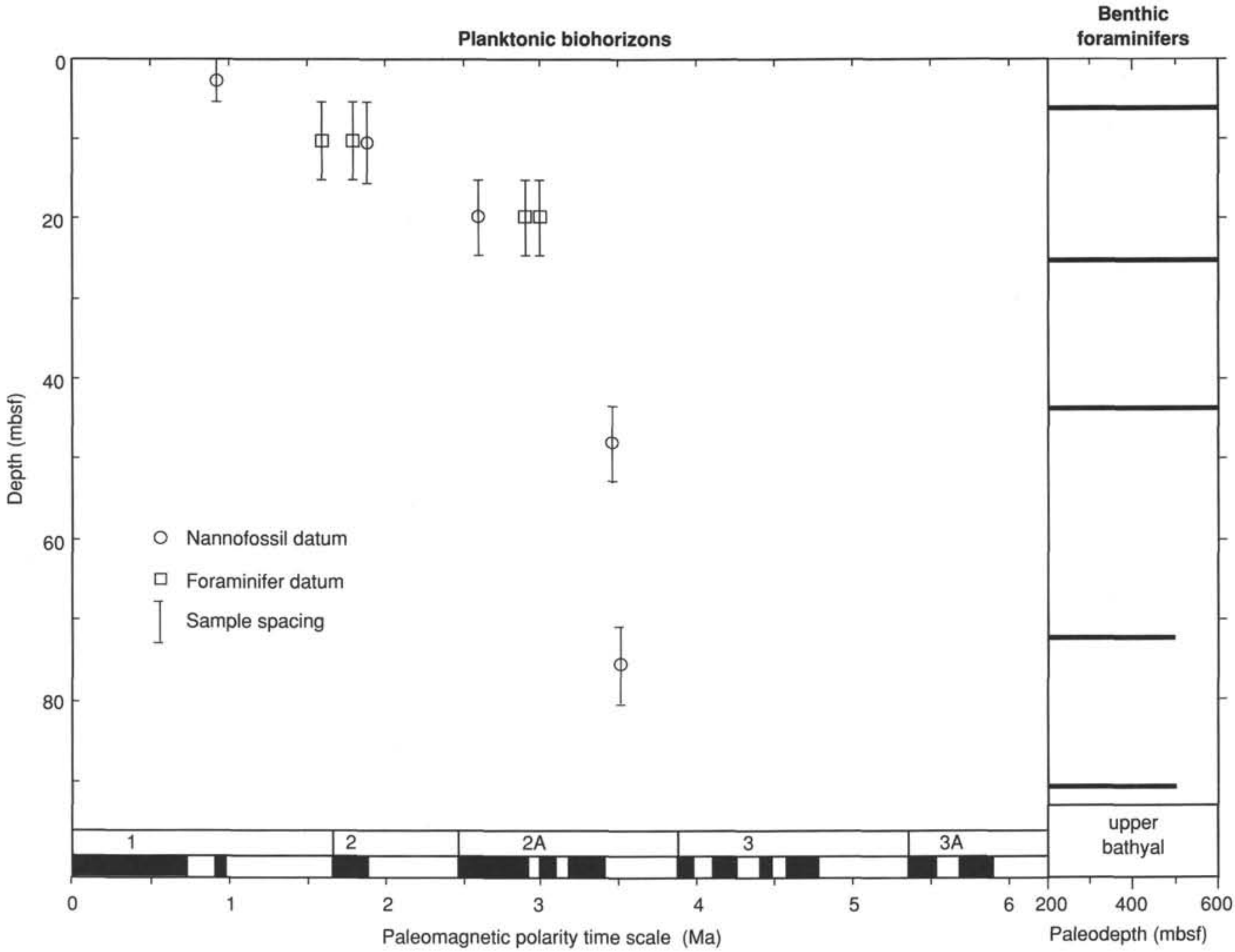

Figure 20. Age vs. depth plot for Hole 816A. All biohorizons are derived from calcareous nannofossils and planktonic foraminifers. Benthic foraminifer paleobathymetry also is shown.

centrations (Figs. 21 and 22; Tables 2 and 3). Quartz concentrations average 3%–4% for the top 60.45 mbsf of Hole 816A. From 60.45 to 88.95 mbsf the quartz concentrations range from 10% to 15.8% indicating an increased amount of terrestrial input.

The main fluctuations in mineralogy occur in the calcite and dolomite fractions of the sediment. Calcite dominates in the top 93 mbsf of Hole 816A with concentrations between 65.5% and 98.2%. Dolomite concentrations are mostly 100% below 93 mbsf (Fig. 22 and Table 3).

Calcium carbonate concentrations are variable, ranging from 50% to 90% (Fig. 23 and Table 4). The top 90-m of the hole is characterized by high-frequency fluctuations in calcium carbonate content, whereas below 90 m the carbonate rises to above 100% and remains nearly constant for the rest of the sampled section; the concentrations are over 100% as a result of the high dolomite content of the sediments.

ORGANIC GEOCHEMISTRY

In addition to safety monitoring for hydrocarbons, the main purpose of the shipboard organic geochemistry studies at Site 816 was to assess the amount and type of organic matter preserved in the Pleistocene to lower Pliocene sediments of the Marion Plateau. We determined the total nitrogen, sulfur, carbon, and the organic carbon contents of 26 additional samples collected for chromatographic analyses of the volatile hydrocarbons (headspace samples) using a NA 1500 Carlo Erba NCS analyzer.

Volatile Hydrocarbons

Light hydrocarbon gases (C_1–C_3) in sediments were analyzed routinely as part of the safety and pollution-prevention monitoring program, using the headspace technique and the Carle gas chromatograph. The results of 26 analyses from Holes 816A, 816B, and 816C are presented in Table 5.

The sediments at Site 816 contained very low concentrations of hydrocarbon gases and presented no safety problems. The concentrations of methane in the headspace gas were ~2 ppm, while ethane or propane were not detected.

Organic Carbon Contents

The total organic carbon (TOC) and total inorganic carbon contents, the total nitrogen, and sulfur concentrations recorded in Holes 816A, 816B, and 816C are presented in Table 6. We observed low to very low TOC values in the sediments, and the total nitrogen and sulfur concentrations were below the detection limits of the NCS analyzer except in Unit I. On the basis of the TOC/nitrogen ratios, the organic matter preserved in the upper bathyal clayey ooze of Unit I is a mixture of terrestrial and marine organic materials (Fig. 24).

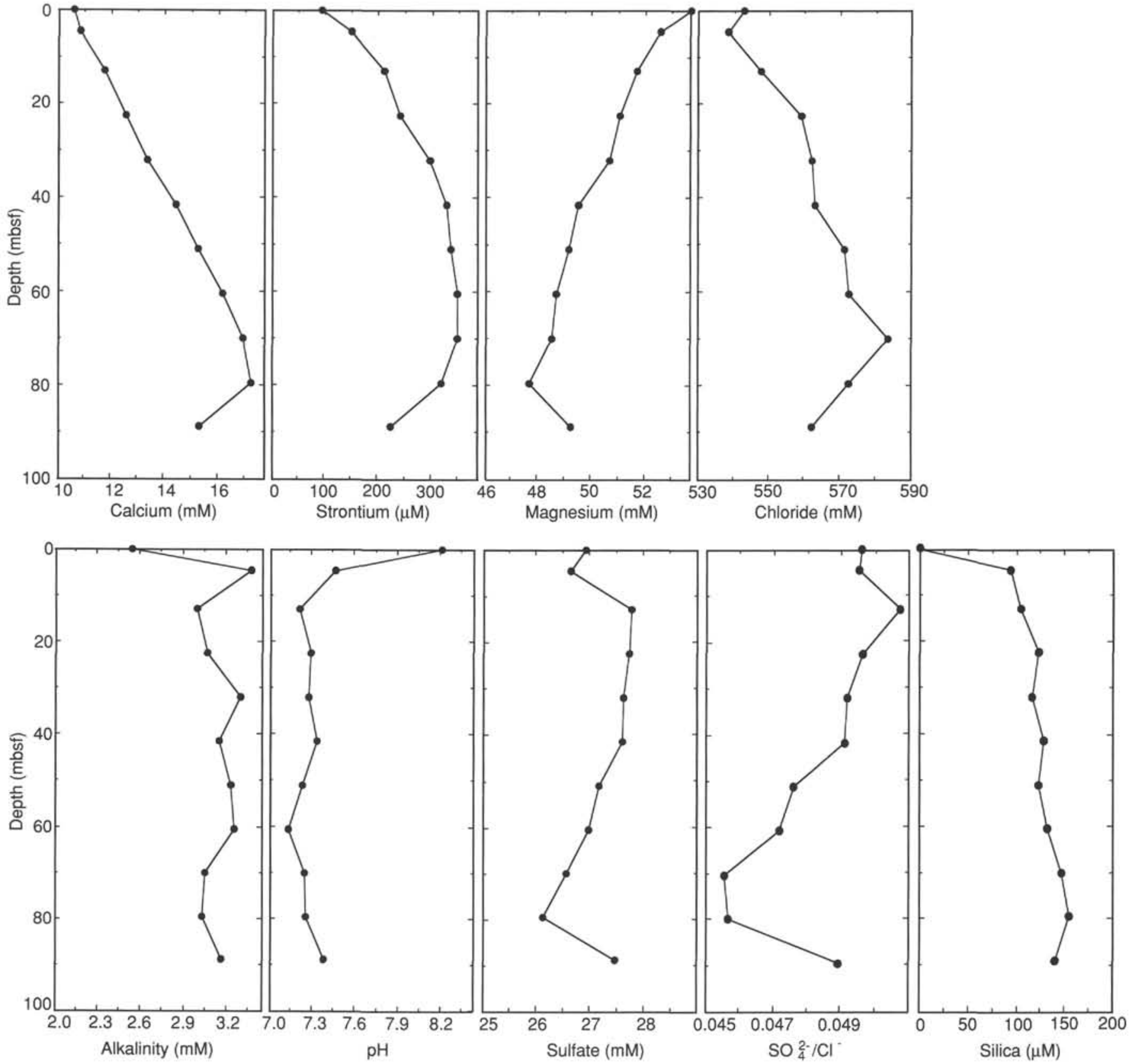

Figure 21. Calcium, strontium, magnesium, chloride, alkalinity, pH, sulfate, sulfate normalized to surface-water salinity, and silica data as a function of depth, Site 816.

Below 92 mbsf, the TOC values were low in the dolomite-rich sediments of Units II and III, progressively decreased in the partially dolomitized floatstones and mudstones of Unit II and were very low (between 0.05% and 0.20%) in the dolomitized coralgal boundstones of Unit III.

As a consequence of the low organic contents, we were unable to conduct detailed geochemical characterization of kerogen types using the Rock-Eval pyrolysis method, as originally planned. More detailed shore-based studies (as elemental analysis and optical investigations on extracted kerogens) will permit characterization of the short-term fluctuations in the vertical distribution and preservation of the different components of the organic matter in the sediments encountered at Site 816.

PHYSICAL PROPERTIES

Physical properties analyzed at this site include bulk density, *P*-wave velocity, and magnetic susceptibility on unsplit cores and *P*-wave velocity, electrical resistivity formation factor, shear strength, and index properties (including bulk density, grain density, water content, porosity, and void ratio) on split cores. The methods used are described in detail in the "Explanatory Notes" chapter of this volume. Generally poor recovery below ~90 mbsf accounts for sparse data from the lower part of the hole.

Bulk Density

Bulk densities for Site 816 were determined from volume and mass measurements on discrete core samples and from

Table 2. Interstitial water data, Hole 816A.

Core, section, interval (cm)	Depth (mbsf)	pH	Alkalinity (mM)	Salinity (g/kg)	Calcium (mM)	Magnesium (mM)	Chloride (mM)	Silica (μM)	Strontium (μM)	Sulfate (mM)
Seawater	0.00	8.22	2.546	35.8	10.58	53.72	542.97	0	93	26.93
133-816A-										
1H-3, 145–150	4.49	7.47	3.381	35.8	10.85	52.57	538.25	94	149	26.65
2H-5, 145–150	12.99	7.22	3.000	35.8	11.75	51.68	547.69	105	210	27.78
3H-5, 145–150	22.46	7.30	3.077	36.0	12.54	51.05	559.02	123	240	27.74
4H-5, 145–150	31.99	7.28	3.306	36.4	13.33	50.66	561.86	117	297	27.64
5H-5, 145–150	41.49	7.34	3.153	37.0	14.41	49.50	562.80	129	328	27.63
6H-5, 145–150	50.99	7.24	3.240	37.5	15.25	49.13	571.30	123	336	27.19
7H-5, 145–150	60.49	7.14	3.260	38.0	16.17	48.68	572.24	133	348	27.00
8H-5, 145–150	69.99	7.25	3.058	37.8	16.93	48.49	583.57	147	349	26.57
9H-5, 145–150	79.49	7.26	3.038	37.0	17.26	47.68	572.24	155	318	26.13
10H-5, 145–150	88.99	7.39	3.173	36.5	15.31	49.23	561.86	141	223	27.49

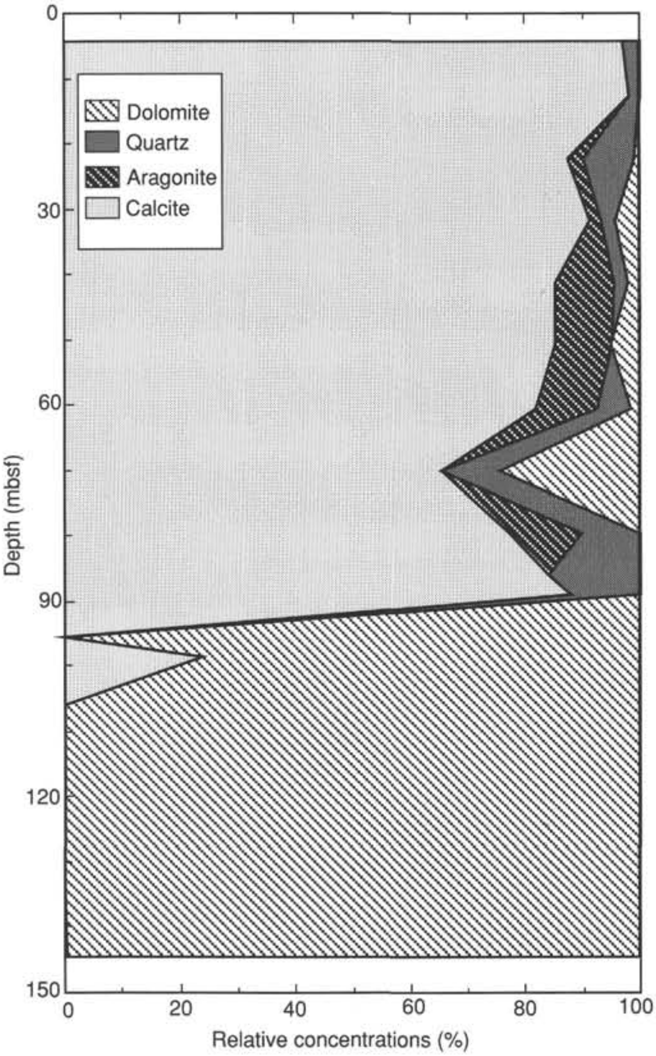

Figure 22. Mineral concentrations as a function of depth calculated as the relative concentration of calcite, aragonite, quartz, and dolomite if they are assumed to be the only mineral components in the sediments, Site 816.

gamma ray absorption by whole round cores (Figs. 25 and 26; Table 7). The downward decrease in bulk density in the upper 10–15 mbsf is probably due to dewatering of the loosely consolidated sediments as they are brought on deck and sampled. Below 15 mbsf we see the more normal downward

Table 3. X-ray diffraction data, Site 816.

Core, section, interval (cm)	Depth (mbsf)	Calcite (%)	Aragonite (%)	Quartz (%)	Dolomite (%)
133-816A-					
1H-3, 145–150	4.45	96.80	0.00	3.20	0.00
2H-5, 145–150	12.95	98.20	0.00	1.80	0.00
3H-5, 145–150	22.45	87.30	3.00	8.80	0.90
4H-5, 145–150	31.95	91.20	2.00	2.60	4.20
5H-5, 145-150	41.45	85.10	10.40	2.70	1.80
6H-5, 145–150	50.95	85.10	10.00	0.00	4.90
7H-5, 145–150	60.45	81.80	10.50	6.10	1.60
8H-5, 145-150	69.51	65.50	0.00	10.30	24.30
9H-5, 145–150	79.45	77.10	12.60	10.30	0.00
10H-5, 145–150	86.00	84.20	0.00	15.80	0.00
11H-2, 2–23	92.73	87.90	0.00	12.10	0.00
15H-1, 0–1	107.70	0.00	0.00	0.00	100.00
15H-1, 69–70	108.49	24.10	0.00	0.00	75.90
133-816B-					
1R-2, 0–1	87.50	0.00	0.00	0.00	100.00
2R-1, 0–1	95.60	0.10	0.00	0.00	99.90
3R-1, 75–78	106.50	0.10	0.00	0.00	99.90
5R-1, 9–11	124.69	0.00	0.00	0.00	100.00
7R-1, 49–50	144.49	0.40	0.00	0.00	99.60

increase in bulk density as the sediments compact because of increased overburden. Between ~50 and 75 mbsf there is a plateau in this trend of increasing bulk density. In this depth interval there is very little increase with depth. This could be due to a combination of several factors including the possible existence of an overlying low permeability zone that prevents the deeper section from dewatering and/or the presence of more sandy turbiditic layers within the zone that supports higher lithostatic loads without compacting.

P-wave Velocity

P-wave velocities were measured on whole round cores using the Multi-Sensor Track (MST) and on discrete core samples using the Hamilton Frame (Table 8; Figs. 25B and 26B). The most interesting results in physical properties at Site 816 may be in MST-derived sonic velocities where the raw data between 30 and 80 mbsf suggests a dominant spatial frequency of about 7 cycles/50 m (Figs. 25B and 26A). According to the biostratigraphy results (see "Biostratigraphy" section, this chapter), the sedimentation rate is in excess of 70 m/m.y. and our spatial velocity cycles translate to a time rate >66 cycles/m.y. or <15 k.y./cycle. We calculated a power spectra for the data of Figure 26B to look for dominant periodicities that might show up as peaks in the power spectra (Fig. 27). A peak would be expected between ~0.19 and 0.2 cycles/m. Indeed there is a peak at that location, but it does not appear to be exceptional. This suggests that the peaks

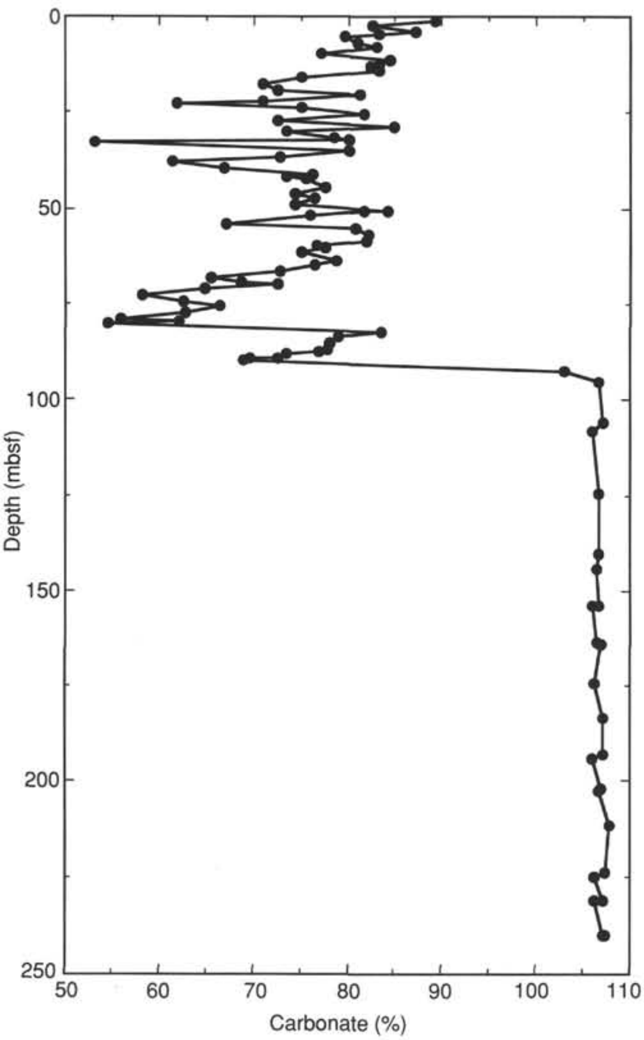

Figure 23. Carbonate data as a function of depth, Site 816.

seen in Figure 26A are only quasiperiodic. If these peaks are produced by a recurring process, the process may not be periodic. Alternatively, the sedimentation rate may not be constant.

The velocity data collected with the Hamilton Frame does not hint at the patterns seen in the MST data (Fig. 26B). This is possibly due to a combination of factors including low spatial sampling rate and further sediment disturbance that resulted from subsampling of the split core.

Porosity

Porosity was one of the index properties determined from discrete core samples using the mass balance and the pycnometer (Table 7). A graph of porosity vs. depth is shown in Figure 26D. Similarly the water content, derived from the same set of index property measurements, is also plotted in Figure 26E. Water content plotted against porosity is depicted in Figure 28A emphasizing once again the internal consistency of our mass and volume measurements that are used to calculate index properties (R = 0.915).

Electrical-Resistivity Formation Factor

We measured the formation factor (FF) at three intervals in core sections from Hole 816A (see Table 9 and Fig. 26F). In Figure 28B, we show FF vs. porosity, and in Figure 28C, we

Table 4. Carbonate data, Site 816.

Core, section, interval (cm)	Depth (mbsf)	Sample	Carbon (%)	Carbonate (%)
133-816A-				
1-H-1, 102–104	1.02	PP	10.72	89.30
1H-2, 102–104	2.52	PP	9.91	82.60
1H-3, 102–104	4.02	PP	10.48	87.30
1H-3, 149–150	4.49	HS	10.17	83.40
1H-4, 51–53	5.01	PP	9.57	79.70
2H-1, 109–111	6.59	PP	9.73	81.10
2H-2, 99–101	7.99	PP	9.97	83.10
2H-3, 101–103	9.51	PP	9.25	77.10
2H-4, 102–104	11.02	PP	10.14	84.50
2H-5, 102–104	12.52	PP	9.99	83.20
2H-5, 149–150	12.99	HS	10.45	82.50
2H-6, 102–104	14.02	PP	10.00	83.30
3H-1, 100–102	16.00	PP	9.01	75.10
3H-2, 99–101	17.49	PP	8.53	71.10
3H-3, 101–103	19.01	PP	8.71	72.60
3H-4, 101–103	20.51	PP	9.76	81.30
3H-5, 101–103	22.01	PP	8.53	71.10
3H-5, 146–147	22.46	HS	7.79	61.90
3H-6, 102–104	23.52	PP	9.02	75.10
4H-1, 101–104	25.51	PP	9.79	81.60
4H-2, 101–104	27.01	PP	8.70	72.50
4H-3, 101–104	28.51	PP	10.20	85.00
4H-4, 101–104	30.01	PP	8.81	73.40
4H-5, 101–104	31.51	PP	9.43	78.60
4H-5, 149–150	31.99	HS	10.16	80.10
4H-6, 101–104	33.01	PP	6.37	53.10
5H-1, 101–103	35.01	PP	9.62	80.10
5H-2, 101–103	36.51	PP	8.74	72.80
5H-3, 101–103	38.01	PP	7.37	61.40
5H-4, 101–103	39.51	PP	8.02	66.80
5H-5, 101–103	41.01	PP	9.16	76.30
5H-5, 149–150	41.49	HS	9.28	73.40
5H-6, 101–103	42.51	PP	9.06	75.50
6H-1, 102–105	44.52	PP	9.31	77.60
6H-2, 102–105	46.02	PP	8.94	74.50
6H-3, 102–105	47.52	PP	9.17	76.40
6H-4, 102–105	49.02	PP	8.93	74.40
6H-5, 102–105	50.52	PP	10.12	84.30
6H-5, 149–150	50.99	HS	10.24	81.60
6H-6, 102–105	52.02	PP	9.13	76.10
7H-1, 101–104	54.01	PP	8.07	67.20
7H-2, 101–104	55.51	PP	9.70	80.80
7H-3, 101–104	57.01	PP	9.87	82.20
7H-4, 101–104	58.51	PP	9.83	81.90
7H-5, 101–104	60.01	PP	9.19	76.60
7H-5, 149–150	60.49	HS	9.85	77.70
7H-6, 101–104	61.51	PP	9.02	75.10
8H-1, 101–103	63.51	PP	9.45	78.70
8H-2, 101–103	65.01	PP	9.17	76.40
8H-3, 101–103	66.51	PP	8.73	72.70
8H-4, 101–103	68.01	PP	7.86	65.50
8H-5, 101–103	69.51	PP	8.26	68.80
8H-5, 149–150	69.99	HS	9.16	72.50
8H-6, 101–103	71.01	PP	7.79	64.90
9H-1, 80–83	72.80	PP	6.97	58.10
9H-2, 80–83	74.30	PP	7.51	62.60
9H-3, 80–83	75.80	PP	7.97	66.40
9H-4, 80–83	77.30	PP	7.53	62.70
9H-5, 80–83	78.80	PP	6.71	55.90
9H-5, 149–150	79.49	HS	7.89	62.00
9H-6, 80–83	80.30	PP	6.56	54.60
10H-1, 80–82	82.30	PP	10.02	83.50
10H-2, 80–82	83.80	PP	9.48	79.00
10H-3, 80–82	85.30	PP	9.37	78.10
10H-4, 80–82	86.80	PP	9.34	77.80
133-816B-				
1R-2, 0–1	87.50	HS	9.77	77.00
133-816A-				
10H-5, 80–82	88.30	PP	8.83	73.60
10H-5, 149–150	88.99	HS	9.21	72.60
133-816B-				
1R-3, 37–40	89.37	PP	8.36	69.60

Table 4 (continued).

Core, section, interval (cm)	Depth (mbsf)	Sample	Carbon (%)	Carbonate (%)
133-816A-				
10H-6, 80–82	89.80	PP	8.27	68.90
11H-2, 23–24	92.73	HS	12.66	102.90
133-816B-				
2R-1, 0–1	95.60	HS	13.30	106.60
3R-1, 75–76	106.05	HS	13.32	107.00
816A-15X-1, 69–70	108.49	HS	13.19	105.90
816B-5R-1, 9–10	124.69	HS	13.36	106.50
816C-2R-1, 7–8	140.47	HS	13.00	106.50
816B-7R-1, 49–50	144.49	HS	13.16	106.40
133-816C-				
4R-1, 0–1	154.00	HS	13.03	106.50
4R-1, 7–10	154.07	PP	12.73	106.00
5R-1, 0–1	163.70	HS	12.77	106.30
5R-1, 75–76	164.45	PP	12.82	106.80
6R-CC, 0–2	174.63	HS	12.95	106.20
7R-1, 6–7	183.16	PP	12.90	107.00
8R-1, 61–62	193.01	PP	12.86	107.10
8R-CC, 0–1	194.31	HS	12.88	105.90
9R-1, 15–16	202.15	PP	12.81	106.70
9R-CC, 0–1	202.50	HS	13.01	106.60
10R-1, 17–18	211.47	PP	13.01	107.80
11R-2, 138–140	223.88	PP	12.88	107.30
11R-CC, 0–2	224.97	HS	12.95	106.20
12R-1, 46–47	231.16	PP	12.84	107.00
12R-1, 55–56	231.25	HS	12.91	106.20
13R-1, 0–1	240.30	HS	12.93	107.00
13R-1, 33–34	240.63	PP	12.88	107.30

show log FF vs. log porosity. Before calculating logs and plotting Figures 28B and 28C, we smoothed the data of Tables 7 and 9 with a 5-point running average followed by interpolation of the smoothed data at 1-m intervals. This permitted us to compare porosity with FF, even though they were not sampled at precisely the same depths in the hole. As with our results at Site 815, we obtained a log-log relationship with a slope of -0.3 rather than a slope in the expected range of -1 to -2 (see discussion of electrical resistivity and Archie's Law in the "Physical Properties" section, "Site 812" chapter, this volume). In the process of measuring the electrical resistivity of split cores we noticed that while the probes are embedded in the core face, the measured resistance usually changes continuously with time, not in a random way, but progressively either increasing or decreasing - usually the latter. Our recorded values are to a great extent taken at an arbitrary time during this process.

Shear Strength

We measured shear strength in the upper section of this hole (Table 10 and Figure 26G). The shear strength is fairly uniform down to about 65 mbsf where a large increase in shear strength is observed.

DOWNHOLE MEASUREMENTS

Reliability of Logs

Hole size is the most important control on accuracy of logs from Hole 816C. Three caliper logs were obtained; in order of increasing reliability, they are: an apparent caliper calculated from the sonic log (see "Explanatory Notes" chapter, this volume), the lithodensity tool caliper (Fig. 29), and the two-axes caliper of the Formation MicroScanner (FMS). The latter two are generally similar at Hole 816B, except that the FMS caliper saturates at a maximum opening of 15 in. (38.1 cm) and the lithodensity caliper saturates at 18 in. (45.7 cm). The sonic caliper was generally unreliable at Hole 816C, due to excessive noise in the sonic data.

Most of the logged interval is <15 in. (38.1 cm); as a result, almost all of the FMS run achieved pad contact with all four pads. Occasional portions of the lithodensity run obtained only marginal pad contact against the borehole wall. As a result, logs of density and photoelectric effect show some swings to unreliably low values (e.g., 134–146 mbsf in Fig. 29). We have clipped these intervals, but the clipped values are only approximately correct.

Most other logs do not require pad contact and therefore are relatively insensitive to the changes in borehole size. Two minor exceptions are the spectral gamma-ray and resistivity logs, which are likely to be changed slightly by postcruise borehole correction.

The initial sonic logs from Hole 816C exhibited many zones in which cycle skipping caused unreliable swings in apparent velocity. Indeed, this sonic log is the lowest quality of any that we obtained on Leg 133, probably because of "road noise" due to dragging the tool over rough and hard borehole wall in the reef-derived carbonates. Reprocessing (see "Explanatory Notes" chapter, this volume) substantially improved the sonic log, based on comparison of the reprocessed sonic log to resistivity (Fig. 30). However, in two intervals (87–103 mbsf and 133–155 mbsf) this comparison suggests that the sonic log is still unreliable. Consequently, we created a pseudosonic log from resistivity (Fig. 30), by regressing sonic on logarithm of resistivity and applying the regression equation to the resistivity log. We consider this technique to be valid in spite of the inclusion of some unreliable sonic data in the regression, because reliable sonic data so greatly outnumber unreliable data as to make the influence of the latter negligible.

Overlay of the reprocessed sonic with resistivity (Fig. 30) shows that the scaling that produces a good overlay (except for unreliable sonic patches) in the upper portion (72.4–163.6 mbsf) matches character but not amplitudes in the lower portion. Separate crossplots for the two intervals 72.4–163.6 mbsf and 163.8–228.9 mbsf (Fig. 31) show that they exhibit very different velocity/resistivity relationships, indicating different cementation styles. The 163.7 mbsf depth of this transition picked from the overlay of Figure 30 corresponds very closely with the ~164 mbsf depth of the Unit II/III contact (see "Lithostratigraphy" section, this chapter). We used the separate regressions for the two intervals (Fig. 31) to generate the final pseudosonic of Figure 30. We consider this pseudosonic log to be almost as good as the reprocessed sonic log in most portions of the hole, and much better in the intervals 87–103 mbsf and 133–155 mbsf.

The spectral gamma-ray tool is the only tool on the seismic stratigraphic combination that can provide useful formation data even through pipe. At Hole 816C through-pipe spectral gamma-ray logs were obtained for the interval 0–72.4 mbsf. In this interval, values for uranium and potassium are just above the resolving power of the tool and values for thorium are below the resolving power of the tool.

Velocity, Resistivity, and Density

Velocity, resistivity, and density are strongly correlated throughout almost all of the logged interval at Hole 816C (Figs. 29 and 30). Indeed, the relationship between velocity and resistivity is so strong that we preferred a pseudovelocity log based on resistivity to the reprocessed velocity log. Because lithologic changes here are relatively minor and confined to variations in relative proportions of the geophys-

Table 5. Volatile hydrocarbon data from headspace analysis at Site 816.

Core, section, interval (cm)	Depth (mbsf)	Sample	Volume (mL)	Gas chromatograph	C_1 (ppm)	C_2 (ppm)	C_3 (ppm)
133-816A-							
1H-3, 149–150	4.49	HS	5	CAR132	2	0	0
2H-5, 149–150	12.99	HS	5	CAR132	2	0	0
3H-5, 146–147	22.46	HS	5	CAR132	2	0	0
4H-5, 149–150	31.99	HS	5	CAR132	2	0	0
5H-5, 149–150	41.49	HS	5	CAR132	2	0	0
6H-5, 149–150	50.99	HS	5	CAR132	2	0	0
7H-5, 149–150	60.49	HS	5	CAR132	2	0	0
8H-5, 149–150	69.99	HS	5	CAR132	2	0	0
9H-5, 149–150	79.49	HS	5	CAR132	2	0	0
816B-1R-2, 0–1	87.5	HS	5	CAR132	2	0	0
133-816A-							
10H-5, 149–150	88.99	HS	5	CAR132	2	0	0
11H-2, 23–24	92.73	HS	5	CAR132	2	0	0
133-816B-							
2R-1, 0–1	95.6	HS	5	CAR132	2	0	0
3R-1, 75–76	106.05	HS	5	CAR132	2	0	0
816A-15X-1, 69–70	108.49	HS	5	CAR132	2	0	0
816B-5R-1, 9–10	124.69	HS	5	CAR132	2	0	0
816C-2R-1, 7–8	140.47	HS	5	CAR132	2	0	0
816B-7R-1, 49–50	144.49	HS	5	CAR132	2	0	0
133-816C-							
4R-1, 0–1	154	HS	5	CAR132	2	0	0
5R-1, 0–1	163.7	HS	5	CAR132	2	0	0
6R-CC, 0–2	174.63	HS	5	CAR132	2	0	0
8R-CC, 0–1	194.31	HS	5	CAR132	2	0	0
9R-CC, 0–1	202.5	HS	5	CAR132	2	0	0
11R-CC, 0–2	224.97	HS	5	CAR132	2	0	0
12R-1, 55–56	231.25	HS	5	CAR132	2	0	0
13R-1, 0–1	240.3	HS	5	CAR132	2	0	0

HS = headspace sample.

ically rather similar minerals dolomite and calcite, log responses are controlled almost entirely by porosity. The extremely high variability in both resistivity and velocity indicates correspondingly high variability in porosity.

The changes in velocity and density with depth (Fig. 29) generally show no evidence of a simple compaction profile, suggesting that mechanical compaction is minor in comparison to diagenesis in controlling porosity at this site. This pattern is even more extreme than that observed at Site 812, and it is the opposite to that observed at Sites 814 and 817, where mechanical compaction is the dominant control on velocity/depth and resistivity/depth patterns (see "Site 812", "Site 814", and "Site 817" chapters, this volume).

The pseudovelocity log has been converted to an integrated traveltime log (Fig. 32), to facilitate depth-to-time conversion for comparison of Site 816 data with seismic facies. For the unlogged interval between the seafloor and 72.4 mbsf, we used a simple linear interpolation between water velocity at the seafloor and the first log value at 72.4 mbsf. We subjectively estimate an error of <5 ms associated with uncertainties of velocities in the top 72.4 mbsf.

Log-Based Units

Most of lithostratigraphic Unit I (see "Lithostratigraphy" section, this chapter) was logged through pipe with the spectral gamma-ray tool. The pipe attenuation of about a factor of three, when combined with the already low proportions of uranium, potassium, and thorium, resulted in near-zero log responses for these three elements. However, the lower portion of Unit I was logged open-hole by several tools of the seismic stratigraphic and FMS tool strings. For the open-hole logged interval of 72–90 mbsf, the clayey nannofossil oozes of Unit I visibly increase in clay-mineral content uphole, based on the potassium and thorium logs (Fig. 33); velocity and resistivity correspondingly decrease (Fig. 29), because clay minerals cause higher porosities than carbonates.

The most distinctive log response within Unit I is a sudden spike to very high uranium content at 88 mbsf, decreasing back to ambient uranium concentrations by 85 mbsf. This marker bed is not at the base of Unit I, which is estimated as 90 mbsf on the basis of the cores and at 89.5–91.5 mbsf on the resistivity log. Its cause is uncertain, but the lack of a corresponding resistivity spike to low resistivity indicates that it is not caused by high organic matter, and the lack of a resistivity spike to high resistivity indicates that it is not a dolomite stringer. It may be rich in dolomite, as high uranium and high dolomite are often associated; alternatively, it may be a diagenetic horizon in which uranium mobilized in the reef facies was precipitated in the lowest pelagic facies.

The contact between Units I and II, at 89.5–91.5 mbsf on the velocity and resistivity logs (Fig. 29), is indicated by a sudden downhole decrease in porosity. This decrease may reflect the sudden change from clayey nannofossil ooze (Unit I) with little diagenesis to rhodolith-bearing floatstone and rudstone (Unit II) with extensive freshwater diagenesis (see "Lithostratigraphy" section, this chapter). Potassium, thorium, and uranium are much lower in Unit II than in Unit I (Fig. 33). Potassium and thorium are so low that they are beneath the resolving power of the spectral gamma-ray tool, as expected based on the paucity of clay minerals in the cores from Unit II (see "Lithostratigraphy" section, this chapter).

Throughout Unit II (93.0–163.7 mbsf), the very large porosity variations follow a bimodal distribution, with about four cycles of alternation between near-zero porosities (with

Table 6. Concentrations of total organic carbon, inorganic carbon, total carbon, total nitrogen, and sulfur in sediments from Site 816.

Core, section, interval (cm)	Depth (mbsf)	Sample	Total organic carbon (%)	Total inorganic carbon (%)	Total carbon (%)	Total nitrogen (%)	Toltal sulfur (%)	TOC/N	TOC/S
133-816A-1H-3, 149–150	4.49	HS	0.16	10.01	10.17	0	0.1		1.6
816C-1W-4, 58–61	5.08	PP	0.19	12.72	12.91	0	0		
816A-2H-5, 149–150	12.99	HS	0.55	9.9	10.45	0	0		
3H-5, 146–147	22.46	HS	0.36	7.43	7.79	0	0.34		1
4H-5, 149–150	31.99	HS	0.55	9.61	10.16	0	0.04		14
5H-5, 149–150	41.49	HS	0.47	8.81	9.28	0.02	0.07	23	6.7
6H-5, 149–150	50.99	HS	0.45	9.79	10.24	0	0.04		11
7H-5, 149–150	60.49	HS	0.52	9.33	9.85	0	0.19		2.7
8H-5, 149–150	69.99	HS	0.46	8.7	9.16	0.02	0.18	23	2.5
9H-5, 149–150	79.49	HS	0.45	7.44	7.89	0.03	0.18	15	2.5
816B-1R-2, 0–1	87.5	HS	0.53	9.24	9.77	0.03	0.04	17	13
816A-10H-5,149–150	88.99	HS	0.49	8.72	9.21	0	0.05		9.8
11H-2, 23–24	92.73	HS	0.31	12.35	12.66	0	0		
816B-2R-1, 0–1	95.6	HS	0.5	12.8	13.3	0	0		
3R-1, 75–76	106.05	HS	0.47	12.85	13.32	0	0		
816A-15X-1, 69–70	108.49	HS	0.48	12.71	13.19	0	0		
816B-5R-1, 9–10	124.69	HS	0.57	12.79	13.36	0	0		
816C-2R-1, 7–8	140.47	HS	0.22	12.78	13	0	0		
816B-7R-1, 49–50	144.49	HS	0.39	12.77	13.16	0	0		
816C-4R-1, 0–1	154	HS	0.24	12.79	13.03	0	0		
5R-1, 0–1	163.7	HS	0.01	12.76	12.77	0	0		
6R-CC, 0–2	174.63	HS	0.2	12.75	12.95	0	0		
7R-1, 6–7	183.16	PP	0.05	12.85	12.9	0	0		
8R-CC, 0–1	194.31	HS	0.17	12.71	12.88	0	0		
9R-CC, 0–1	202.5	HS	0.21	12.8	13.01	0	0		
10R-1, 17–18	211.47	PP	0.07	12.94	13.01	0	0		
11R-CC, 0–2	224.97	HS	0.2	12.75	12.95	0	0		
12R-1, 55–56	231.25	HS	0.16	12.75	12.91	0	0		
13R-1, 0–1	240.3	HS	0.08	12.85	12.93	0	0		

HS = headspace sample; PP = physical properties sample.

correspondingly high resistivity, velocity, and density), and high porosities (Fig. 29). Quite possibly, this bimodal character primarily reflects a bimodal initial lithostratigraphy rather than bimodal variations in diagenetic recrystallization, but post-cruise analysis of FMS data will be required to separate the two factors. Certainly substantial recrystallization has occurred in Unit II to decrease the porosity of some beds to near zero.

Unit III, 163.7–250 mbsf, is a dolomitized coralgal boundstone of reef-flat origin (see "Lithostratigraphy" section, this chapter). As previously mentioned, Unit III is very different from Unit II in its resistivity/velocity relationship. In Unit II, both resistivity and velocity are strongly affected by porosity change, implying that the higher porosity units still maintain some intergranular porosity. In contrast, in Unit III substantial porosity increases cause correspondingly substantial resistivity decreases but have only a subtle effect on velocity. This pattern in Unit III suggests a diagenetic porosity, with a high degree of pore connectivity creating conductivity pathways, while having little effect on the rigidity of the formations. Consequently, the variations in porosity, particularly those implied by resistivity, should be good indicators of variations in diagenetic dissolution. Units II and III today have rather similar porosities (e.g., Fig. 29), but the different velocity/resistivity relationships imply that Unit III experienced substantial cementation followed by dissolution.

Based primarily on resistivity log responses (e.g., Fig. 29), Unit III is composed of two subunits: 164–200 mbsf and 200–244 mbsf. The upper subunit consists of three sawtoothed cycles, each about 14 m thick, of gradually decreasing porosity capped by a sudden jump to the higher porosity of the overlying cycle. Within each cycle, the initial porosity decrease is rather smooth but the overlying low-porosity interval is more heterogeneous. The three cycles progressively evolve toward slightly lower porosities (higher resistivities). Only preliminary FMS images were available on the ship, but these images were enough to show that the lower portion of each cycle has a fine-scale porosity and the upper portion has a more vugular porosity with pores several millimeters or larger in size (see microfiche, this volume). In both FMS and resistivity log responses, each of these sawtooth cycles is similar to a cycle described at Site 812 and interpreted as reflecting sea-level changes (see "Site 812" chapter, this volume). We interpret these three cycles as most likely reflecting three cycles of small fluctuations in sea level, with associated major diagenetic impact because of the sensitivity of these reef-flat sediments to subtle changes in sea level.

The lower subunit (200–244 mbsf) of Unit III is similar to the upper subunit, except that it is characterized by more chaotic porosity changes than the upper subunit. Some sawtooth character is evident, but bed thickness is smaller and much more variable than in the upper subunit. Analysis of the processed FMS images will be required, in order to interpret the style of porosity variations at a vertical resolution 1–2 orders of magnitude higher than is obtainable from the logs of Figures 29 and 33.

Because the spectral gamma-ray tool is at the top of the long seismic stratigraphic tool string, only 18 m of spectral gamma-ray logs were obtained from the lower subunit. A major uranium peak is detected at 206 mbsf, in a thin (<2 m) highly cemented bed (Fig. 33). From this peak, uranium generally decreases uphole throughout Unit III until the low-uranium baseline of Unit II is reached. The generally higher uranium in Unit III than in Unit II, like the differing velocity/resistivity relationships, reflects the different diagenetic states of the two units. Though both are characterized by freshwater diagenesis, dolomitization is more pervasive in Unit III, and the higher uranium is associated with this

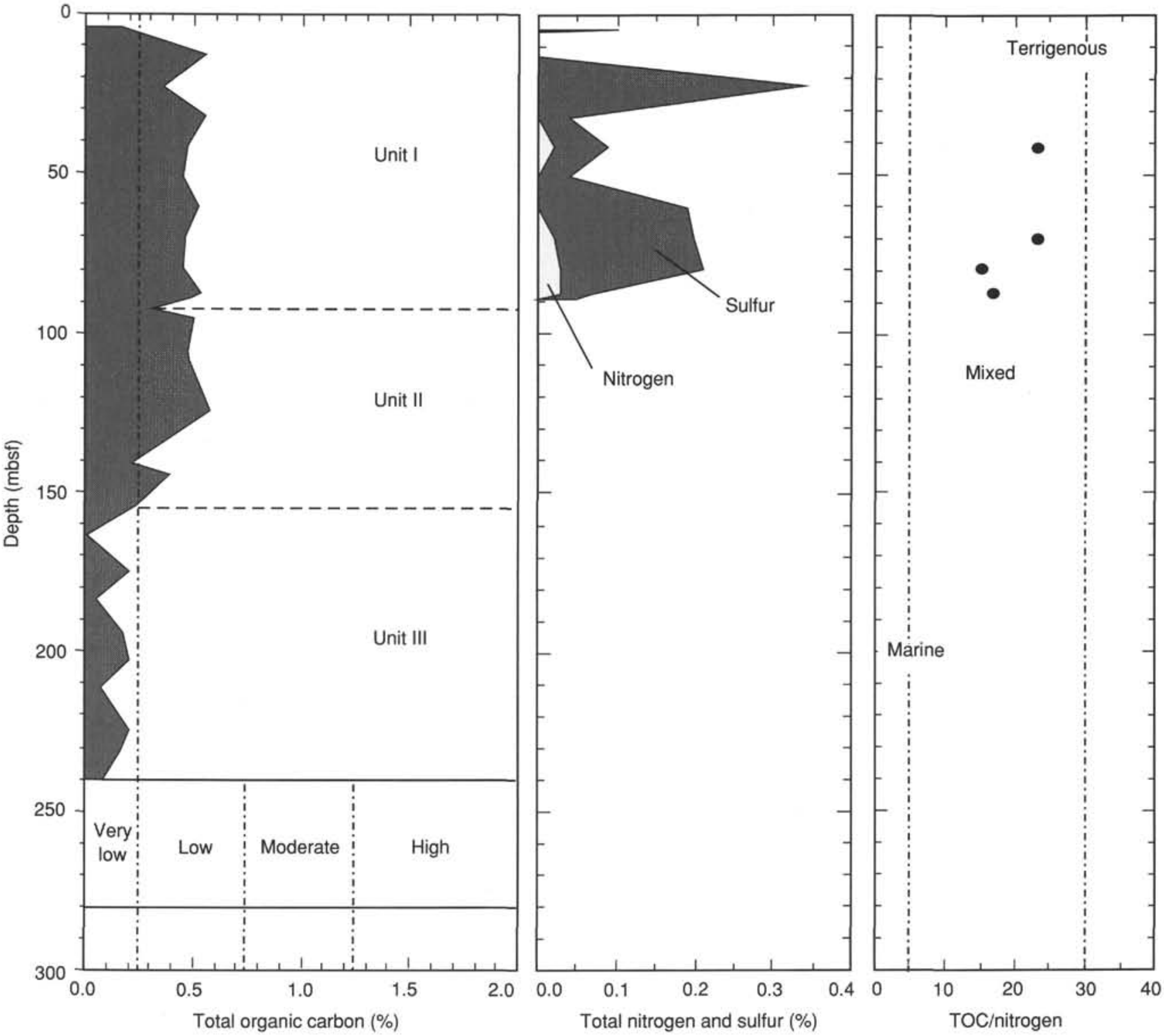

Figure 24. Distribution with depth of concentrations of total organic carbon, nitrogen, and sulfur in sediments at Site 816.

dolomitization. Similar associations were seen at Sites 812 and 814 (see "Site 812" and "Site 814" chapters, this volume).

Temperature

No heat flow measurements were made at Site 816, and thus the thermal gradient at the site is unknown. The Lamont-Doherty Geological Observatory (L-DGO) temperature tool was run at the bottom of the seismic stratigraphic tool string. Because the hole temperatures had been reduced by circulation during coring and by hole conditioning immediately prior to logging, we were unable to infer an equilibrium thermal profile from a single temperature logging run. Our recorded temperature of 17.4°C at 244 mbsf thus is a minimum estimate of equilibrium temperature.

The temperature tool was run not to estimate heat flow, but in case fluid flow was present. In Figure 34, measured temperature is plotted as a function of pressure recorded simultaneously by the tool. Depths shown are approximate and may be revised by up to 5 m by post-cruise merging of the Schlumberger time/depth data with the temperature-tool time/pressure data. The temperature pattern of Figure 34 is approximately linear between the bottom of the hole and 40–45 mbsf, but then drops rapidly to bottom-water temperatures of 14°C. This pattern is very similar to that observed at Sites 814 and 815. One possible explanation for these observations is that water is flowing up out of the lowest penetrated portion of the formation. Most of the outflow would presumably be to the seafloor. An alternative explanation is that there is no fluid flow effect on borehole temperatures, but annual variations in bottom water temperature are so large that the borehole fluids are not in thermal equilibrium with the bottom waters. We obtained borehole fluid samples with both the wireline packer and the Barnes WSTP tool, to determine if the upward flux explanation is correct. Because these samples appear to be seawater (see "Inorganic Geochemistry" section, this chapter), the fluid flux hypothesis seems less likely than the nonequilibrium hypothesis.

SEISMIC STRATIGRAPHY

The stratigraphic section at Site 816 was divided into 3 seismic sequences (Figs. 35 and 36), all of which were drilled. A brief description of each of the sequences is given below

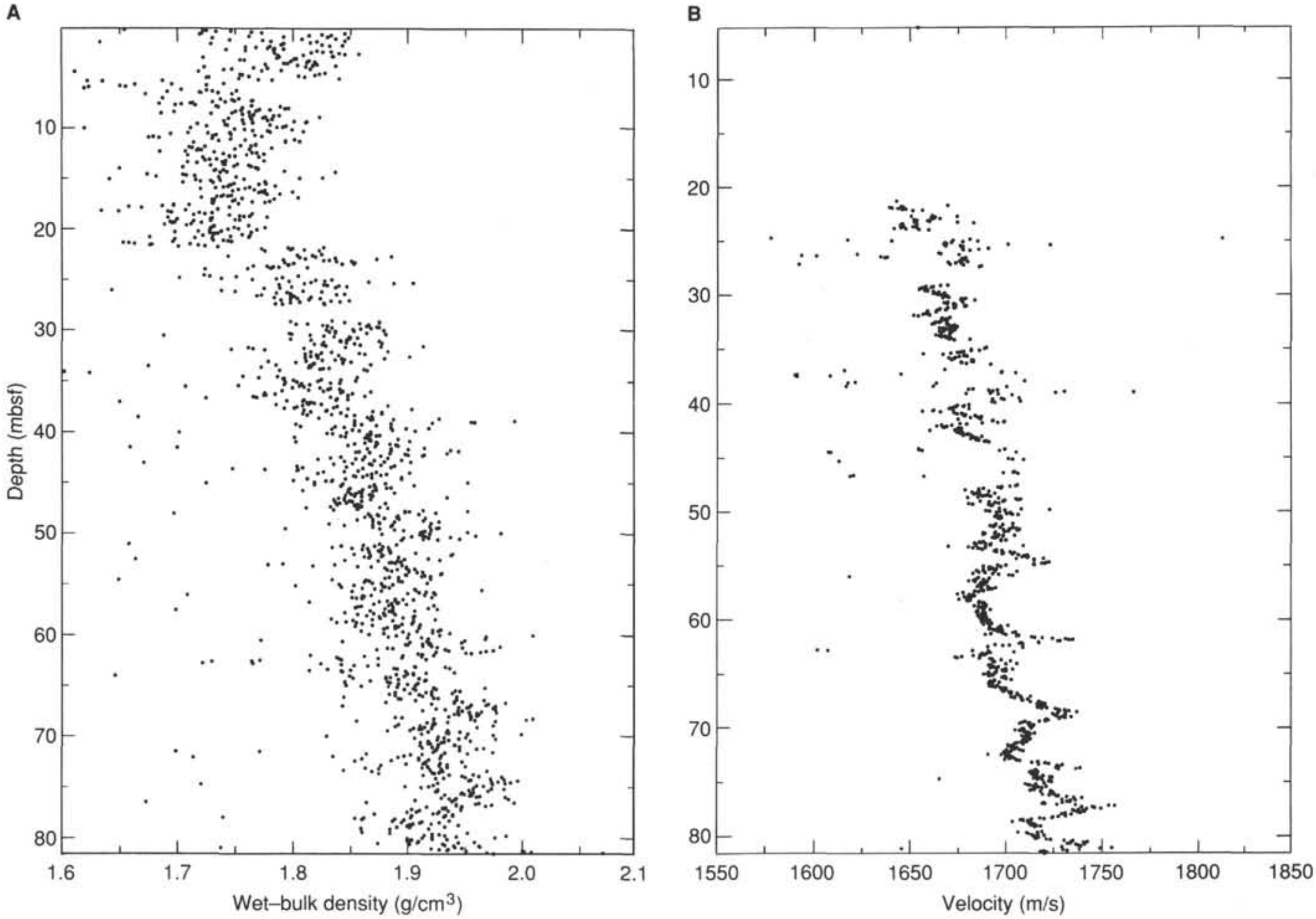

Figure 25. **A.** Unfiltered GRAPE bulk density measurements for Site 816. Due to the varying rate of motion of the core through the GRAPE system, there are often multiple measurements at the same position in the core. All data points displayed are averages of all data in 5-cm blocks along the core. **B.** MST sonic velocity for whole round cores from Hole 816A.

and in the following section they are correlated with the lithostratigraphic units encountered at the site.

Sequence 1 extends from the seafloor down ~0.115 s to 0.695 s (between 0 and 94 mbsf) at Site 816. Much of the seismic character is obscured by a strong source pulse at the seafloor but it characteristically onlaps the upper boundary of sequence 2. Sequence 1 at this site corresponds to sequence 1 at Sites 815 and 826.

Sequence 2 occurs between 0.695 and 0.750 s (between 94 and 164 mbsf). At the site the sequence is characterized by discontinuous reflectors of moderate amplitude and frequency. However, north of the site, it forms a mound, whereas to the south, the reflectors have similar amplitude and frequency, but are more continuous, wavy, and subparallel.

Sequence 3 occurs between 0.750 s and the first water bottom multiple (from 164 mbsf to TD cored the top of the sequence). The sequence is characteristically poorly to non-reflecting with some discontinuous hummocky high-amplitude, low-frequency reflectors. Sequence 3 at Site 816 is equivalent to sequence 10 at Site 815 and sequence 2 at Site 826.

Correlation with Lithostratigraphy of Site 816

There is a direct correlation between the three seismic sequences interpreted at Site 816 and the three lithostratigraphic units cored at this site (Fig. 35). Sequence 1 correlates with Unit 1 and consists of light gray, foraminiferal nannofossil ooze at the top of the section and passes down into olive green nannofossil clayey ooze at the base. The unit becomes both chalky and dolomitic toward the base. Sequence 2 correlates to Unit II and is a limestone consisting of partially dolomitized rhodolith-bearing bioclastic floatstone and rudstone. Sequence 3, which correlates with Unit III, is also a limestone and it consists of a dolomitized coralgal framestone.

The seismic stratigraphy when combined with the lithostratigraphy shows Site 816 is located on the edge of carbonate platform, with the platform slope located between Sites 815 and 816. This platform consists of an early build-up of a chlorozoan framework assemblage (sequence 3 and Unit III), which is largely responsible for the architecture of the margin. This is overlain by a mound formed by bioclastic sediments in Unit II and sequence 2 and then buried by fine-grained calcareous muds of Unit I and sequence 1.

SUMMARY

A summary of this site is presented in the "Summary" section, "Site 815" chapter (this volume).

REFERENCES

Poag, C. W., 1981. *Ecologic Atlas of Benthic Foraminifera of the Gulf of Mexico:* Stroudsburg, PA (Hutchinson Ross Publ. Co.).

Symonds, P. A., and Davies, P. J., 1988. Structure, stratigraphy, evolution and regional framework of the Townsville Trough and Marion Plateau region - research cruise proposal, project 9131.11. *Bur. Miner. Res. Aust. Rec.*, 48.

van Morkhoven, F.P.C.M., Berggren, W. A., Edwards, A. S., et al., 1986. Cenozoic cosmopolitan deep-water benthic foraminifera. *Bull. Mem. Cent. Rech. Explor.-Prod. Elf- Aquitaine Mem.*, 11.

133A-109

NOTE: All core description forms ("barrel sheets") and core photographs have been printed on coated paper and bound separately as Part 2 of this volume, beginning on page 813.

Formation microscanner images for this site are presented on microfiche in the back of Part 2.

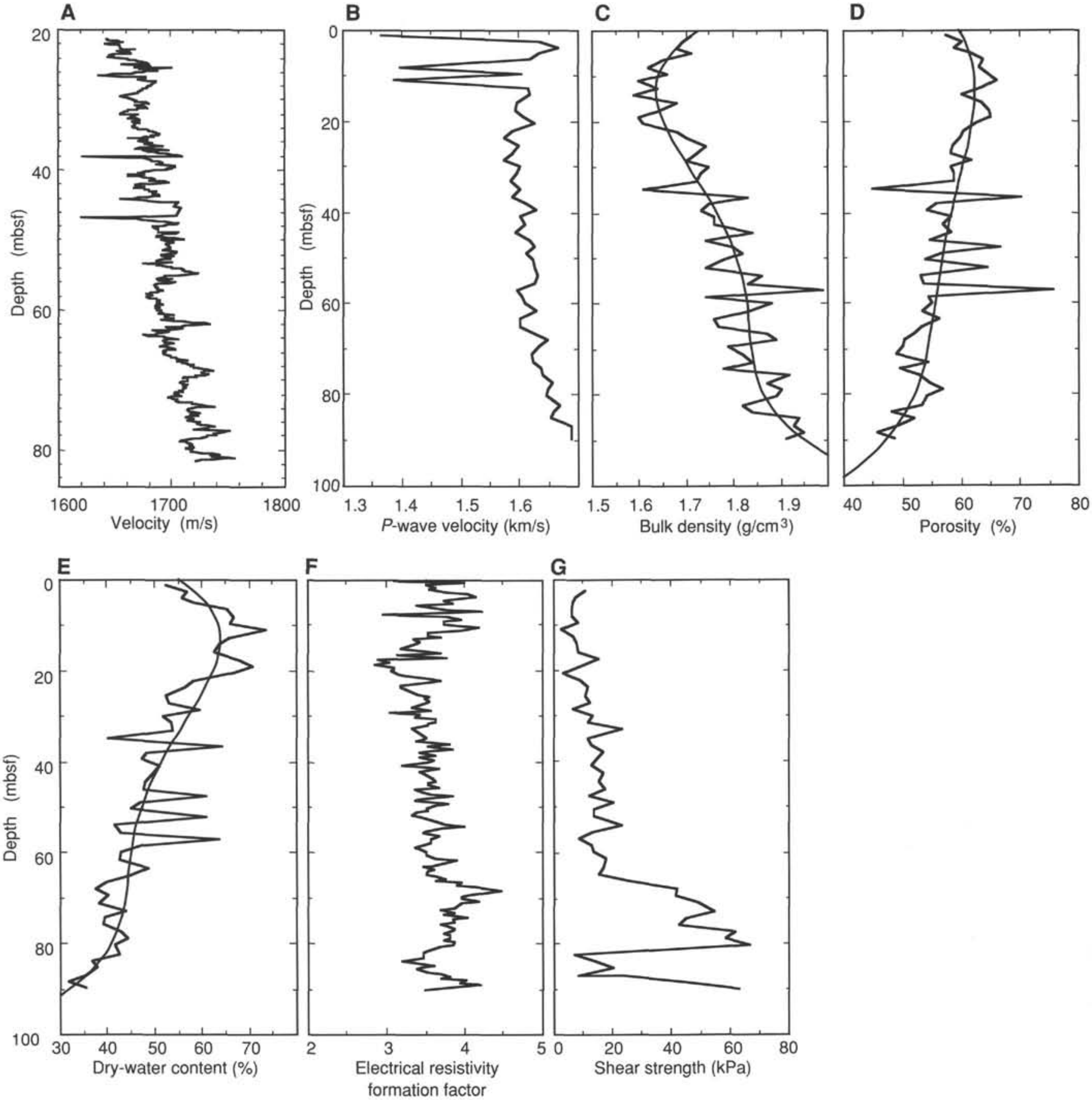

Figure 26. Physical properties data vs. depth, Site 816. **A.** MST sonic velocity; the data points of Figure 25B have been edited to remove isolated, extreme values (spikes) and duplicate measurements at the same depth have been averaged to yield one value. The output from this averaging process has been filtered with a 5-point running average and interpolated at 0.1 m intervals before plotting. **B.** *P*-wave velocity; the data are derived from Hamilton Frame measurements on discrete samples from cores. The values less than 1.5 km/s are probably due to rapid draining of permeable sands. **C.** Wet-bulk density derived from mass and volume measurements of discrete core samples (pycnometer method). The smooth curve is a fourth order regression $Y = 1.7245 - 0.015360X + 8.1955\times10^{-4}X^2 - 1.2936\times10^{-5}X^3 + 6.7046\times10^{-8}X^4$ where Y is bulk density, X is depth, and the regression coefficient R is 0.877. **D.** Porosity; the smooth curve is a fourth order regression $Y = 59.690 + 0.4622X - 2.4667\times10^{-2}X^2 + 3.897\times10^{-4}X^3 - 2.1112\times10^{-6}X^4$ where Y = porosity, X = depth, and the regression coefficient $R = 0.669$. **E.** Dry-water content, which is water content is water mass/dry sediment mass. The data are derived from mass measurements on discrete samples from cores before and after drying. The smooth curve is a fourth order least squares regression $Y = 55.208 + 1.5383X - 8.1502\times10^{-2}X^2 + 1.2844\times10^{-3}X^3 - 6.6776\times10^{-6}X^4$, where Y is dry-water content, X is depth, and the regression coefficient R is 0.854. **F.** Electrical-resistivity formation factor. **G.** Shear strength.

Table 7. Physical properties data, Hole 816A.

Core, section, interval (cm)	Depth (mbsf)	Bulk density (g/cm^3)	Grain density (g/cm^3)	Porosity (%)	Water content (%)	Void ratio
133-816A-						
1H-1, 101–104	1.01	1.71	3.00	57.3	52.3	1.34
1H-2, 101–104	2.51	1.69	2.69	60.1	57.0	1.51
1H-3, 101–104	4.01	1.68	2.66	58.8	55.9	1.43
1H-4, 51–54	5.01	1.71	2.69	61.4	58.2	1.59
2H-1, 101–104	6.51	1.65	2.74	63.7	65.3	1.75
2H-2, 101–104	8.01	1.62	2.72	63.2	66.7	1.72
2H-3, 101–104	9.51	1.66	2.68	64.5	66.1	1.82
2H-4, 101–104	11.01	1.60	2.70	66.2	73.5	1.96
2H-5, 101–104	12.51	1.64	2.72	63.5	66.0	1.74
2H-6, 101–104	14.01	1.59	2.69	60.2	63.6	1.52
3H-1, 101–104	16.01	1.68	2.70	63.3	62.8	1.73
3H-2, 101–104	17.51	1.64	2.79	64.8	68.1	1.84
3H-3, 101–104	19.01	1.60	2.72	64.9	70.9	1.85
3H-4, 101–104	20.51	1.61	2.72	62.7	66.7	1.68
3H-5, 101–104	22.01	1.68	2.69	60.4	58.1	1.53
3H-6, 101–104	23.51	1.70	2.71	59.9	56.6	1.49
4H-1, 101–104	25.51	1.74	2.78	58.4	52.3	1.40
4H-2, 101–104	27.01	1.72	2.70	58.2	53.1	1.39
4H-3, 101–104	28.51	1.70	2.67	61.9	59.6	1.62
4H-4, 101–104	30.01	1.75	2.71	58.3	51.9	1.40
4H-5, 101–104	31.51	1.73	2.73	58.8	53.5	1.43
4H-6, 101–104	33.01	1.72	2.75	58.8	53.9	1.43
5H-1, 101–104	35.01	1.61	2.70	45.0	40.3	0.82
5H-2, 101–104	36.51	1.83	2.53	70.1	64.5	2.34
5H-3, 101–104	38.01	1.75	2.75	55.9	48.5	1.27
5H-4, 101–104	39.51	1.73	2.64	54.2	47.2	1.18
5H-5, 101–104	41.01	1.76	2.69	58.2	51.2	1.39
5H-6, 101–104	42.51	1.76	2.71	56.9	49.7	1.32
6H-1, 101–104	44.51	1.84	2.85	58.3	47.9	1.40
6H-2, 101–104	46.01	1.74	2.71	54.6	47.6	1.20
6H-3, 101–104	47.51	1.80	2.35	66.7	61.1	2.00
6H-4, 101–104	49.01	1.82	2.87	57.0	47.1	1.32
6H-5, 101–104	50.51	1.78	2.70	54.0	45.0	1.17
6H-6, 101–104	52.01	1.74	2.48	64.4	60.9	1.81
7H-1, 101–104	54.01	1.86	2.76	53.1	41.4	1.13
7H-2, 101–104	55.51	1.83	2.75	53.7	42.8	1.16
7H-3, 101–104	57.01	1.99	2.78	75.6	63.8	3.09
7H-4, 101–104	58.51	1.74	2.73	54.4	47.4	1.20
7H-5, 101–104	60.01	1.88	2.68	55.0	42.8	1.22
7H-6, 101–104	61.51	1.83	2.71	53.3	42.6	1.14
8H-1, 101–104	63.51	1.76	2.73	56.4	48.8	1.29
8H-2, 101–104	65.01	1.77	2.72	53.3	44.6	1.14
8H-3, 101–104	66.51	1.87	2.70	52.1	40.0	1.09
8H-4, 101–104	68.01	1.89	2.79	50.4	37.6	1.02
8H-5, 101–104	69.51	1.79	2.72	50.1	40.2	1.00
8H-6, 101–104	71.01	1.82	2.69	49.1	38.1	0.96
9H-1, 80–84	72.80	1.84	2.20	54.5	43.8	1.20
9H-2, 80–84	74.30	1.78	2.64	49.4	39.6	0.98
9H-3, 80–84	75.80	1.92	2.71	52.9	39.2	1.12
9H-4, 80–84	77.30	1.87	2.68	54.8	42.8	1.21
9H-5, 80–84	78.80	1.90	2.69	57.0	44.3	1.33
9H-6, 80–84	80.30	1.89	2.68	54.2	41.5	1.18
10H-1, 80–84	82.30	1.82	2.72	53.2	42.7	1.14
10H-2, 80–84	83.80	1.84	2.71	48.2	36.8	0.93
10H-3, 80–84	85.30	1.94	2.64	51.9	37.7	1.08
10H-4, 80–84	86.80	1.93	2.69	49.2	35.3	0.97
10H-5, 80–84	88.30	1.95	2.73	45.7	31.6	0.84
10H-6, 80–84	89.80	1.91	3.57	48.6	35.4	0.95

Table 8. Compressional-wave velocity data, Hole 816A.

Core, section, interval (cm)	Depth (mbsf)	Distance (mm)	Traveltime (μs)	Velocity (m/s)
133-816A-				
1H-1, 101–104	1.01	26.92	22.02	1364
1H-2, 101–104	2.51	27.02	19.01	1634
1H-3, 101–104	4.01	26.58	18.42	1668
1H-4, 51–54	5.01	28.91	20.17	1634
2H-1, 101–104	6.51	27.59	19.52	1618
2H-2, 101–104	8.01	26.92	21.55	1399
2H-3, 101–104	9.51	27.62	19.68	1604
2H-4, 101–104	11.01	28.54	22.87	1387
2H-5, 101–104	12.51	28.19	19.92	1615
2H-6, 101–104	14.01	27.27	19.31	1619
3H-1, 101–104	16.01	28.37	20.23	1596
3H-2, 101–104	17.51	28.37	20.26	1594
3H-3, 101–104	19.01	28.72	20.33	1608
3H-4, 101–104	20.51	29.06	20.34	1627
3H-5, 101–104	22.01	29.20	20.85	1588
3H-6, 101–104	23.51	28.45	20.50	1576
4H-1, 101–104	25.51	28.98	20.58	1600
4H-2, 101–104	27.01	29.28	20.90	1588
4H-3, 101–104	28.51	28.72	20.69	1574
4H-4, 101–104	30.01	28.41	20.18	1603
4H-5, 101–104	31.51	28.06	20.03	1597
4H-6, 101–104	33.01	29.03	20.75	1587
5H-1, 101–104	35.01	28.15	20.02	1603
5H-2, 101–104	36.51	29.98	21.34	1588
5H-3, 101–104	38.01	28.98	20.43	1614
5H-4, 101–104	39.51	29.36	20.51	1628
5H-5, 101–104	41.01	28.98	20.54	1603
5H-6, 101–104	42.51	27.88	19.78	1610
6H-1, 101–104	44.51	29.51	20.99	1593
6H-2, 101–104	46.01	28.89	20.32	1619
6H-3, 101–104	47.51	28.36	19.92	1626
6H-4, 101–104	49.01	29.37	20.67	1614
6H-5, 101–104	50.51	28.45	19.98	1625
6H-6, 101–104	52.01	29.01	20.31	1627
7H-1, 101–104	54.01	29.15	20.34	1632
7H-2, 101–104	55.51	29.71	20.75	1626
7H-3, 101–104	57.01	29.99	21.26	1596
7H-4, 101–104	58.51	29.59	20.90	1605
7H-5, 101–104	60.01	27.67	19.66	1609
7H-6, 101–104	61.51	29.25	20.43	1630
8H-1, 101–104	63.51	28.95	20.53	1602
8H-2, 101–104	65.01	27.54	19.65	1602
8H-3, 101–104	66.51	28.80	20.22	1623
8H-4, 101–104	68.01	28.37	19.71	1647
8H-5, 101–104	69.51	28.32	19.81	1634
8H-6, 101–104	71.01	30.07	21.02	1622
9H-1, 80–83	72.80	30.55	21.28	1625
9H-2, 80–83	74.30	29.96	20.78	1638
9H-3, 80–83	75.80	30.24	20.92	1641
9H-4, 80–83	77.30	30.38	20.85	1656
9H-5, 80–83	78.80	30.57	21.05	1648
9H-6, 80–83	80.30	31.58	21.70	1645
10H-1, 80–83	82.30	28.77	19.73	1670
10H-2, 80–83	83.80	30.29	20.77	1658
10H-3, 80–83	85.30	29.98	20.62	1654
10H-4, 80–83	86.80	30.68	20.69	1688
10H-6, 80–83	89.80	29.55	20.02	1688

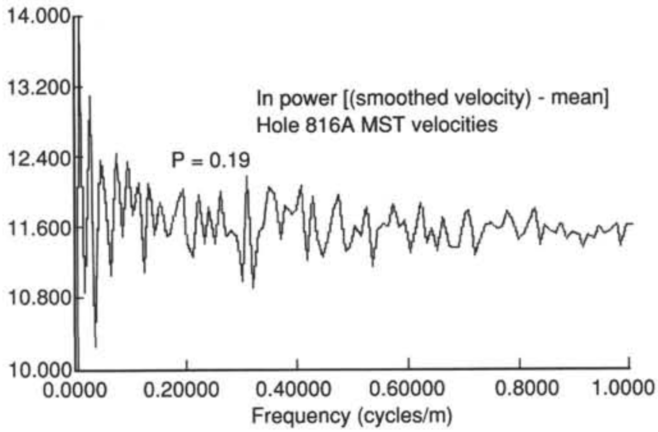

Figure 27. A power spectra of the Site 816 velocity data of Figure 26A after subtracting the mean of the data set from each data point. The letter P indicates a peak in the spectra that would correspond to the approximate periodicity of major peaks in the depth series of Figure 26A.

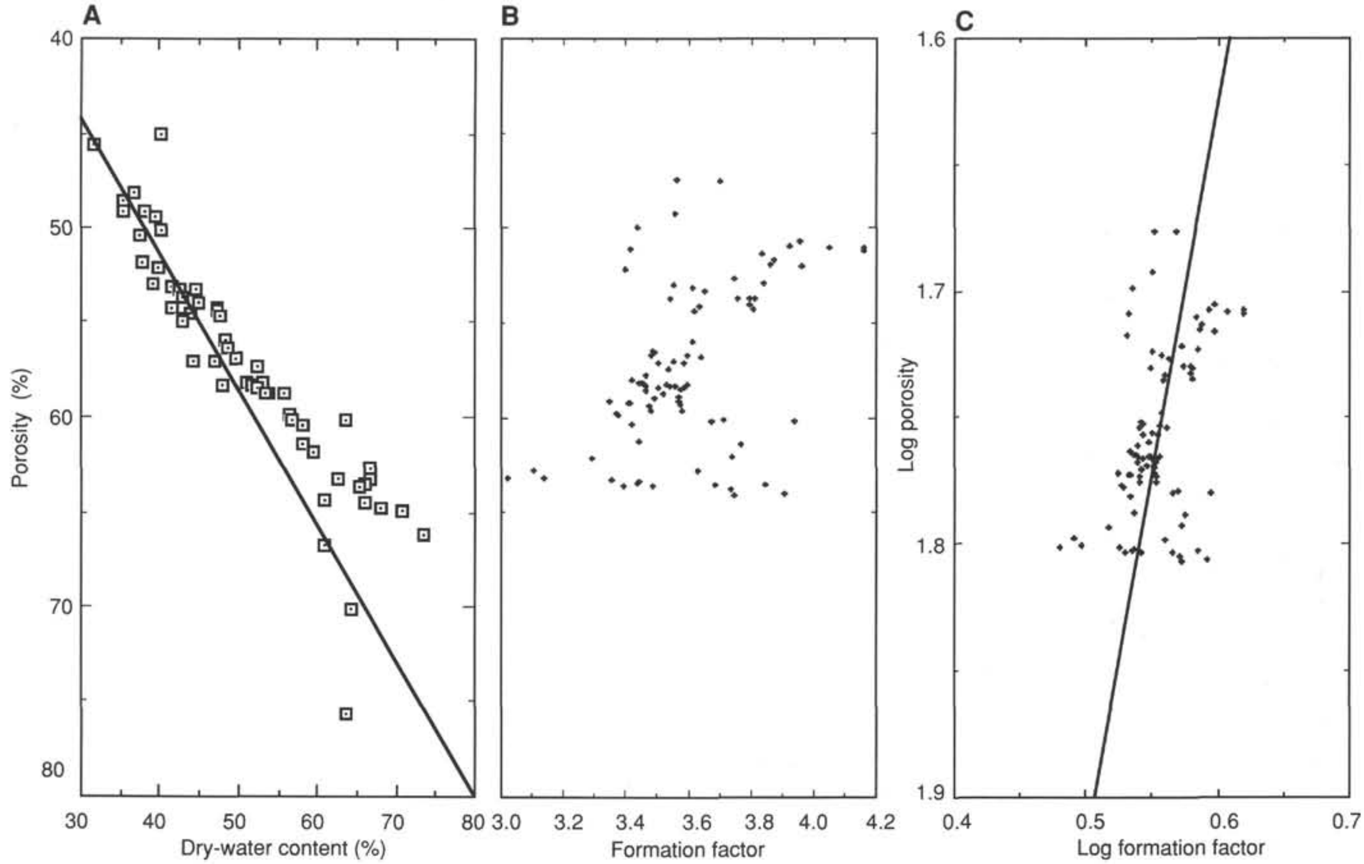

Figure 28. **A.** Dry-water content vs. porosity at Site 816. The data are derived from mass and pycnometer volume measurements on discrete samples from cores. The linear regression is of the form $Y = -41.029 + 1.6032X$ where Y is dry-water content, X is porosity, and the regression coefficient R is 0.915. **B.** FF vs. porosity. The raw data in Figures 26D and 26F were smoothed with a five-point running average and then interpolated to a 1-m spacing in depth to permit correlation of porosity with resistivity from resistivity vs. depth and porosity vs. depth series. **C.** Log FF vs. log porosity. The least-squares linear regression of FF on porosity is of the form $Y = 1.1551–0.34155X$ where Y is log FF, X is log porosity, and the linear regression coefficient R is 0.448.

Table 9. Electrical-resistivity formation factor data, Hole 816A.

Core, section, interval (cm)	Depth (mbsf)	Seawater (ohms)	Sample (ohms)	Formation factor
133-816A-				
1H-1, 20–20	0.20	2.7	8.4	3.11
1H-1, 70–70	0.70	2.7	10.8	4.00
1H-1, 120–120	1.20	2.7	9.5	3.52
1H-2, 20–20	1.70	2.7	9.8	3.63
1H-2, 70–70	2.20	2.7	9.6	3.56
1H-2, 120–120	2.70	2.7	10.2	3.78
1H-3, 20–20	3.20	2.6	10.5	4.04
1H-3, 70–70	3.70	2.6	10.8	4.15
1H-3, 120–120	4.20	2.6	10.3	3.96
1H-4, 20–20	4.70	2.6	9.7	3.73
1H-4, 70–70	5.20	2.6	10.0	3.85
2H-1, 18–18	5.68	2.6	8.8	3.38
2H-1, 120–120	6.70	2.6	9.8	3.77
2H-2, 20–20	7.20	2.6	11.0	4.23
2H-2, 70–70	7.70	2.6	7.7	2.96
2H-2, 120–120	8.20	2.6	9.8	3.77
2H-3, 20–20	8.70	2.6	10.3	3.96
2H-3, 70–70	9.20	2.6	9.7	3.73
2H-3, 120–120	9.70	2.6	9.7	3.73
2H-4, 20–20	10.20	2.6	10.2	3.92
2H-4, 70–70	10.70	2.6	10.9	4.19
2H-4, 120–120	11.20	2.6	10.3	3.96
2H-5, 20–20	11.70	2.6	9.2	3.54
2H-5, 70–70	12.20	2.6	9.2	3.54
2H-5, 120–120	12.70	2.6	9.6	3.69
2H-6, 20–20	13.20	2.6	8.7	3.35
2H-6, 70–70	13.70	2.6	8.9	3.42
2H-6, 120–120	14.20	2.6	8.8	3.38
3H-1, 20–20	15.20	2.7	8.6	3.19
3H-1, 70–70	15.70	2.7	9.6	3.56
3H-1, 120–120	16.20	2.7	10.0	3.70
3H-2, 20–20	16.70	2.7	8.5	3.15
3H-2, 70–70	17.20	2.7	10.2	3.78
3H-2, 120–120	17.70	2.7	7.8	2.89
3H-3, 20–20	18.20	2.7	8.2	3.04
3H-3, 70–70	18.70	2.7	7.7	2.85
3H-3, 120–120	19.20	2.7	8.4	3.11
3H-4, 20–20	19.70	2.7	8.4	3.11
3H-4, 70–70	20.20	2.7	8.3	3.07
3H-4, 120–120	20.70	2.7	8.5	3.15
3H-5, 20–20	21.20	2.7	8.7	3.22
3H-5, 70–70	21.70	2.7	9.6	3.56
3H-5, 110–110	22.10	2.7	10.0	3.70
3H-6, 20–20	22.70	2.7	9.6	3.56
3H-6, 70–70	23.20	2.7	8.6	3.19
3H-6, 120–120	23.70	2.7	8.6	3.19
4H-1, 20–20	24.70	0.0	0.0	0.00
4H-1, 70–70	25.20	2.7	9.2	3.41
4H-1, 120–120	25.70	2.7	9.6	3.56
4H-2, 20–20	26.20	2.7	9.4	3.48
4H-2, 70–70	26.70	2.7	9.6	3.56
4H-2, 120–120	27.20	2.7	9.5	3.52
4H-3, 20–20	27.70	2.8	9.5	3.39
4H-3, 70–70	28.20	2.8	9.3	3.32
4H-3, 120–120	28.70	2.8	10.0	3.57
4H-4, 20–20	29.20	2.8	8.5	3.04
4H-4, 70–70	29.70	2.8	9.6	3.43
4H-4, 120–120	30.20	2.8	9.4	3.36
4H-5, 20–20	30.70	2.8	10.2	3.64
4H-5, 70–70	31.20	2.8	10.2	3.64
4H-5, 120–120	31.70	2.8	9.9	3.54
4H-6, 20–20	32.20	2.8	9.9	3.54
4H-6, 70–70	32.70	2.8	9.3	3.32
4H-6, 120–120	33.20	2.8	9.4	3.36
5H-1, 20–20	34.20	0.0	0.0	0.00
5H-1, 70–70	34.70	2.8	9.8	3.50
5H-1, 120–120	35.20	2.8	9.7	3.46
5H-2, 20–20	35.70	2.8	9.5	3.39
5H-2, 70–70	36.20	2.8	10.7	3.82
5H-2, 120–120	36.70	2.8	9.9	3.54
5H-3, 20–20	37.20	2.8	10.8	3.86
5H-3, 70–70	37.70	2.8	10.0	3.57
5H-3, 120–120	38.20	2.8	9.6	3.43
5H-4, 20–20	38.70	2.8	10.2	3.64

Table 9 (continued).

Core, section, interval (cm)	Depth (mbsf)	Seawater (ohms)	Sample (ohms)	Formation factor
5H-4, 70–70	39.20	2.8	9.6	3.43
5H-4, 120–120	39.70	2.8	10.1	3.61
5H-5, 20–20	40.20	2.8	9.9	3.54
5H-5, 70–70	40.70	2.8	9.0	3.21
5H-5, 120–120	41.20	2.8	9.7	3.46
5H-6, 20–20	41.70	2.8	10.3	3.68
5H-6, 70–70	42.20	2.8	9.6	3.43
5H-6, 120–120	42.70	2.8	9.7	3.46
6H-1, 30–30	43.80	2.7	9.7	3.59
6H-1, 70–70	44.20	2.8	10.2	3.64
6H-1, 120–120	44.70	2.8	9.9	3.54
6H-2, 20–20	45.20	2.8	9.9	3.54
6H-2, 70–70	45.70	2.8	10.3	3.68
6H-2, 120–120	46.20	2.8	9.4	3.36
6H-3, 20–20	46.70	2.8	9.7	3.46
6H-3, 70–70	47.20	2.8	10.0	3.57
6H-3, 120–120	47.70	2.8	10.8	3.86
6H-4, 20–20	48.20	2.8	9.6	3.43
6H-4, 70–70	48.70	2.8	9.4	3.36
6H-4, 120–120	49.20	2.8	10.6	3.79
6H-5, 20–20	49.70	2.8	10.2	3.64
6H-5, 70–70	50.20	2.8	9.8	3.50
6H-5, 120–120	50.70	2.8	9.9	3.54
6H-6, 20–20	51.20	2.8	9.5	3.39
6H-6, 70–70	51.70	2.8	9.3	3.32
6H-6, 120–120	52.20	2.8	9.6	3.43
7H-1, 30–30	53.30	2.8	10.2	3.64
7H-1, 70–70	53.70	2.8	10.5	3.75
7H-1, 120–120	54.20	2.8	11.2	4.00
7H-2, 20–20	54.70	2.8	10.4	3.71
7H-2, 70–70	55.20	2.8	9.8	3.50
7H-2, 120–120	55.70	2.8	9.7	3.46
7H-3, 20–20	56.20	2.8	10.3	3.68
7H-3, 70–70	56.70	2.8	10.2	3.64
7H-3, 120–120	57.20	2.8	10.0	3.57
7H-4, 20–20	57.70	2.8	10.0	3.57
7H-4, 70–70	58.20	2.8	9.8	3.50
7H-4, 120–120	58.70	2.8	9.4	3.36
7H-5, 20–20	59.20	2.8	9.6	3.43
7H-5, 70–70	59.70	2.8	9.8	3.50
7H-5, 120–120	60.20	2.8	9.8	3.50
7H-6, 20–20	60.70	2.8	9.8	3.50
7H-6, 70–70	61.20	2.8	10.2	3.64
7H-6, 120–120	61.70	2.8	10.9	3.89
8H-1, 50–50	63.00	2.8	10.0	3.57
8H-1, 70–70	63.20	2.8	9.7	3.46
8H-1, 120–120	63.70	2.8	10.1	3.61
8H-2, 20–20	64.20	2.8	9.9	3.54
8H-2, 70–70	64.70	2.8	9.8	3.50
8H-2, 120–120	65.20	2.8	10.2	3.64
8H-3, 20–20	65.70	2.8	10.5	3.75
8H-3, 70–70	66.20	2.8	10.2	3.64
8H-3, 120–120	66.70	2.8	11.1	3.96
8H-4, 20–20	67.20	2.8	10.9	3.89
8H-4, 70–70	67.70	2.8	11.6	4.14
8H-4, 120–120	68.20	2.8	12.5	4.46
8H-5, 20–20	68.70	2.8	12.1	4.32
8H-5, 70–70	69.20	2.8	11.3	4.04
8H-5, 120–120	69.70	2.8	11.1	3.96
8H-6, 20–20	70.20	2.8	11.1	3.96
8H-6, 70–70	70.70	2.8	11.7	4.18
8H-6, 120–120	71.20	2.7	10.7	3.96
9H-1, 20–20	72.20	2.6	10.1	3.88
9H-1, 70–70	72.70	2.6	9.6	3.69
9H-1, 120–120	73.20	2.6	10.1	3.88
9H-2, 20–20	73.70	2.6	9.7	3.73
9H-2, 70–70	74.20	2.6	10.5	4.04
9H-2, 120–120	74.70	2.6	10.0	3.85
9H-3, 20–20	75.20	2.6	10.1	3.88
9H-3, 70–70	75.70	2.6	9.6	3.69
9H-3, 120–120	76.20	2.6	9.8	3.77
9H-4, 20–20	76.70	2.6	10.1	3.88
9H-4, 70–70	77.20	2.6	10.0	3.85
9H-4, 120–120	77.70	2.6	9.7	3.73
9H-5, 20–20	78.20	2.6	9.9	3.81
9H-5, 70–70	78.70	2.6	9.9	3.81
9H-5, 112–112	79.12	2.6	9.7	3.73

Table 9 (continued).

Core, section, interval (cm)	Depth (mbsf)	Seawater (ohms)	Sample (ohms)	Formation factor
9H-6, 20–20	79.70	2.6	10.1	3.88
9H-6, 70–70	80.20	2.6	10.0	3.85
9H-6, 120–120	80.70	2.6	9.6	3.69
10H-1, 20–20	81.70	2.9	10.2	3.52
10H-1, 70–70	82.20	2.8	9.7	3.46
10H-1, 120–120	82.70	2.8	9.7	3.46
10H-2, 20–20	83.20	3.0	10.4	3.47
10H-2, 70–70	83.70	3.0	9.6	3.20
10H-2, 120–120	84.20	2.9	9.7	3.34
10H-3, 20–20	84.70	2.8	10.1	3.61
10H-3, 70–70	85.20	2.9	10.0	3.45
10H-3, 120–120	85.70	2.9	9.8	3.38
10H-4, 20–20	86.20	3.0	10.6	3.53
10H-4, 70–70	86.70	2.9	10.7	3.69
10H-4, 120–120	87.20	2.8	10.7	3.82
10H-5, 20–20	87.70	3.0	11.1	3.70
10H-5, 70–70	88.20	2.9	11.7	4.03
10H-5, 120–120	88.70	2.9	11.4	3.93
10H-6, 20–20	89.20	2.9	12.2	4.21
10H-6, 70–70	89.70	2.9	10.7	3.69
10H-6, 120–120	90.20	2.9	10.1	3.48

Table 10. Vane shear strength data, Hole 816A.

Core, section, interval (cm)	Depth (mbsf)	Spring number	Torque (degrees)	Strain (degrees)	Shear strength (kPa)
133-816A-					
1H-2, 90–91	2.40	1	51	16	10.8
1H-3, 90–91	3.90	1	36	23	7.6
1H-4, 40–41	4.90	1	31	21	6.6
2H-1, 95–96	6.45	1	30	21	6.4
2H-2, 94–95	7.94	1	29	18	6.2
2H-3, 90–91	9.40	1	39	21	8.3
2H-4, 90–91	10.90	1	11	8	2.3
2H-5, 90–91	12.40	1	32	22	6.8
2H-6, 90–91	13.90	1	37	21	7.9
3H-1, 90–91	15.90	1	38	25	8.1
3H-2, 90–91	17.40	1	73	22	15.5
3H-3, 90–91	18.90	1	48	25	10.2
3H-4, 90–91	20.40	1	16	20	3.4
3H-5, 90–91	21.90	1	44	20	9.3
3H-6, 90–91	23.40	1	55	18	11.7
4H-1, 90–91	25.40	1	51	23	10.8
4H-2, 90–91	26.90	1	59	21	12.5
4H-3, 90–91	28.40	1	32	18	6.8
4H-4, 90–91	29.90	1	62	22	13.2
4H-5, 90–91	31.40	1	54	22	11.5
4H-6, 90–91	32.90	1	109	25	23.1
5H-1, 90–91	34.90	1	54	22	11.5
5H-2, 90–91	36.40	1	61	24	12.9
5H-3, 90–91	37.90	1	81	25	17.2
5H-4, 90–91	39.40	1	70	24	14.9
5H-5, 90–91	40.90	1	61	22	12.9
5H-6, 90–91	42.40	1	80	22	17.0
6H-1, 90–91	44.40	1	73	22	15.5
6H-2, 90–91	45.90	1	82	23	17.4
6H-3, 90–91	47.40	1	56	23	11.9
6H-4, 90–91	48.90	1	95	25	20.2
6H-5, 90–91	50.40	1	64	24	13.6
6H-6, 90–91	51.90	1	64	24	13.6
7H-1, 90–91	53.90	1	110	20	23.3
7H-2, 90–91	55.40	1	63	20	13.4
7H-3, 90–91	56.90	1	41	21	8.7
7H-4, 90–91	58.40	1	61	18	12.9
7H-5, 90–91	59.90	1	64	18	13.6
7H-6, 90–91	61.40	1	85	21	18.0
8H-1, 90–91	63.40	1	81	22	17.2
8H-2, 90–91	64.90	1	72	24	15.3
8H-3, 90–91	66.40	1	122	25	25.9
8H-4, 90–91	67.90	1	197	19	41.8
8H-5, 90–91	69.40	4	35	18	41.6
8H-6, 94–95	70.94	4	41	16	48.8
9H-1, 94–95	72.94	4	46	15	54.7
9H-2, 94–95	74.44	4	38	16	45.2
9H-3, 94–95	75.94	4	36	14	42.8
9H-4, 94–95	77.44	4	52	16	61.8
9H-5, 94–95	78.94	4	49	12	58.3
9H-6, 94–95	80.44	4	56	12	66.6
10H-1, 94–95	82.44	4	6	5	7.1
10H-2, 94–95	83.94	4	12	13	14.3
10H-3, 96–97	85.46	4	17	17	20.2
10H-4, 96–97	86.96	4	7	7	8.3
10H-4, 102–103	87.02	4	20	18	23.8
10H-5, 102–103	88.52	4	38	19	45.2
10H-6, 102–103	90.02	4	53	13	63.0

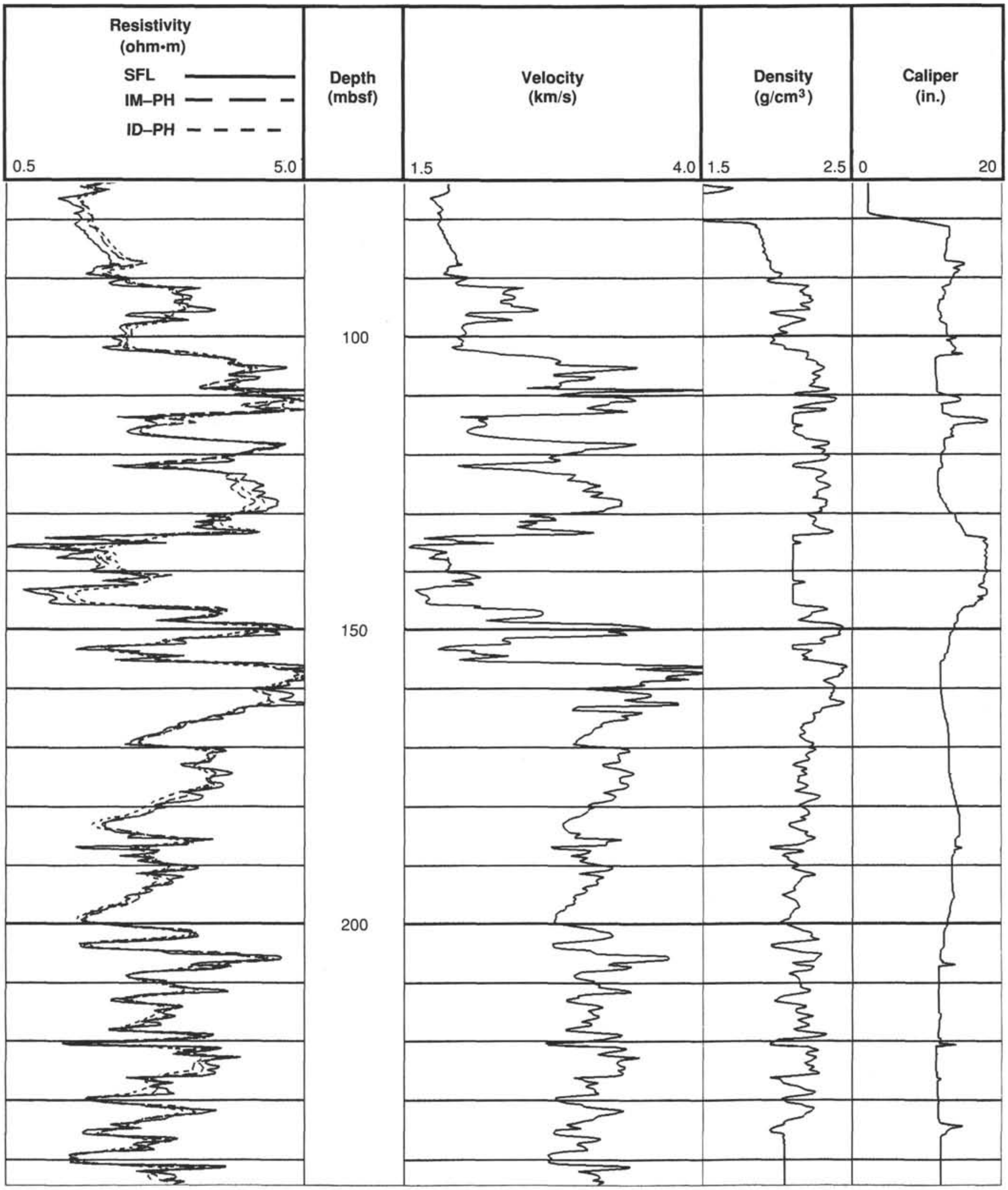

Figure 29. Primary porosity logs obtained by the seismic stratigraphic tool string at Hole 816C.

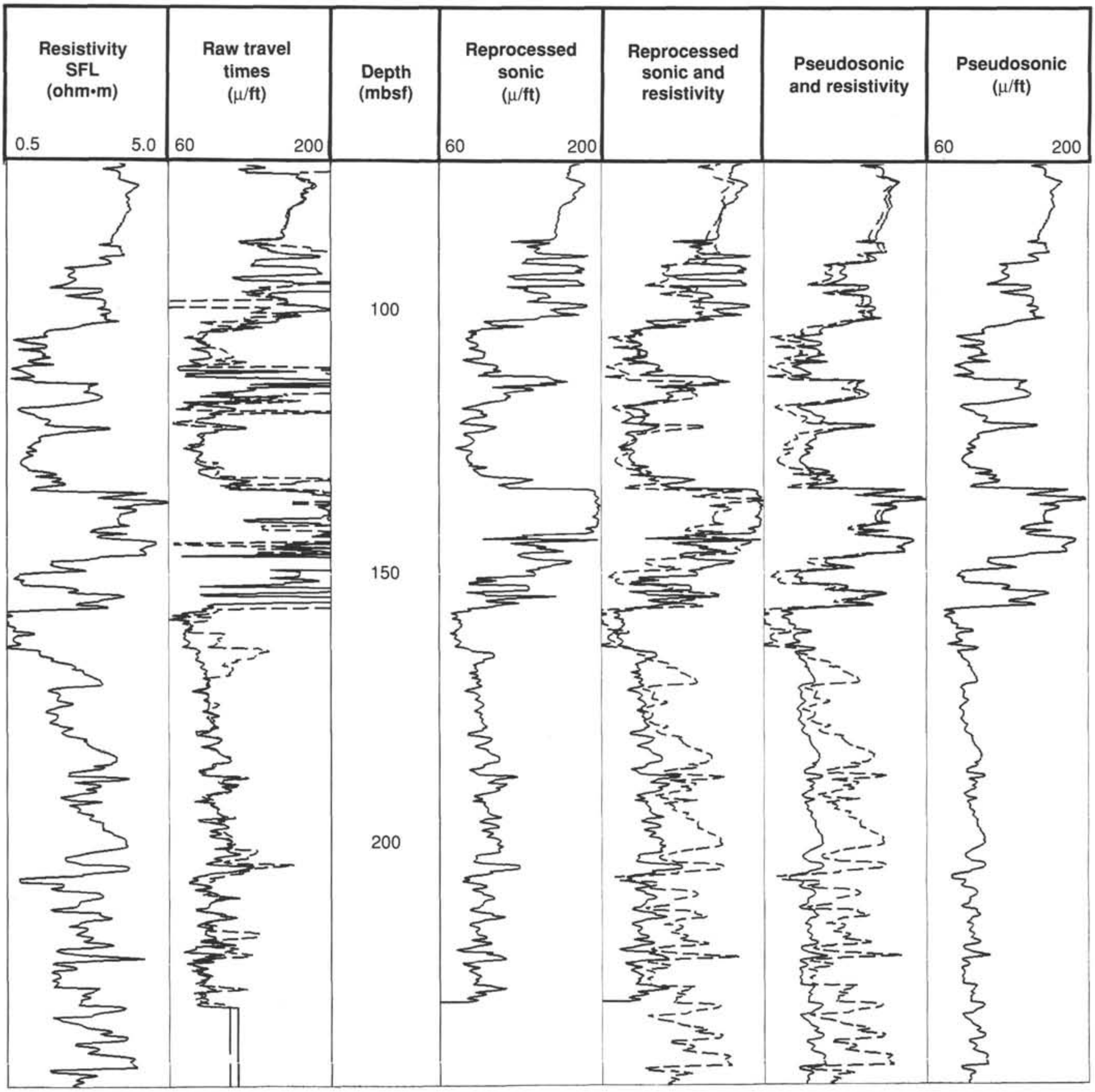

Figure 30. Comparison of the shallow focussed resistivity log (track 1) for Site 816 with the raw Schlumberger sonic logs (track 2), reprocessed sonic log (tracks 3 and 4) and a pseudosonic log based on resistivity (tracks 5 and 6).

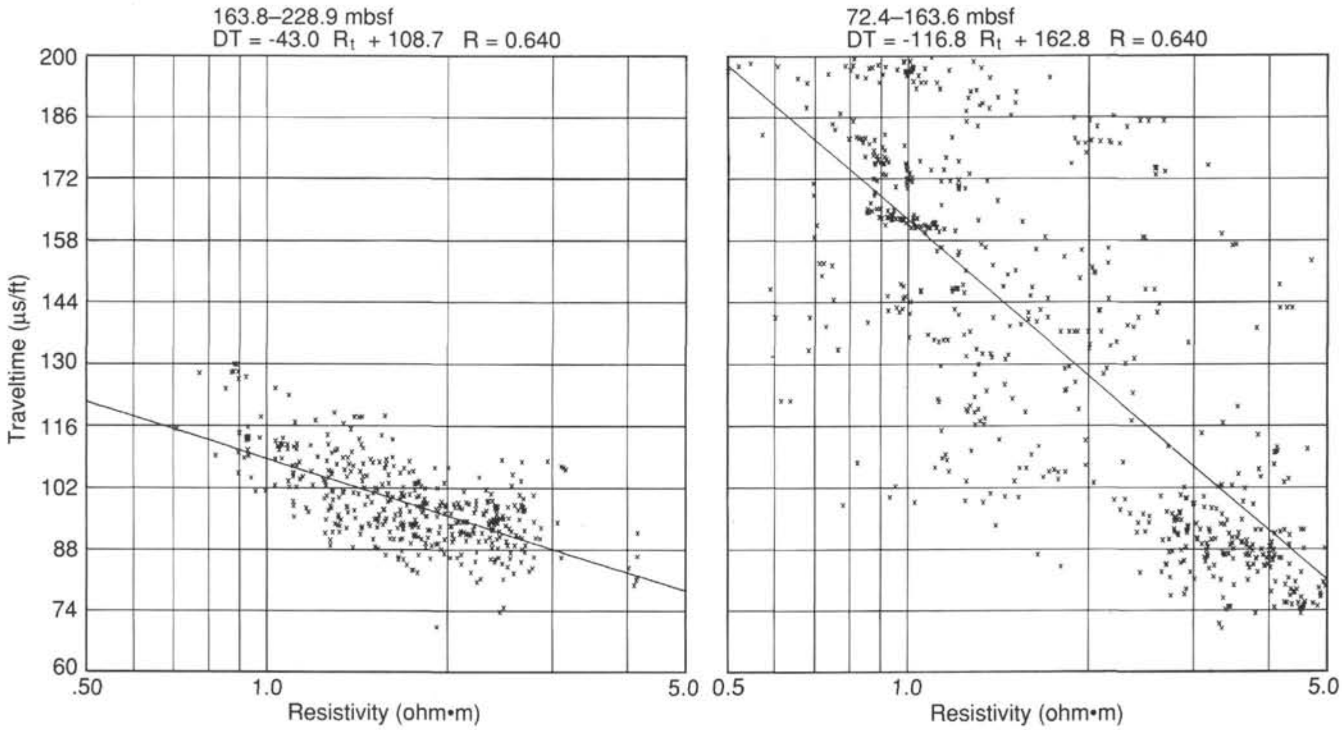

Figure 31. Relationship between resistivity and sonic traveltime for the two intervals 72.4–163.6 mbsf and 163.8–228.9 mbsf, used for calculating a pseudosonic log from resistivity.

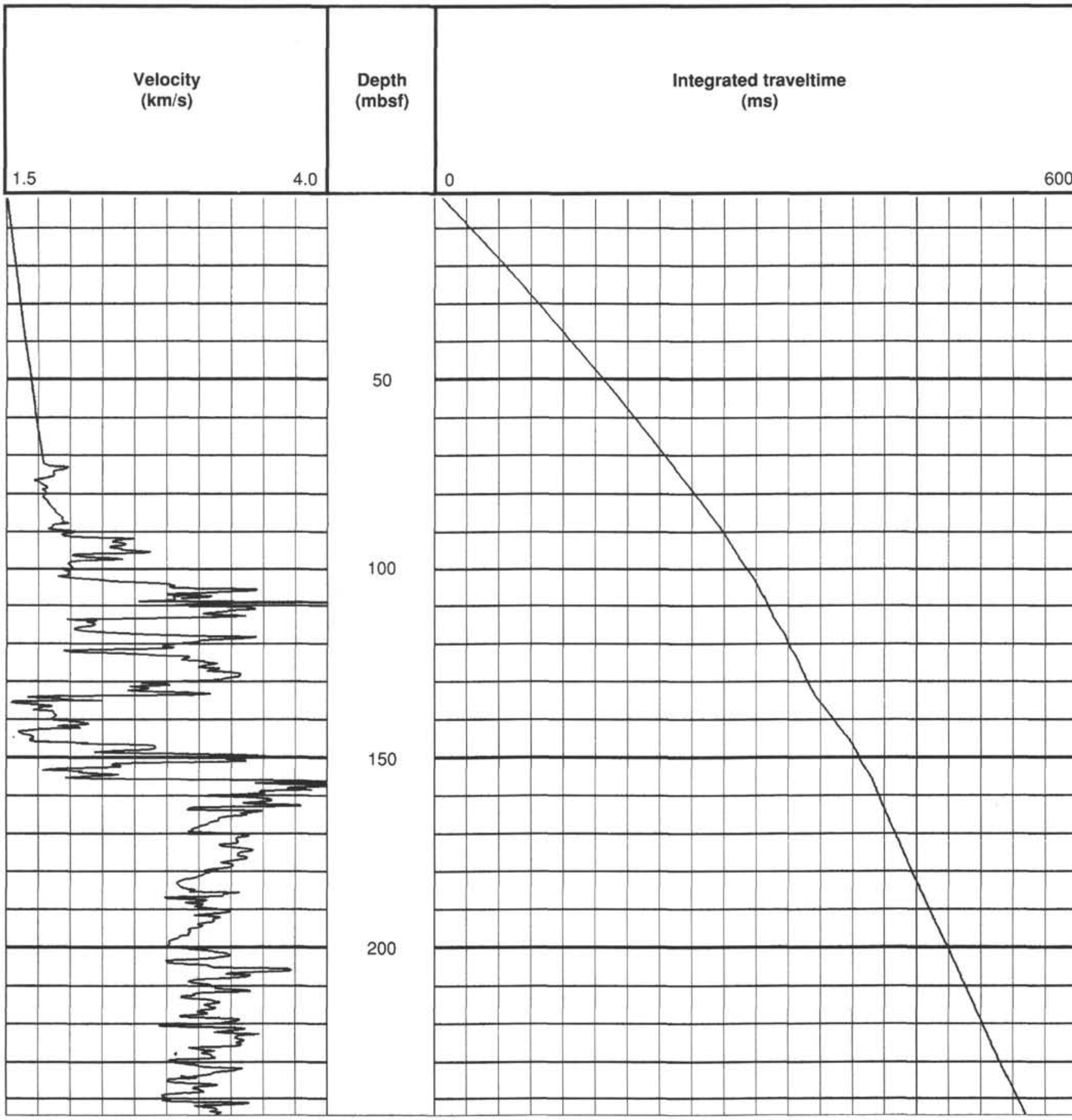

Figure 32. Velocity log and the integrated two-way traveltime function that it implies, for matching of core-based information from Site 816 with the seismic sections across the site.

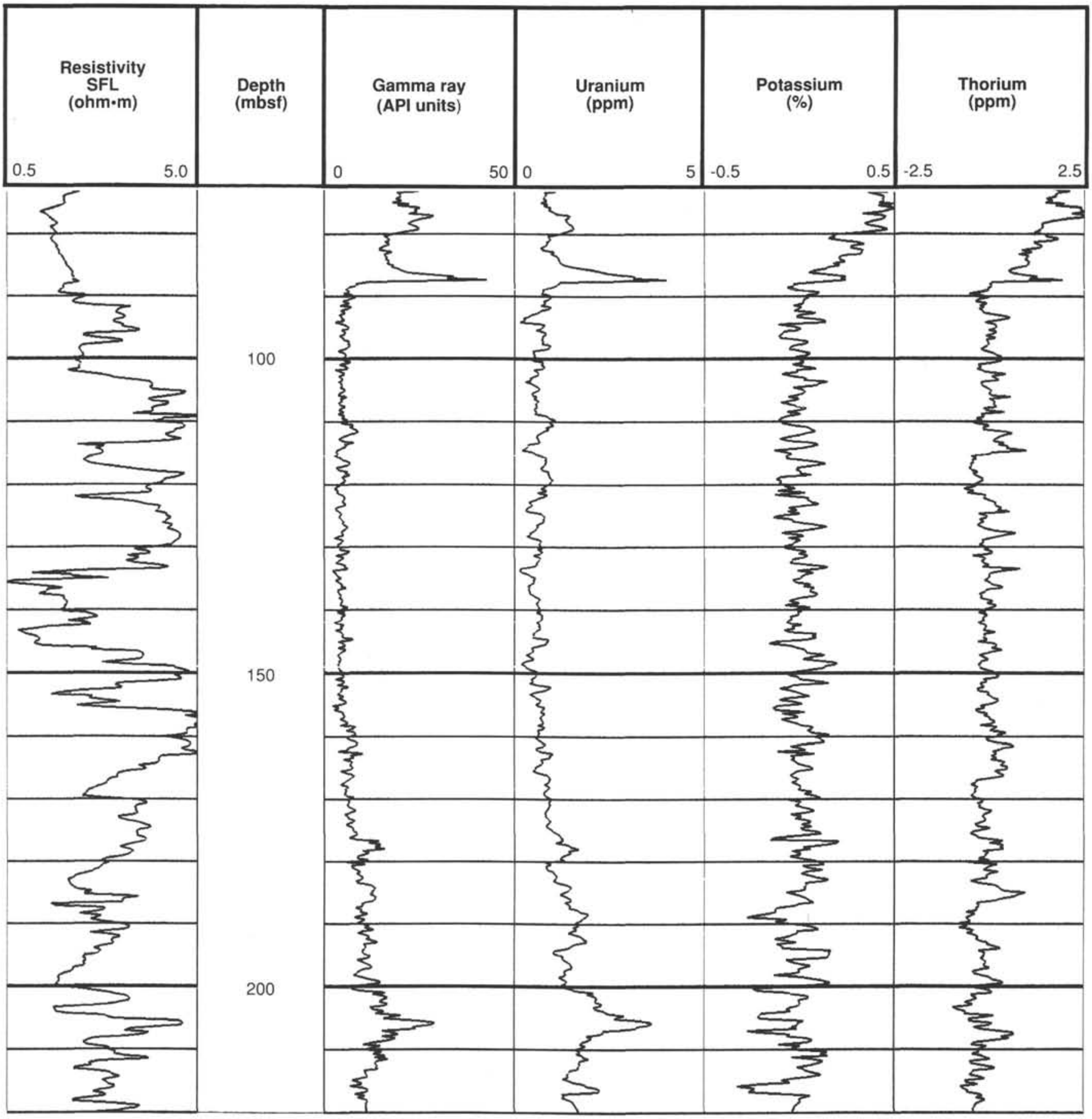

Figure 33. The spectral gamma-ray logs for Hole 816C, showing the marked difference between pelagic sediments above 90 mbsf and reef-derived sediments below 90 mbsf.

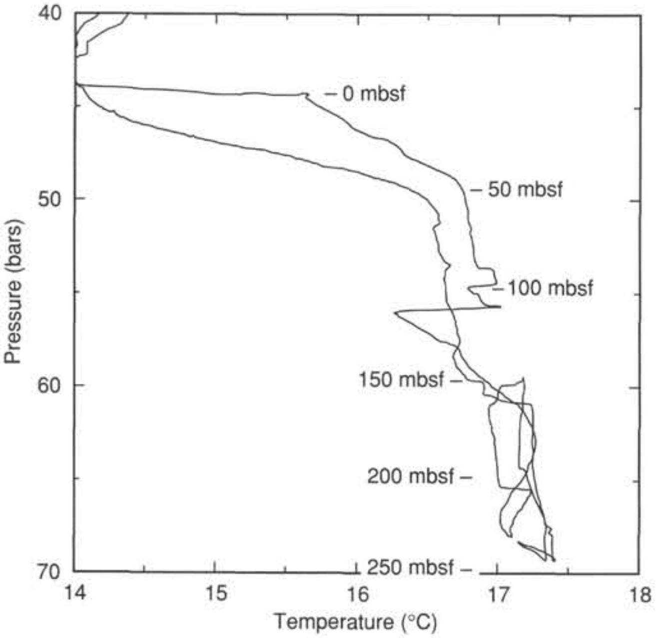

Figure 34. Temperature log as a function of pressure (or depth) for Site 816.

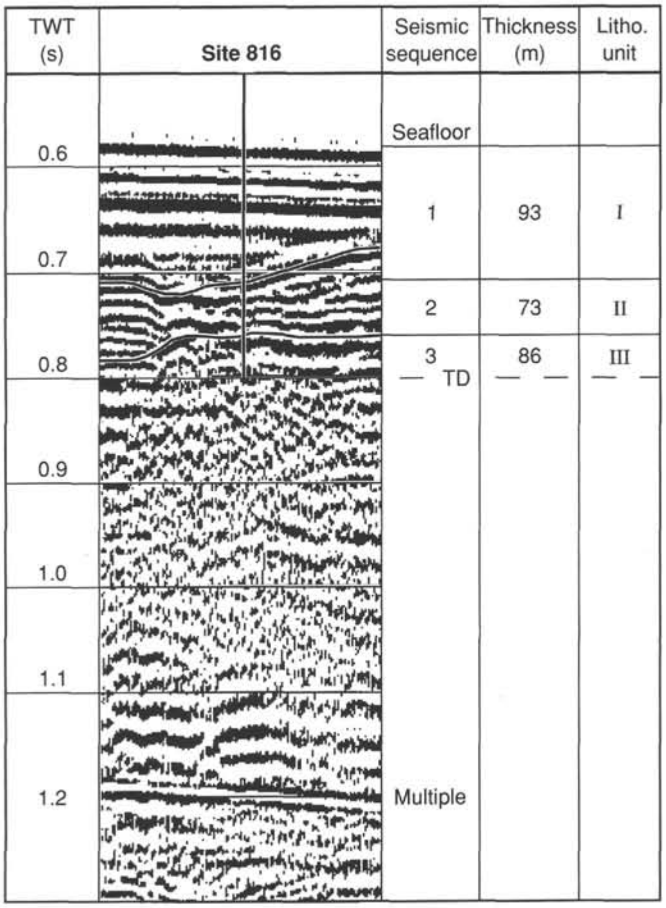

Figure 35. Seismic sequences at Site 816 showing their thickness and correlation with the lithologic units intersected. Based on BMR Line 75/027, Part A.

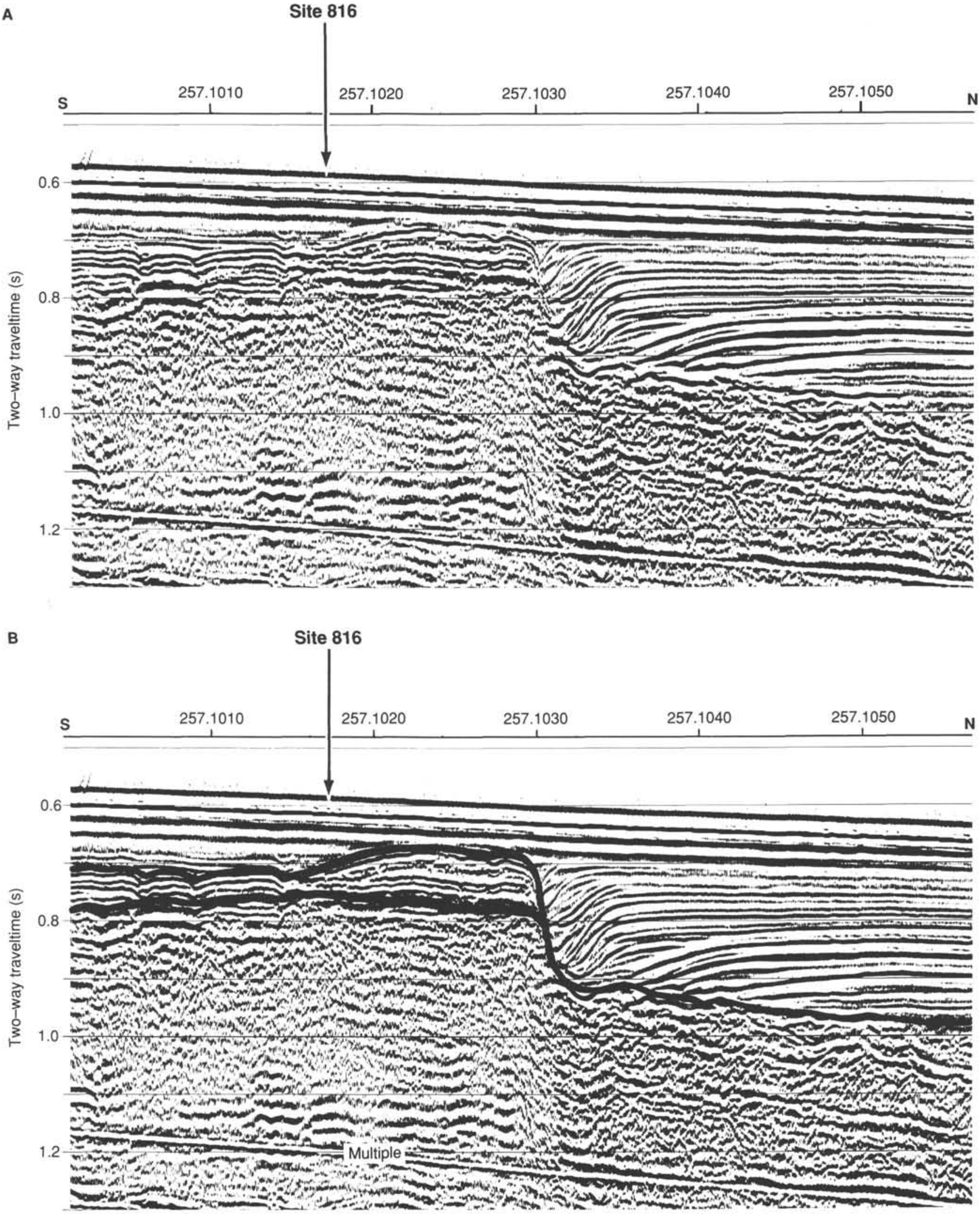

Figure 36. Uninterpreted (**A**); interpreted (**B**) seismic section showing the regional distribution of seismic sequences mapped at Site 816. Sequence stratigraphy of the downlapping section to the north of the site is described in the "Site 815" chapter (this volume); based on BMR seismic Line 75/027, Part A.

Hole 816B: Resistivity-Sonic-Natural Gamma Ray Log Summary

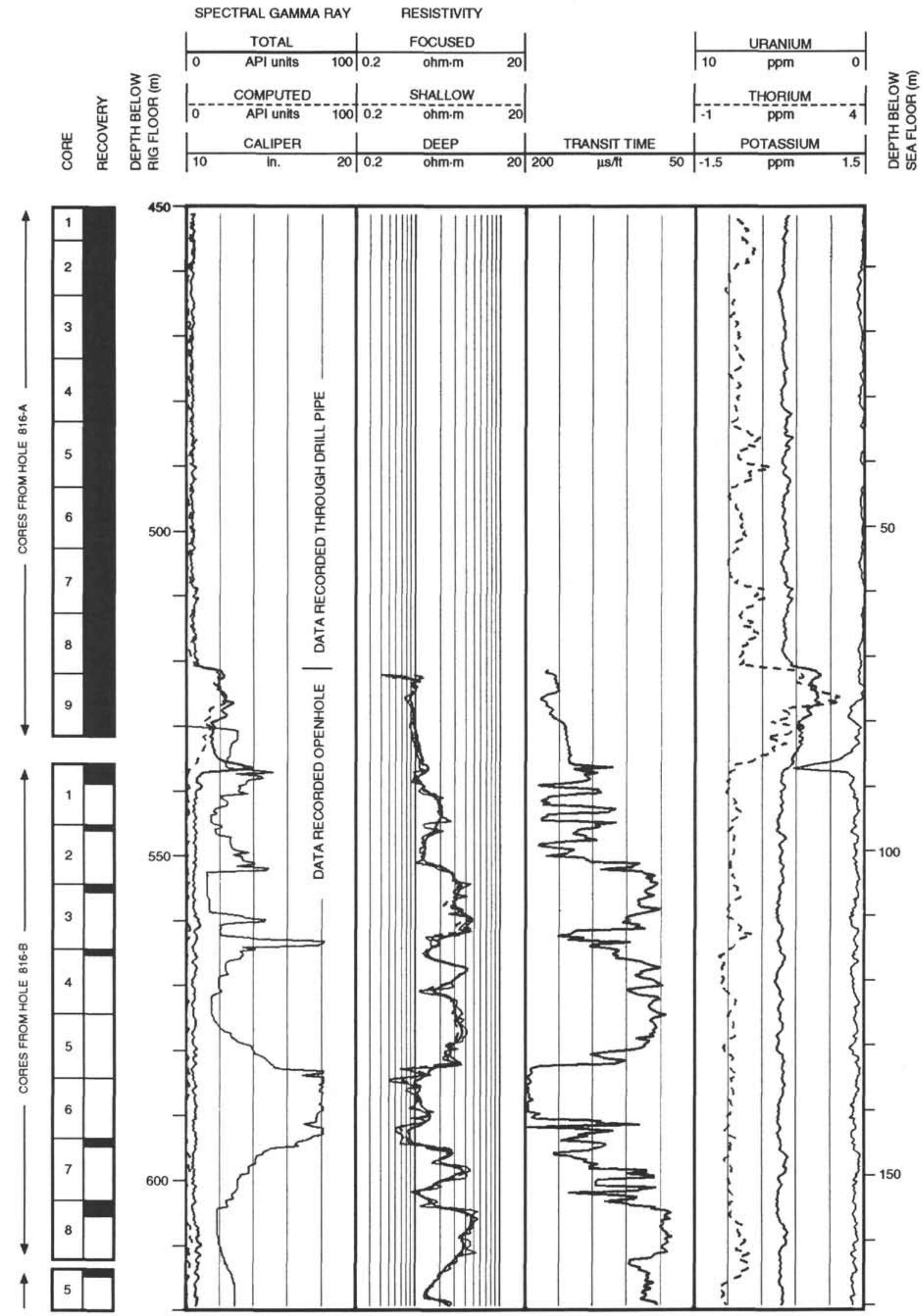

Hole 816B: Resistivity-Sonic-Natural Gamma Ray Log Summary (continued)

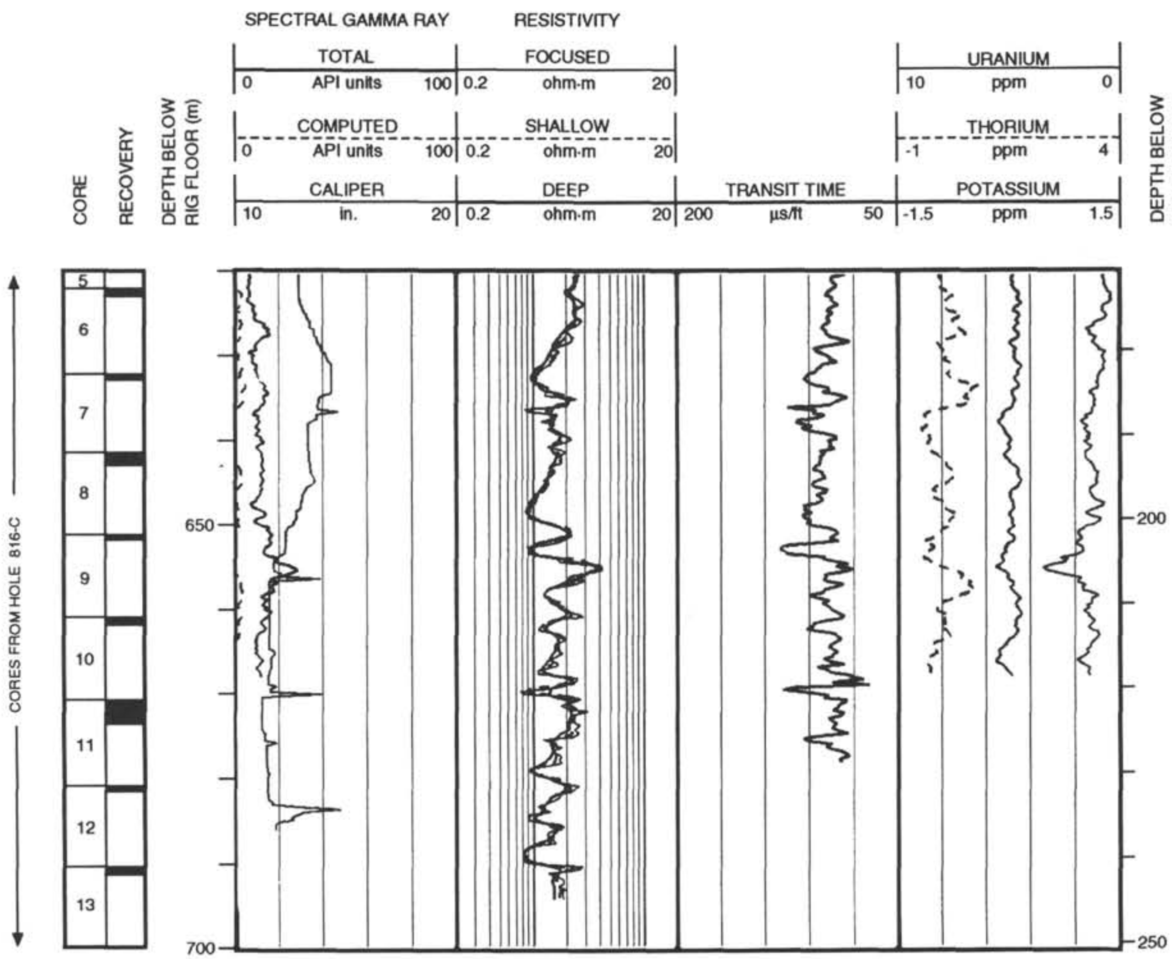

Hole 816B: Density-Natural Gamma Ray Log Summary

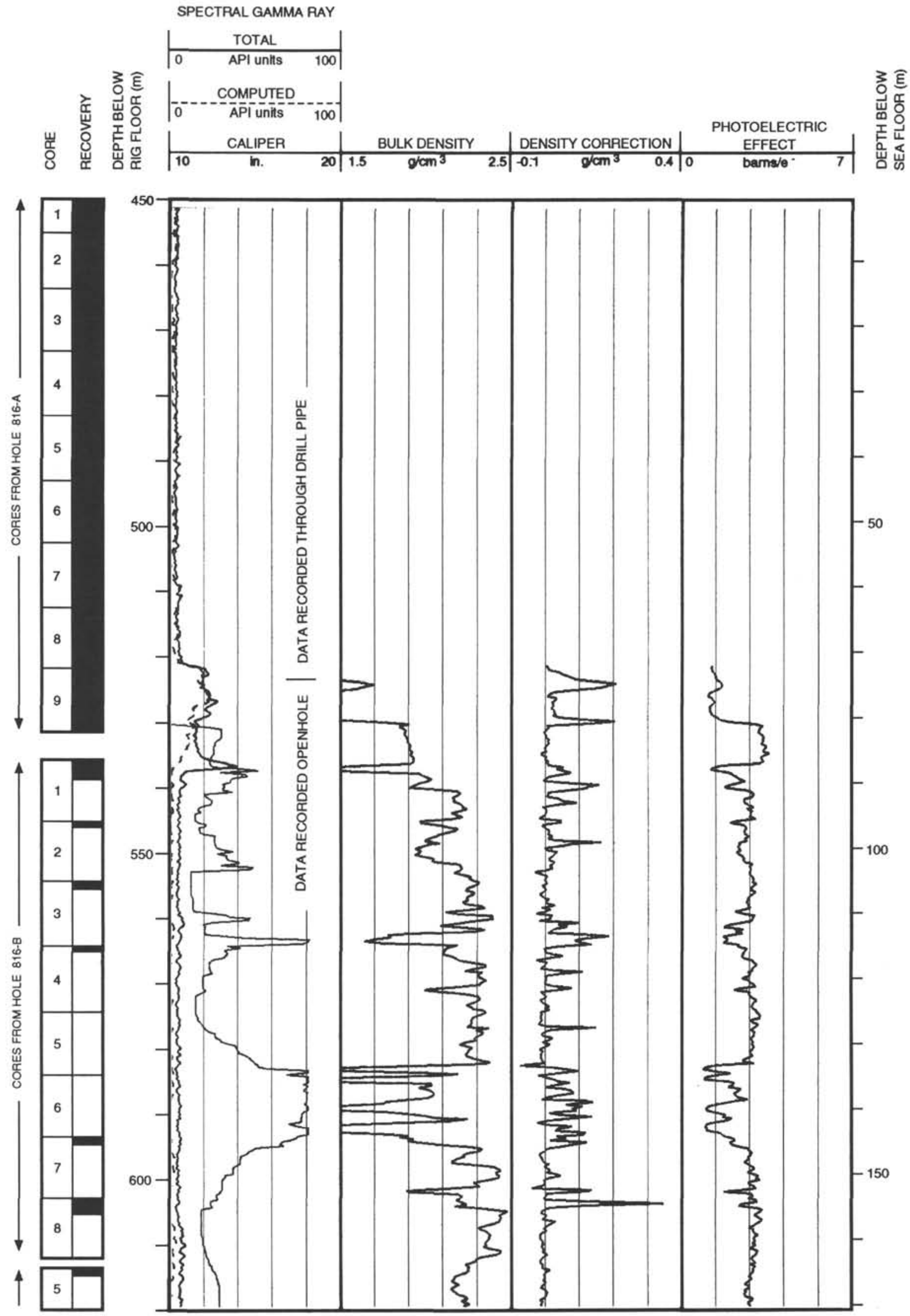

Hole 816B: Density-Natural Gamma Ray Log Summary (continued)